The thesis of Mirsaeed Zelli was reviewed and approved* by the following:

Dr. Catherine Kallin
Professor, McMaster University
Thesis Advisor

Dr. John Berlinsky
Academic Programs Director, Perimeter Institute
Committee Member

Dr. Paul Ayers
Professor, McMaster University
Committee member

Dr. Eric Sorenson
Professor, McMaster University
Committee Member

*Signatures are on file in the Graduate School.

The Mixed State of a π-Striped Superconductor

THE MIXED STATE OF A π-STRIPED SUPERCONDUCTOR

By

Mirsaeed Zelli, B.Sc., M.Sc.

A Thesis

Submitted to the School of Graduate Studies

in Partial Fulfillment of the Requirements

for the Degree of

Doctor of Philosophy

McMaster University

DOCTOR OF PHILOSOPHY (2012)   McMaster University

(Physics and Astronomy)   Hamilton, Ontario

TITLE: Landau Levels and Quantum Oscillations in a π-Striped Superconductor

AUTHOR: Mirsaeed Zelli, B.Sc. (University of Tehran), M.Sc. (University of Manitoba)

SUPERVISOR: Professor Catherine Kallin

NUMBER OF PAGES: xvii, 102

Abstract

In this thesis, we investigate the properties of a model of an anti-phase modulated d-wave superconductor, particularly in the presence of a magnetic field. This so-called model of π-striped superconductor has been proposed to describe the decoupling between Cu-O planes in 1/8 doped $La_{2-x}Ba_xCuO_4$. The d-wave superconducting order parameter in a π-striped superconductor oscillates spatially with period 8 and zero average value. Unlike a uniform d-wave superconductor, this model has non-zero density of states at zero energy and exhibits an extended Fermi surface. Within Bogoliubov-de Gennes theory, we study the mixed state of this model and compare it to the case of a uniform d-wave superconductor. We find a periodic structure of the low-energy density of states, with a period that is proportional to B, corresponding to Landau levels that are a coherent mixture of particles and holes. These results are also discussed in the context of experiments which observe quantum oscillations in the cuprates.

Furthermore, within Bogoliubov-de Gennes theory, a semiclassical approximation is used to study quantum oscillations and to determine the Fermi surface area associated with these oscillations in this model. The Fermi surface is reconstructed via Andreev-Bragg scattering, and the semiclassical motion is along these Fermi surface sections as well as between them via magnetic breakdown. Oscillations periodic in 1/B are found in both the positions and widths of the lowest Landau levels. The area corresponding to these quantum oscillations for intermediate pairing interaction is similar to that reported for experimental measurements in the cuprates. A comparison is made of this theory to data for quantum oscillations in the specific heat measured by Riggs et al.

Co-Authorship

This thesis represents original work written by myself, Mirsaeed Zelli and co-authored by Dr. Catherine Kallin and Dr. John Berlinsky. The results presented in this thesis are either published in or submitted to *Physical Review B*. The references for the papers are Zelli *et al.* (2011) Phys. Rev. B., 84, 174525 and Zelli *et al.* (2012) arXiv:1201.1920v2 (submitted to Phys. Rev. B). I grant an irrevocable, non-exclusive license to McMaster University and the National Library of Canada to reproduce this material as part of this thesis.

Acknowledgements

The work presented in this thesis is the result of five years of research. Here I wish to acknowledge many people who made this work possible in different ways along the way.

Before all else, I offer my sincere gratitude to my supervisor, Dr. Catherine Kallin, for her patient guidance and continuous support during the course of my Ph.D.. I also wish to express my deep gratitude to my co-supervisor, Dr. John Berlinsky, whose tremendous kindness and support will never be forgotten. I am grateful for all of their brilliant inputs and suggestions which made this thesis what it is.

I would like to thank members of my supervisory committee, Dr. Erik Sorensen, and Dr. Paul Ayers and Dr. Lee for their helpful contributions. I express my appreciation to all the staff of the Physics & Astronomy department, in particular, Liz Penny, Cheryl Johnston, Mara Esposto, Rose McNeice and Tina Stewart for their continuous help. I warmly thank Hua Wu for taking care of our computers. I also wish to thank my family. The work of this research would not be possible without their endless love and enormous inspiration. In particular, I am so grateful to my father whom I can never thank enough for all the things he has done for me.

I would like to thank all the graduate students with whom I shared my time during the course of my Ph.D.. I will never forget my great times here at McMaster. Many thanks to Prasanna and Shouvik, with whom I shared my office. Lastly, I would like to thank my current and previous group members, in particular, Phil Ashby and Michael Young, for great discussions.

Table of Contents

List of Figures

ix

xiii

xiv

Chapter 1

Introduction and Overview

1.1   Introduction

Superconductivity is a state characterized by perfect conductivity and perfect diamagnetism. It was first discovered by Onnes in 1911 in mercury at temperatures below 4.1K, known as the superconducting transition temperature, T_c. After the discovery, numerous other metals were found to exhibit superconductivity at very low temperatures. Nevertheless, the mechanism of superconductivity remained a mystery for many years until Bardeen, Cooper, and Schrieffer presented a complete theoretical picture in 1957 (Bardeen *et al.*, 1957). The so-called BCS theory is an instability of the Fermi surface (FS) in the presence of an attractive interaction between electrons at low temperatures. The interactions in the BCS model is mediated by phonons, vibrations of the underlying lattice. The instability of the FS is due to the formation of bound pairs of electrons, called Cooper pairs. The $2e$ charge-carrying Cooper pairs can move in the material without resistance, leading to superconductivity. There is a minimum energy required to break the pairing of each Cooper

pair. This leads to the appearance of a gap at the Fermi energy, consistent with experimental measurements. Details of BCS theory can be found in the two books by Tinkham (1996) and de Gennes (1989).

Although BCS theory is successful in describing the mechanism of superconductivity in metals, it fails to explain the nature of the phenomenon in the so-called unconventional superconductors such as high temperature superconductors. The nature of high temperature superconductivity, in particular cuprate superconductivity, is perhaps the most challenging problem in modern condensed matter physics. It is the aim of this thesis to investigate one particular model that has been proposed to explain some of the properties of the cuprate superconductors. Before discussing the current situation of our understanding of the cuprate superconductors, we would like to briefly discuss the mixed state of superconductors, as it is a crucial concept that we will use in the rest of the thesis.

1.1.1 Mixed State

A perfect conductor in the presence of a magnetic field prevents the field from entering the bulk. A superconductor, in addition to this property, expels a field as it is cooled through the critical temperature. This phenomenon is called the Meissner effect. When the magnetic field exceeds a critical field H_c, it is energetically favorable to let the field enter the superconductor and the state of the matter becomes a normal state. However, for type II superconductors, the transition to the normal state is a smooth transition which might span several tens of Tesla. Unlike their type I counterparts, the magnetic field flux starts to partially penetrate the type II superconductor at a lower critical field

H_{c1} and only becomes a normal state at an upper critical field H_{c2}. Between H_{c1} and H_{c2}, the material consists of superconducting and normal domains known as the mixed state. Perhaps the most important property of the mixed state is that the normal domains are flux tubes that carry a fluxoid quantum of $\Phi_0 = hc/2e$ which is half of the flux quantum, ϕ_0. The flux tubes, also called vortices, tend to arrange themselves in an ordered array such as a triangular or square array. In the presence of vortices, the magnetic field in the London approximation is given by

$$B - \lambda^2 \nabla^2 B = \frac{\phi_0}{2} \sum_i \delta(\vec{r} - \vec{r}_i) \qquad (1.1)$$

where λ is the London penetration depth and the summation is over the positions of the vortices. We use this equation in Appendix C to find the superfluid velocity field.

1.2   High Temperature Superconductivity

In 1986, a new superconducting state was observed by Bednorz and Muller in Sr-doped La_2CuO_4 at temperatures close to 30K (Bednorz and Muller, 1986). This discovery had a huge impact on solid state physics as T_c was higher than that could be understood by the BCS theory. Subsequently, other doped Copper-oxide materials, the so-called cuprates, have been found to be superconducting at even higher temperatures. This is why the term high temperature superconductivity is used to refer to this surprising phenomenon seen in these ceramic superconductors. Note that the cuprates are only one of two classes of the high temperatures superconductors that are known at

this point in time. The other class is the iron-based superconductors which were discovered much later than the cuprates in 2008. In this thesis, we focus on the first class of high temperature superconductivity, the cuprate superconductivity.
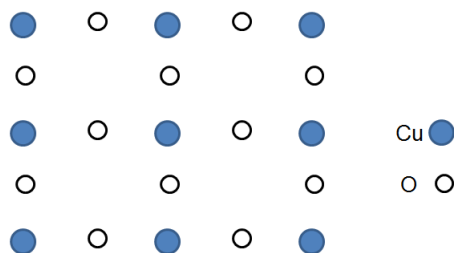
Figure 1.1 The two dimensional structure of a CuO$_2$ layer in cuprates.

1.3   Cuprates

Cuprates are made by doping the parent rare earth copper-oxide material with different kinds of dopants such as Sr. The undoped parent material is a quasi-two dimensional material in the sense that it consists of two dimensional copper-oxide (CuO$_2$) layers that have weak inter-layer interactions. The structure of a single CuO$_2$ layer is shown in Fig. 1.1. The Cu atoms which form a square lattice each have one unpaired electron in the undoped state. When the material is doped with holes, some of the Cu atoms lose an electron and all their remaining valence electrons are paired. The O atoms are located on the bonds connecting the nearest neighbor Cu atoms. The rest of the atoms in the material lie in between the CuO$_2$ layers and play the role of a charge reservoir.

It is common to discuss cuprates in terms of their phase diagram as a function of temperature, T, and hole-doping, x. In general, the cuprates have
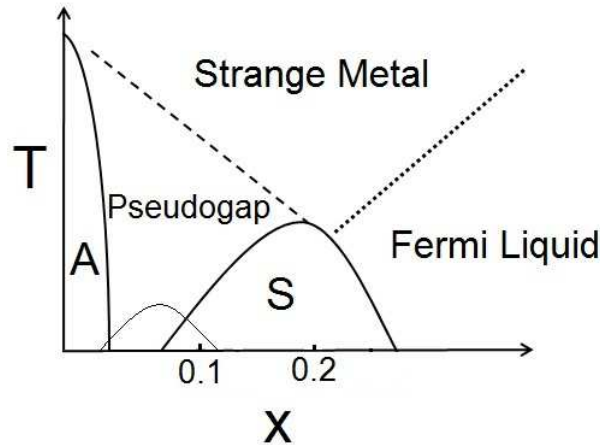
Figure 1.2 General phase diagram of hole doped cuprates as a function of doping and temperature. A denotes an antiferromagnetic insulating state and S denotes a superconducting state.

a phase diagram as shown in Fig. 1.2. Although the parent material can also be doped with electrons, Fig. 1.2 only shows the hole-doped phase diagram which is the focus of this thesis. Around $x = 0$, the so-called half-filling, the material is an insulating anteriferromagent. The insulating behavior is due to the strong on-site Coulomb repulsion which prevents Cu atoms from being occupied by two electrons. Consequently conduction is suppressed and the material becomes a Mott insulator. Superconductivity, denoted by S in Fig. 1.2, appears in the cuprates only when the antiferromagnetic order is destabilized by doping. The transition temperature increases with the doping, x, and reaches a maximum at the "optimal doping". Beyond optimal doping, the transition temperature decreases with x and finally the superconducting phase disappears at fairly large dopings. Cuprates are classified as underdoped and overdoped based on their hole-doping in the phase diagram relative to optimal doping. The two classes have significant differences that will be discussed in the following paragraphs.

The dashed line in 1.2 indicates a cross-over from the normal state to the so-called pesudogap phase. This mysterious phase that occurs for underdoped cuprates and temperature range $T_c < T < T^*$, is the subject of extensive and ongoing research (Norman and Pepin, 2003). Although not superconducting, it is shown that some of the properties of the superconducting state appear in the pseudogap phase (Williams *et al.*, 1997). Even the normal phase of the cuprates, above the pseudogap phase in the phase diagram, exhibits some peculiar properties. For example, conductivity measurements show that it acts like a metal within the Cu-O layers but is an insulator along the normal direction to the layers. The resistivity within the Cu-O planes varies linearly as a function of T which is different from the T^2 dependence of a Fermi Liquid. This part of the phase diagram is referred as a "strange metal" due to the its strange characteristics. The normal state for the overdoped materials, however, is a Fermi Liquid. The small region between the antiferromagnetic and superconducting phase in the phase diagram is believed to be one where various orderings such as spin glasses and stripes compete and, as a result, is poorly understood.

1.3.1   Nature of Superconductivity in the Cuprates

Conventional metallic superconductors are s-wave. That is, the superconducting gap around the FS is relatively independent of the wave vector k. The cuprates were initially thought to have the same property. However, after years of controversies, it was confirmed that the superconducting gap in the cuprates has a d-wave symmetry (Hardy *et al.*, 1993; Van Harlingen, 1995; Tsuei and Kirtley, 2000). The d-wave superconducting gap changes signs and

amplitude around the FS. The amplitude of the gap goes to zero at four points in the BZ which we refer as nodal points or simply nodes. The nodal behavior gives rise to zero-energy excitations which dramatically changes the low temperature physics of the cuprates from that of conventional superconductors.

The Cu-O layers in the cuprates are modelled by a constrained two dimensional tight-binding Hamiltonian with nearest neighbor antiferromagnetic exchange interaction, the so-called t-J model (Ogata and Fukuyama, 2008), which is derived from the Hubbard model in the strong Coloumb repulsion limit. The constraint in the t-J model is the "no-double occupancy" rule which turns it into a strongly correlated problem. The model can be solved approximately using self-consistent BdG mean field theory which results in the following k-dependence for the gap in the homogeneous case

$$\Delta_k = 2\Delta[\cos(k_x) - \cos(k_y)] \qquad (1.2)$$

where Δ is the magnitude of the uniform d-wave order parameter. Then the excitation energy for the quasiparticles is given by

$$\epsilon_k = \sqrt{E_k^2 + \Delta_k^2} \qquad (1.3)$$

$E_k = -2t[\cos(k_x) + \cos(k_y)] - \mu$ is the dispersion for the kinetic part of the Hamiltonian. As usual, physicists are interested in the low energy energy spectrum which can be obtained by expansion of the cos function in E_k and Δ_k around the nodes. The result is a Dirac-like dispersion relation given by

$$\epsilon_k = \sqrt{(\hbar v_F k_1)^2 + (\hbar v_\Delta k_2)^2}. \qquad (1.4)$$

where k_1 (k_2) is the wave vector component normal (tangential) to the FS and $\hbar v_F$ ($\hbar v_\Delta$) is the slope of the linear change in quasiparticle energy along that direction. As a result, the low-energy density of states is linear with respect to the quasiparticle energy which explains some of the low-temperature properties of the cuprates (Imai *et al.*, 1988; Hardy *et al.*, 1993). As an example the electronic specific heat goes as T^2.

There are, however, measurements and phenomenon that can not be explained with the the simple picture of a BCS-type d-wave superconductor. Eq. (1.4) describes well-defined, long-lived quasiparticle excitations that would suggest a Fermi Liquid type behavior for the normal state of the cuprates. However, in the underdoped regime of the cuprates, the Fermi liquid type behavior is absent for both the pseudogap and the strange metal regions. Other mysterious features of the cuprates are the formation of stripes and quantum oscillations. Here we will review the pseudogap phase and the quantum oscillations in the cuprates. We will discuss the stripe structure in the next chapter.

1.3.2 Pseudogap

The nature of the pseudogap phase remains a mystery after years of study and debate. The physical behavior in this phase can be characterized as "non-Fermi-liquid-like", which typically means that the sharp fermionic excitations of a Fermi liquid are broadened even close to the Fermi surface (Ding *et al.*, 1997; Norman *et al.*, 1998). The spin excitations are suppressed which means that a gap develops in this pseudogap phase (Williams *et al.*, 1997). This gap does not lead to superconductivity, and it is also not a full gap with zero

density of states at low energy, which is why this phase is called the pseudogap phase. The pseudogap can be seen in different experiments such as NMR (Williams *et al.*, 1997) and ARPES (Ding *et al.*, 1997; Norman *et al.*, 1998). ARPES observes disconnected sections of 2D FS which appear to terminate at gaps near anti-nodal points at $(\pm\pi, 0)$ and $(0, \pm\pi)$, but which also could be segments of FS pockets where only part of the pocket has significant spectral weight. These so-called Fermi arcs become shorter, possibly tending toward nodal points, as T is lowered. No sharp quasiparticles are observed near the anti-nodal points at $(\pm\pi, \pm\pi)$.

The source of the non-Fermi-liquid-like behavior is the subject of hot debates and disputes. Some studies connect it to resonating valence bonds (Anderson, 1987) or preformed pairs (Randeria *et al.*, 1989). Others associate it with exotic forms of fluctuating or static spatial order such as charge or spin density waves (Brown and Gruner, 1994; Borisenko *et al.*, 2008; Emery *et al.*, 1997) or singlet or triplet D-density waves (Chakravarty *et al.*, 2001). The model studied in this thesis is proposed to have connections to the pseudogap phase.

1.3.3 Quantum Oscillations

Recent observations of Quantum oscillations (QO) in the cuprates added one more piece to the puzzle of high temperature cuprate superconductivity. QO are a quantum phenomenon in which various properties of a metals exhibit oscillatory behavior as a function of $1/H$ that are related to the shape of the FS. Techniques based on quantum oscillations are important experimental tools for determining the shape of the FS of various materials. The phenomenon

was first observed in magnetization measurements of a sample of bismuth in 1930. A plausible theoretical theory for the QO phenomenon was not proposed until a much later time in 1952 when Onsager showed that the period of oscillations in $1/H$ is in fact proportional to $1/A$ where A is an extremal cross-sectional area of the FS in a plane perpendicular to the magnetic field. Onsager's qualitative picture can be understood based on the formation of Landau levels (LLs) near the Fermi energy. LLs are equally spaced discrete energy levels that are formed due to the presence of a magnetic field and are reviewed in appendix A. Here we describe the qualitative picture of QO for a two dimensional free electron system where LLs are formed near the Fermi energy. A more precise derivation of the quantum oscillations can be found in the book by Shoenberg (1984).

As the magnetic field increases, the LL spacing $\hbar\omega_c$ increases and, as a result, LLs pass through the Fermi energy. Suppose, for a certain magnetic field, one LL lies exactly on top of the Fermi energy. Then one can write $\epsilon_F = (n + 1/2)\hbar\omega_c$ where n is an integer counting the number of LLs from zero to ϵ_F. Once the magnetic field increases, the LL moves away from the Fermi energy. However, for some other magnetic field, another consecutive LL will again be at the Fermi energy so that $\epsilon_F = (n - 1/2)\hbar\omega_c$. It follows that $\Delta(\epsilon_F/\hbar\omega_c) = 1$. Using the relations $\epsilon_F = \frac{\hbar^2 A}{2\pi m}$ and $\hbar\omega_c = \frac{\hbar e H}{mc}$ for two dimensional electrons, we obtain Onsager's relation,

$$\Delta(\frac{1}{H}) = \frac{2\pi e}{\hbar c}\frac{1}{A}. \tag{1.5}$$

Thus the frequency of oscillations in $1/H$ is given by $F = (c\hbar/2\pi e)A$. Note that the periodic behavior of LLs going through the Fermi energy corresponds

to oscillations in the magnitude of the DOS at the Fermi energy. This quantity
couples directly to other physical quantities and hence gives rise to periodic
oscillations in those other properties. The oscillatory behavior in the mag-
netization is called the de Haas-van Alphen (dHvA) effect in honor of its
discoverers. Quantum oscillations can also be seen in the field dependence of
the specific heat, electrical resistivity and mechanical properties. In the case
of electrical resistivity, the phenomenon is called the Shubnikov-de Haas effect.

A more rigorous derivation of the Onsager's relation for each property
starts by writing the free energy as follows:

$$\Omega = -k_B T \sum_i \ln[1 - \exp(-\beta(\epsilon_i - \mu)] \tag{1.6}$$

where the sum is over all possible states with energy ϵ_F. Consequently one
can find each property such as the specific heat, magnetization, etc., by taking
one or more partial derivative of the free energy. The resulting formula is
the so-called Lifshitz-Kosevich (LK) formula (Lifshitz and Kosevich, 1955).
Experimental data is fit to the LK formula to find the area and effective mass
associated with QO.

Quantum oscillations in the underdoped cuprates were first observed in
the electrical resistivity of YBCO in 2007 (Doiron-Leyraud *et al.*, 2007). Since
2007, quantum oscillations have been observed in other physical properties
and are now a well-established phenomenon in the cuprates (Jaudet *et al.*,
2008; Riggs *et al.*, 2011; Bangura *et al.*, 2008; Yelland *et al.*, 2008; Audouard
et al., 2009; Sebastian *et al.*, 2008; Singleton *et al.*, 2010; Rourke *et al.*, 2010;
Yao *et al.*, 2011). It is indicative of the existence of a Fermi surface in the
normal state of the underdoped cuprates. Here the term "normal state" is

ambiguous because the measurements are performed in a resistive state where the superconducting pairing potential can still be present. In other words, because the magnetic field is below H_{c2}, the sample can be in a vortex liquid state which gives rise to finite resistivity. Consequently, the observation of QO has shifted the focus away from RVB, etc, toward broken symmetry Fermi liquid states. Nevertheless, the result of QO experiments is also interesting. The FS area is only about 2% of the Brillouin zone (BZ), which is significantly smaller than the area one would expect from paramagnetic band structure calculations (Andersen *et al.*, 1995). Also the Hall resistivity measurements have determined the FS to be an electron pocket (Leboeuf *et al.*, 2007) which is unexpected for a hole-doped cuprate. In contrast, the FS area associated with QO in the overdoped cuprates is a large FS consistent with the hole doping (Vignolle *et al.*, 2008). So the following immediate questions arise: Is the QO a characteristic of the normal state in the underdoped cuprates? Why does it occur and why is it so dramatically different from the overdoped cuprates?

There have been different proposals to explain quantum oscillations in the cuprates (Pereg-Barnea *et al.*, 2009; Elfimov *et al.*, 2008; Alexandrov, 2008). A FS reconstruction approach due to some form of translational symmetry breaking order is the most promising approach (Brown and Gruner, 1994; Borisenko *et al.*, 2008). Translational symmetry can break due to different reasons, for example antiferromagnetism or the stripe order that comes in the the form of density waves in the cuprates. Providing an alternative explanation for QO in the cuprates based a model of a superconductor with stripe order is the main focus of this thesis.

1.4 Summary and Overview

A quarter of century after the discovery of the first high-T_c superconductor, the mechanism responsible for the phenomenon is not established. The understanding of the normal state from which the superconductivity arises is a crucial step to understanding the cuprate superconductivity. In principle, one expects to go from the superconducting state to the normal state by either raising the temperature or the magnetic field. As discussed earlier, the physical behavior at higher temperatures is non-Fermi-liquid-like. However, the state obtained from destroying superconductivity by a magnetic field behaves like a Fermi liquid. This is mainly based on the observation of quantum oscillations in cuprates. Furthermore, it is not straightforward to connect the FS areas determined by quantum oscillations with the Fermi arc observed in ARPES (Onsager, 1952). However it has been noted that commensurate static translational symmetry breaking, due to charge or spin density waves, could reorganize the large hole FS of the undistorted lattice into a number of smaller hole and electron pockets and that the small electron pockets could account for the quantum oscillations (Millis and Norman, 2007; Harrison, 2009). The explanation for the arcs is then that the spectral weight due to the periodic perturbation of the CDW or SDW is large on the arcs that are observed by ARPES and small on the remainder of the FS hole pockets.

In this thesis, we consider a variation of this picture in which the periodic superlattice arises from a modulation of the d-wave superconducting gap function (Berg *et al.*, 2007, 2009; Baruch and Orgad, 2008). We study such a modulated pairing potential in the presence of large magnetic fields using lattice Bogoliubov-de Gennes (BdG) theory (de Gennes, 1989) to determine

whether it gives rise to quantum oscillations. The remainder of this thesis is organized as follows. In chapter 2, we describe the model for a π-striped superconductor. This section shows the density of states (DOS), the spectral functions and the FS in zero field for different gap amplitudes for this model. In chapter 3, we establish the formation of Landau levels by a magnetic field and examine the effect of the doping the gap amplitude on the Landau level spectra. In addition, the specific heat is calculated to make some connection to experiment. In chapter 4, we provide the justification for a semiclassical approximation which enables us to calculate the area associated with quantum oscillations. Consequently, a consistent picture of quantum oscillations in a π-striped superconductor corresponding to different FS areas was obtained. The quantum oscillations in this chapter are all found within the context of the semicalssical approximation and still need to be proved rigorously. Finally, we summarize this thesis and provide an outlook in chapter 5.

Chapter 2

A π-striped Superconductor

2.1   Introduction

The interplay between magnetism and superconductivity is an essential feature
of the high T_c cuprates. The transition from an antiferromagnetic state at half-
filling to a superconducting state at finite doping is key to understanding of
these materials. To examine the nature of this transition, one needs to address
the region in the phase diagram at low temperature that includes the end of
the antiferromagnetic region and the beginning of the superconducting dome.
This is illustrated by the region inside the thin line in Fig. 1.2. In this region,
there are evidence for spin glass (Matsuda *et al.*, 2002) behavior and stripe
order (Tranquada *et al.*, 1995; Fujita *et al.*, 2004; Abbamonte *et al.*, 2005).
Stripes, which are the focus of this thesis, are not only limited to this part of
the phase diagram and can exist at higher dopings as well.

Stripes is the term describing unidirectional density waves. Stripes are
associated with either a periodic modulation of the charge density, charge den-
sity waves (CDW), or spin density waves (SDW). The stripe state is mainly

observed in lanthanum cuprates such as $La_{2-x}Ba_xCuO_4$ and $La_{2-x}Sr_xCuO_4$. In this family of cuprates, the stripe order is most stable at 1/8 doping and is known to coincide with a CDW with the periodicity of 4 lattice constants. Stripes are believed to be the reason for the so-called "1/8 anomaly" phenomenon in which most lanthanum cuprates exhibit singular behavior in the doping dependence of various low-temperature properties around 1/8 doping. The deep minimum in T_c is one of the several anomalies that have been observed in lanthanum cuprates at 1/8 doping. One more example of the 1/8 anomaly is the visible minimum in the superfluid density $n_s(x)$ as function of the hole doping x at 1/8 doping (Berg *et al.*, 2003). The evidence for the existence of stripes in other cuprates is less compelling. However, studies have shown that stripes can be induced by a magnetic field in YBCO, a cuprate with minimal chemical disorder (Wu *et al.*, 2011; Haug *et al.*, 2009). Stripes can be either static or dynamic. Static stripes have been observed only in certain particular compounds. However, there are signatures of dynamic stripe order in the cuprates (Xu *et al.*, 2007).

Whether the stripe state competes or coexists with superconductivity is not well understood. The fact that T_c for some cuprates drops at 1/8 doping points to the competing nature of stripe and superconducting order. However, some experimental studies argue that the two states coexist (Howald *et al.*, 2003; Hücker *et al.*, 2011; Tranquada *et al.*, 2008). Nevertheless, there is evidence that a two-dimensional-type superconductivity arises within the cuprate layers which is in direct relation to the appearance of the stripe order in 1/8 doped $La_{2-x}Ba_xCuO_4$ (Li *et al.*, 2007). Meanwhile, an apparent dynamical decoupling of the cuprate layers is observed which results in zero Josephson coupling between nearest cuprate layers. This dynamical decoupling is also

reported in studies where a magnetic field is used to induce stripes (Schafgans *et al.*, 2010; Wu *et al.*, 2011).

To explain the phenomenon of two-dimensional superconductivity in the stripe-friendly cuprates, a proposal for a new state of matter was put forward by Berg *et al* (Berg *et al.*, 2007, 2009), the so-called Pair Density Wave (PWD). In a PWD, superconductivity does not compete nor coexist with CDW and SDW, but it is intertwined with these density waves. The order parameter for this state describes a paired state with non-zero wave vector, $\vec{q}$, and breaks the translational symmetry of the underlying lattice. This is in contrast to more conventional *s*-wave or *d*-wave superconductors in which the pairing is spatially uniform and consequently the paired state has a net zero momentum. In (Berg *et al.*, 2007), the authors also speculate that the pseudogap state of cuprates might be associated with a fluctuating PDW state.

The PDW state is a promising candidate for explaining some of the properties of the underdoped cuprates. In this thesis, we will focus on a unidirectional PDW where the translational symmetry is broken only in one direction. We refer to this case as a π-striped superconductor. Here π denotes the anti-phase nature of modulations in the superconducting order parameter. The rest of this chapter[1] is organized as follows: in the next section, we introduce a mean field Hamiltonian associated with the π-striped superconducting model. Next, the method we use to find the DOS and spectral properties of this model at zero magnetic field is described. Finally, we will report the calculated properties of the model. This chapter provides some of the back-

---

[1]The results presented in this chapter are published in Physical Review B (Zelli *et al.*, 2011)

ground information that one needs to understand the subsequent chapters of this thesis.

2.2 The Model and Method

The two-dimensional tight-binding model for a superconductor with nearest neighbor singlet pairing is described by the following mean-field Hamiltonian (Baruch and Orgad, 2008)

$$H = H_0 + \sum_{i,\delta} \{ \Delta_{i\delta} [c_{i\uparrow}^{\dagger} c_{i+\delta\downarrow}^{\dagger} - c_{i\downarrow}^{\dagger} c_{i+\delta\uparrow}^{\dagger}] + H.C. \} \qquad (2.1)$$

where $c_{i\sigma}^{\dagger}$ ($c_{i\sigma}$) creates (annihilates) an electron with spin σ on site i and $\Delta_{i\delta}$ is the pairing potential associated with the link between nearest neighbor sites, i and $i + \delta$. The first term of the Hamiltonian is the kinetic part of the Hamiltonian, denoted by H_0, and is given by

$$H_0 = -\sum_{i,\delta,\sigma} t c_{i\sigma}^{\dagger} c_{i+\delta,\sigma} - \sum_{i,\delta',\sigma} t_2 c_{i\sigma}^{\dagger} c_{i+\delta',\sigma} - \sum_{i,\sigma} \mu c_{i\sigma}^{\dagger} c_{i,\sigma} \qquad (2.2)$$

where δ and δ' are assumed over 4 nearest and second nearest neighbor sites, t (t_2) is the nearest (second nearest) neighbor hopping energy and the chemical potential is denoted by μ. In this thesis, the hopping energies are treated as constants and can be taken out of the summation. H_0 has the dispersion $\epsilon_0 = -2t(\cos(k_x) + \cos(k_y)) - 4t_2 \cos(k_x)\cos(k_y) - \mu$ in k space. For simplicity, we set $t_2 = 0$ for most of this thesis unless otherwise stated.

In the pairing part of the Hamiltonian, $\Delta_{i\delta}$ is the order parameter which specifies the pairing on nearest neighbor bonds in real space. The Hamiltonian

describes a uniform d-wave superconductor if $\Delta_{i\delta} = \Delta$ for $\delta = \pm\hat{x}$ and $\Delta_{i\delta} = -\Delta$ for $\delta = \pm\hat{y}$. The most essential feature of a d-wave superconductor is its nodal behavior where the low-energy DOS vanishes linearly with energy. This was briefly discussed in chapter 1.

For a model of a π-striped superconductor, the pairing interaction is modulated in the x direction and is given by

$$\begin{cases} \Delta_{i\delta} = \Delta \cos(q_x(x - 1/2 \pm 1/2)) & \text{if } \delta = \pm\hat{x} \\ \Delta_{i\delta} = -\Delta \cos(q_x(x - 1/2)) & \text{if } \delta = \pm\hat{y}. \end{cases} \quad (2.3)$$

The superconducting condensate for the proposed model occurs at a nonzero wave vector. By setting $q_x = \pi/4$, the Hamiltonian describes a system with a d-wave-type order parameter that has a sinusoidal modulation with 8-site periodicity in the x direction. The presence of a modulated gap with wavevector $2\pi/8$ will induce a charge modulation of twice this wavevector since the charge density is sensitive to the gap magnitude, but not to the sign. This 4 lattice constant periodicity for the charge stripe structure is consistent with the experimental measurements. Due to the periodic modulation of the order parameter, a particle with wave vector $\vec{k}$ is coupled to ones with wave vectors $-\vec{k} \pm \vec{q_x}$. We shall see that this property of a striped superconductor has crucial effects on its low-energy properties.

There are two possible stable configurations for the order parameter of the π-striped superconducting model. One configuration is the site-centered configuration in which the node of the modulation lies on a site. The other one is the bond-centered configuration in which the node lies on a bond. The calculations in this work are done for the latter configuration which is shown
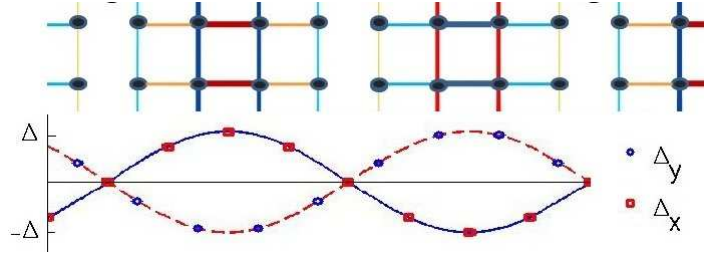
Figure 2.1 Position dependence of the pairing gap for the bond-centered configuration using color coding on bonds. The lower part of the figure shows the varying gap amplitude as a function of x.

in Fig. 2.1. However, the qualitative behavior of the system in the presence of a magnetic field is similar for the site-centered case.

Now, we derive how particles are coupled in k-space for a π-striped superconductor. We start with the interaction part of the Hamilton for a π-striped superconductor with the bond-centered configuration. For simplicity, we use a notation for the creation and annihilation operators that specifies the coordinates of the site they operate on and write

$$H' = \sum_{x,y} \Delta \{\cos(q_x x)[c^\dagger_{x,y\uparrow} c^\dagger_{x+1,y\downarrow} + c^\dagger_{x+1,y\uparrow} c^\dagger_{x,y\downarrow}] \tag{2.4}$$

$$- \cos(q_x(x-1/2))[c^\dagger_{x,y\uparrow} c^\dagger_{x,y+1\downarrow} + c^\dagger_{x,y+1\uparrow} c^\dagger_{x,y\downarrow}] + H.C.\}.$$

Substituting $c_{x,y\sigma} = \frac{1}{\sqrt{N}} \sum_k e^{i(k_x x + k_y y)} c_{k\sigma}$ where σ is the spin sign, we have

$$H' = \frac{1}{N} \sum_{kk'} \sum_{x,y} \frac{\Delta}{2} \{((e^{iq_x x} + e^{-iq_x x})(e^{ik'_x} + e^{ik_x}) e^{i(k_x x + k_y y)} e^{i(k'_x x + k'_y y)} c^\dagger_{k\uparrow} c^\dagger_{k'\downarrow}$$

$$\tag{2.5}$$

$$-(e^{iq_x(x-1/2)} + e^{-iq_x(x-1/2)})(e^{ik'_y} + e^{ik_y}) e^{i(k_x x + k_y y)} e^{i(k'_x x + k'_y y)} c^\dagger_{k\uparrow} c^\dagger_{k'\downarrow} + H.C.\}$$

Performing the summation over position yields

$$H' = \sum_k \frac{\Delta}{2}\{[(e^{-i(k_x+q_x)} + e^{ik_x}) - e^{-iq_x/2}(e^{-ik_y} + e^{ik_y})]c_{k\uparrow}^\dagger c_{-k-q_x\downarrow}^\dagger \qquad (2.6)$$

$$+[(e^{-i(k_x-q_x)} + e^{ik_x}) - e^{iq_x/2}(e^{-ik_y} + e^{ik_y})]c_{k\uparrow}^\dagger c_{-k+q_x\downarrow}^\dagger + H.C.\}.$$

Simplifying the above expression, we get

$$H' = \sum_k \Delta\{e^{-iq_x/2}[\cos(k_x + q_x/2) - \cos(k_y)]c_{k\uparrow}^\dagger c_{-k-q_x\downarrow}^\dagger \qquad (2.7)$$

$$+e^{iq_x/2}[\cos(k_x - q_x/2) - \cos(k_y)]c_{k\uparrow}^\dagger c_{-k+q_x\downarrow}^\dagger + H.C.\}.$$

Eq. (2.7), the pairing part of the mean-field Hamiltonian in k-space, shows that, for $q_x = \pi/4$, each wave vector k is only coupled to 7 other wave vectors.

2.3 Bogoliubov-de Gennes Mean Field Theory

In this section, we describe how to solve the Hamiltonian of Eq. (2.1). To do so, we use the Bogoliubov transformation to write the annihilation operators as

$$c_{i\uparrow} = \sum_n u_n(i)\gamma_{n\uparrow} - v_n(i)^*\gamma_{n\downarrow}^\dagger \qquad (2.8)$$

$$c_{i\downarrow} = \sum_n u_n(i)\gamma_{n\downarrow} + v_n(i)^*\gamma_{n\uparrow}^\dagger \qquad (2.9)$$

where $\gamma_{n\sigma}^\dagger$ and $\gamma_{n\sigma}$ are quasiparticle operators that obey fermionic anti-commutation relations. The idea of the unitary transformation is to cast Eq. (2.1) in the

form

$$H = \sum_{n\sigma} \epsilon_n \gamma_{n\sigma}^\dagger \gamma_{n\sigma} + E_0, \tag{2.10}$$

where E_0 is the ground state energy and ϵ_n is the energy of the n-th quasiparticle excitation. This implies that $\gamma_{n\sigma}^\dagger$ is an operator that creates a quasiparticle with energy ϵ_n and spin σ. In order to satisfy Eq. (2.10), the space dependent functions u and v in 2.8 and 2.9 must satisfy the so-called BdG equations given by

$$\epsilon_n u_n(i) = -t \sum_\delta u_n(i+\delta) - \mu u_n(i) + \sum_\delta \Delta_{i\delta} v_n(i+\delta), \tag{2.11}$$

$$\epsilon_n v_n(i) = t \sum_\delta v_n(i+\delta) + \mu v_n(i) + \sum_\delta \Delta_{i\delta}^* u_n(i+\delta). \tag{2.12}$$

These can be expressed in short by the following eigenvalue equation

$$H_{BdG} \begin{pmatrix} u_n \\ v_n \end{pmatrix} = \begin{pmatrix} \hat{h} & \hat{\Delta} \\ \hat{\Delta}^* & -\hat{h}^* \end{pmatrix} \begin{pmatrix} u_n \\ v_n \end{pmatrix} = \epsilon_n \begin{pmatrix} u_n \\ v_n \end{pmatrix}. \tag{2.13}$$

where H_{BdG} is a Hermitian operator and is called the BdG Hamiltonian. According to 2.11 and 2.12, $\hat{h}$ and $\hat{\Delta}$ operators are given by

$$\hat{h} = -t \sum_\delta \hat{s}_\delta - \mu \tag{2.14}$$

$$\hat{\Delta} = \sum_\delta \Delta_{i\delta} \hat{s}_\delta \tag{2.15}$$

where $\hat{s}_\delta$ is defined as the operator, $\hat{s}_\delta u(r) = u(r+\delta)$. One important property of the BdG Hamiltonian is that, if $\begin{pmatrix} u_n \\ v_n \end{pmatrix}$ is an eigenfunction of H_{BdG} with

eigenvalue ϵ_n, then $\begin{pmatrix} -v_n^* \\ u_n^* \end{pmatrix}$ is also an eigenfunction of the Hamiltonian with eigenvalue $-\epsilon_n$. So we only need to use the positive energy solutions in calculation of various physical properties such as DOS.

2.3.1 Translational Symmetry and Bloch Theorem

Performing numerical calculations, one is limited by computational facilities such as speed and memory. From a computational physicist's point of view, diagonalizing large matrices is perhaps the most computationally challenging task. This is because the time it takes to diagonalize a matrix goes approximately as the third power of the linear size of the matrix. Hence, to deal with large systems, one often use approximating methods such as Monte Carlo simulations. In this thesis, we solve our model by an exact diagonalization of the Hamiltonian which is possible only because of the translational symmetry in our model. Due to this property, we block diagonalize the Hamiltonian to greatly reduce the computational time. The translational symmetry is mathematically expressed as

$$[H, \hat{T}_{\vec{R}}] = 0 \tag{2.16}$$

where $\hat{T}_{\vec{R}}^\dagger = e^{i\hat{p}\cdot\vec{R}/\hbar}$ is the translation operator. From the commutation relation, when $\hat{T}_{\vec{R}}$ operates on an eigenfunction of the Hamiltonian ψ, it gives

$$\hat{T}_{\vec{R}}^\dagger \psi_k(r) = \psi_k(r + \vec{R}) = e^{ik\cdot\vec{R}}\psi_k(r), \tag{2.17}$$

where $\vec{k}$ is an index called the Bloch wave vector. Equation (2.17) is Bloch's theorem and states that the an eigenfunction of a Hamiltonian gains a phase

factor when it is shifted by $\vec{R}$ provided that the operator $\hat{T}_{\vec{R}}$ leaves the Hamiltonian invariant.
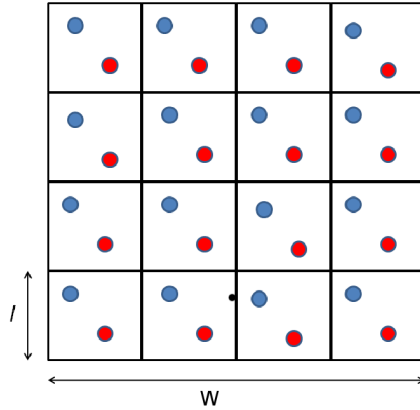
Figure 2.2 A two dimensional system with periodic boundary conditions having a square unit cell of linear size l. The red and blue dots denote the presence of an arbitrary intracell potential inside each unit cell but the same for all unit cells.

What does the Bloch theorem mean for our tight-binding calculations? Assume we have a system with linear size W, so that there are W^2 sites in the system. For simplicity, we assume square unit cells with linear size l as shown in Fig. 2.2 and apply periodic boundary conditions to the system. We have Bloch wavevectors, $\vec{k}$, given by $k_x = \frac{2\pi l}{W}m$ and $k_y = \frac{2\pi l}{W}n$ where m and n are integers ranging from zero to $\frac{W}{l} - 1$. The total number of wavevectors is $M^2 = (\frac{W}{l})^2$.

Next we write down the interactions for a reference unit cell and one of the Bloch wavevectors. When writing the inter-unit-cell interactions, we use the Bloch theorem so that the wave function outside the reference unit cell can be shifted back to the the reference unit cell by providing it with the corresponding Bloch phase. One can think of this approach block-diagonalizing the big matrix with linear size W to M^2 smaller matrices with linear size l.

If the Hamiltonian contains pairing interactions, then one needs to solve the BdG Hamiltonian of type (2.13). This means that, for a system with linear size W and unit cells with linear size l, we need to diagonalize M^2 matrices with linear size $2l$. The wave function can be written as

$$\begin{pmatrix} u_n(i + \vec{R}) \\ v_n(i + \vec{R}) \end{pmatrix} = e^{i\vec{k}\cdot\vec{R}} \begin{pmatrix} u_n(i) \\ v_n(i) \end{pmatrix} \tag{2.18}$$

Then, as described above, $\hat{h}$ and $\hat{\Delta}$ operators are only defined for the sites inside the reference unit cell. For each Bloch wavevector, k, when $\hat{s}_\delta$ in $\hat{h}$ and $\hat{\Delta}$ takes the operand outside the unit cell, then the operator $\hat{s}_\delta$ in 2.14 and 2.15 needs to be replaced by

$$\begin{cases} e^{ik_x}\hat{s}_{\delta - l\hat{x}} & \text{if } \delta = \hat{x} \\ e^{-ik_x}\hat{s}_{\delta + l\hat{x}} & \text{if } \delta = -\hat{x} \\ e^{ik_y}\hat{s}_{\delta - l\hat{y}} & \text{if } \delta = \hat{y} \\ e^{-ik_y}\hat{s}_{\delta + l\hat{y}} & \text{if } \delta = -\hat{y}. \end{cases} \tag{2.19}$$

These conditions make sure that we only need the wave function within the unit cell to perform our calculation for each Bloch state k.

2.4 Density of States and Spectral Function

In principle, within the mean field approach, one can calculate the various properties of a superconducting system using the solutions to the BdG Hamiltonian. Two properties that are often calculated are the density of states and the spectral weight function. Both properties are defined based on the Green's

function (Takigawa *et al.*, 2002). The local density of states is given by

$$D(i, \epsilon) = 2 \sum_{n=1}^{(Ml)^2} [|u_n(i)|^2 \delta(\epsilon - \epsilon_n) + |v_n(i)|^2 \delta(\epsilon + \epsilon_n)] \qquad (2.20)$$

where l^2 is the number of sites in one unit cell and M^2 is the number of unit cells. Note that i's here can be any site in the entire system and ϵ_n's are restricted to the positive-energy solutions of the BdG Hamiltonian. Due to translational symmetry, the local density of states is the same for translationally equivalent sites in all unit cells.

The spectral weight function in the extended Brillouin zone (BZ) is given by

$$A(k, \epsilon) = \frac{2}{(Ml)^2} \sum_{n=1}^{(Ml)^2} [|u_n(k)|^2 \delta(\epsilon - \epsilon_n) + |v_n(k)|^2 \delta(\epsilon + \epsilon_n)] \qquad (2.21)$$

where $u_n(k)$ $(v_n(k))$ is the Fourier transform of $u_n(i)$ $(v_n(i))$ (Garg, 2006). The k's are the wavevectors in an extended BZ and differ from the Bloch wavevector in the previous section, which are the wavevectors in the reduced BZ. For a π-striped superconductor, to go to the reduced BZ scheme, one sums $A(k, \epsilon)$ over the eight coupled k in the extended BZ that can be folded back to one point in the reduced BZ.

The DOS as a function of energy can be obtained from the position average of the local density of states or the wave vector average of the spectral weight function.
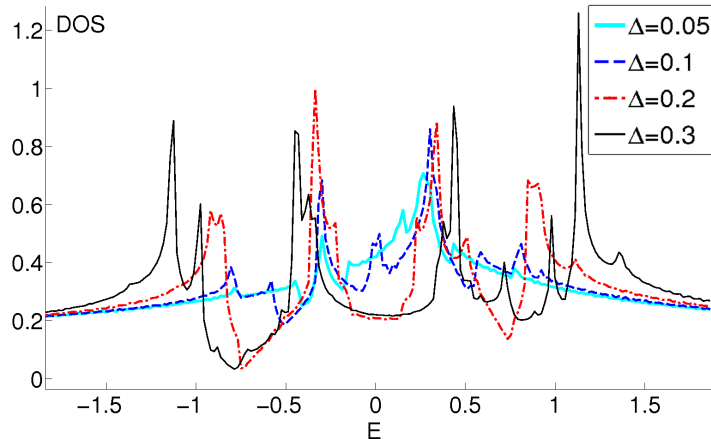
Figure 2.3 DOS of a π-striped superconductor for various values of the pairing gap amplitude. The second nearest neighbor hopping for this DOS calculation is set to zero and the chemical potential μ is adjusted to yield 1/8 doping here and in the following figures unless another value is explicitly stated. Note the finite DOS at zero energy and the complex structure which arises from band folding associated with the strength of the periodic interaction as discussed in the text.

2.5   Results

We solve the Hamiltonian of Eq. (2.1) for a π-striped superconductor in zero magnetic field by diagonalizing the BdG Hamiltonian (2.13) (de Gennes, 1989). The order parameter for a π-striped superconductor is given in Eq. (2.3). The DOS of a homogeneous d-wave superconductor vanishes linearly at $E = 0$. In contrast, a π-striped superconductor has a non-zero DOS at zero energy (Baruch and Orgad, 2008). The low-energy dependence of the DOS for various values of the pairing gap amplitude, Δ, is shown in Fig. 2.3. All the energies are written in units of the nearest neighbor hopping t which is set to 1. The chemical potential, μ, here and for the remainder of this thesis is adjusted to yield 1/8 doping unless another value is explicitly stated.

It is useful to compare and contrast the Δ dependence of the DOS shown in Fig. 2.3 to that of the one-electron spectral weight shown in Fig.
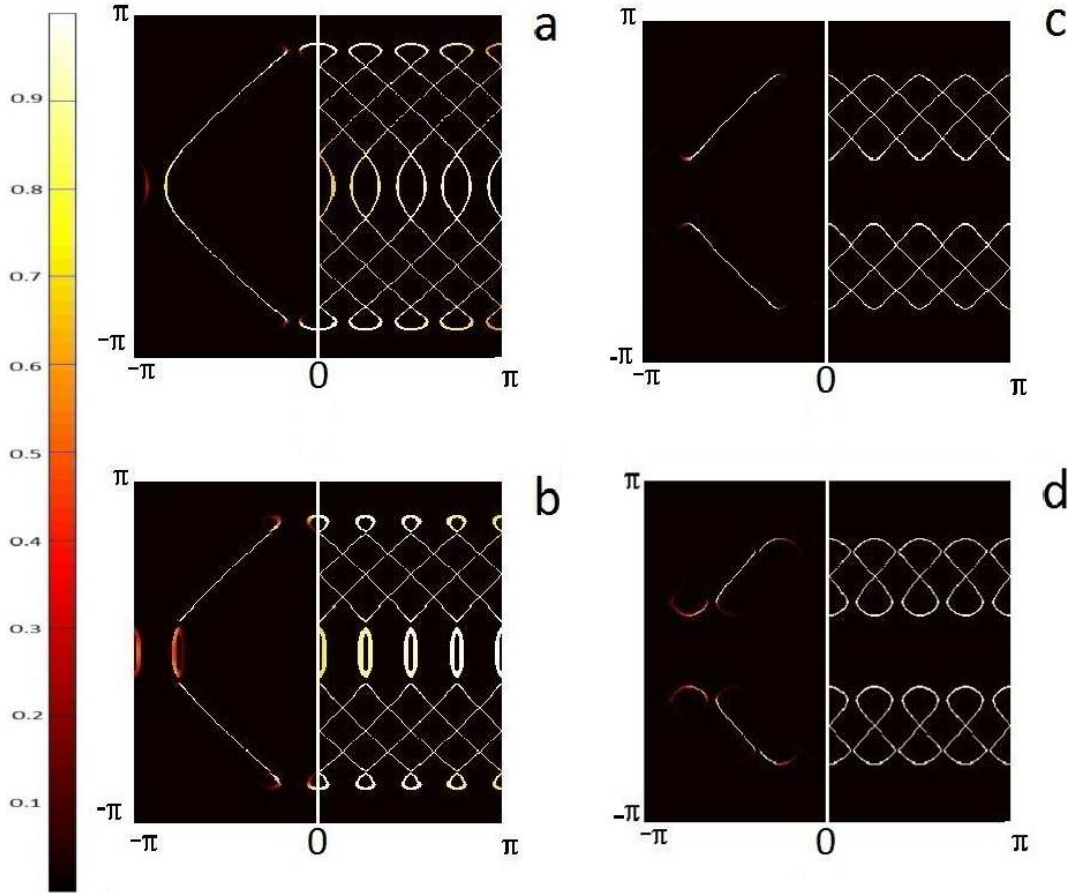
Figure 2.4 The spectral weight (left) and FS (right) for four values of the pairing gap Δ a) 0.05, b) 0.1, c) 0.2 and d) 0.4 in half of the extended BZ. The colorbar applies only to the spectral weight.

2.4. For small Δ, small gaps open in the unperturbed FS segments that can be connected by q_x as shown in Fig. 2.4(a). Consequently the DOS at zero energy does not change significantly with respect to the unperturbed case. For values of Δ in the approximate range $0.07 \lesssim \Delta \lesssim 0.13$, the pairing gap has become strong enough to create two sets of closed loops as can be seen in Fig. 2.4(b) for $\Delta = 0.1$. The Fermi velocity associated with these loops is small and consequently they contribute considerably to the DOS at zero energy. This is why there is a peak in the DOS for $\Delta = 0.1$. For intermediate values of Δ, in

the approximate range ($0.14 \lesssim \Delta \lesssim 0.25$), the loops are gapped out and the peak disappears. In this range, the spectral weight exhibits Fermi arcs with two very small gaps. This is shown in Fig. 2.4(c). For even larger Δ, the gaps within the Fermi-arc-shaped spectral weight become larger and the shape of the FS in the repeated BZ scheme appears as figure-8-shaped loops as shown in Fig. 2.4(d) for $\Delta = 0.4$.
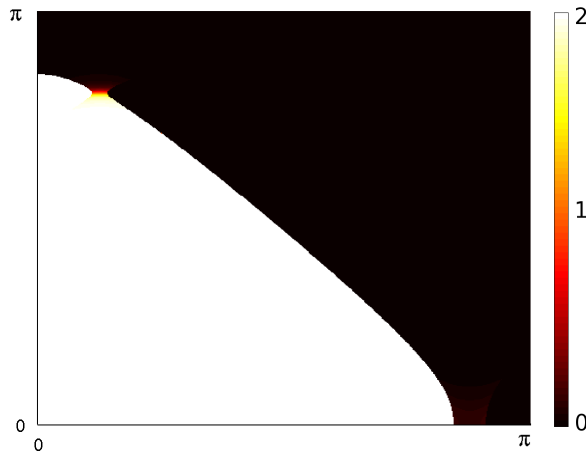
Figure 2.5 The momentum occupation function for $\Delta = 0.02$ and $\mu = -0.23$ corresponding to 1/8 doping.

In Fig. 2.5, we show the momentum occupation function for $\Delta = 0.02$ at 1/8 doping. The function is defined as

$$n(k) = \int_{-\infty}^{0} A(k, \epsilon) \tag{2.22}$$

where $A(k, \epsilon)$ is the spectral function of Eq. (2.21). It shows the occupation of the states in the quadrant of the extended BZ at zero temperature. The momentum occupation function is the same as that of the $\Delta = 0$ case except near the gaps. Note that there are four gaps in the original FS for the parameters used and only one gap is shown in the quadrant of the BZ. The u's and the
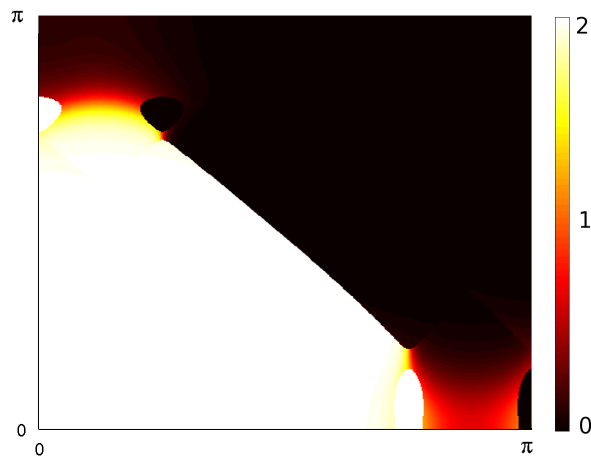
Figure 2.6 The momentum occupation function for $\Delta = 0.1$ and $\mu = -0.25$ corresponding to 1/8 doping.

v's, the Bogoliubov quasiparticle amplitudes, jump sharply on crossing the FS as they do for a normal metal, rather than varying smoothly as they do near the gapped regions of a d-wave superconductor. In that sense, most of the FS acts like a metallic FS.
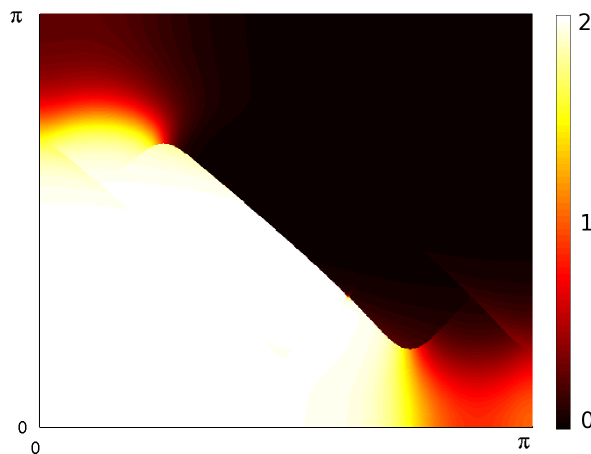
Figure 2.7 The momentum occupation function for $\Delta = 0.2$ and $\mu = -0.3$ corresponding to 1/8 doping.

Fig. 2.6 shows the momentum occupation function for $\Delta = 0.1$ at 1/8

Figure 2.8 The momentum occupation function for $\Delta = 0.4$ and $\mu = -0.36$ corresponding to 1/8 doping.

doping. It is apparent that the u's and the v's are mixed near the anti nodal points but still rather metallic near the center of the Fermi arcs. In fact this is the case for even larger Δ as shown in Fig. 2.7 for $\Delta = 0.2$. As Δ increases, the part of the FS where the u's and v's are essentially 0 or 1 at $T = 0$ shrinks. This is illustrated in Fig. 2.8 for $\Delta = 0.4$.

2.6   Periodic Andreev state
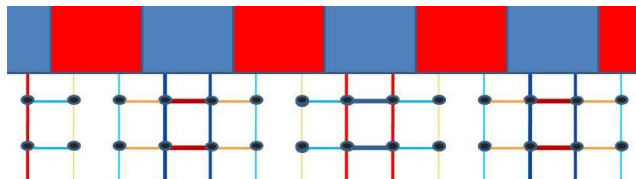
Figure 2.9 High (red stripe) and low (blue stripe) density structure of the low-energy particles relative to the modulated d-wave gap. High (low) density is indicated by a red (blue) stripe.

In this section, a type of Andreev state that is seen for the low-energy particles (holes) in the absence of a magnetic field and persists in the presence

of a magnetic field is discussed. We have already examined how the spectral weight of the low-energy states of a π-striped superconductor changes as the pairing amplitude Δ is varied. We can also look at the real space representation of these states. Our main finding is that, for intermediate values of Δ where the shape of Fermi arc is assumed in the spectral function (see Fig. 2.4), the real space representation of the low-energy states exhibits a periodic stripe structure with the periodicity of four lattice sites. The stripe structure corresponds to higher and lower density of low-energy electrons and holes. Each stripe has a width of two lattice constants and the higher density stripes are located exactly where the order parameter is minimum as shown in Fig. 2.9. The density ratio of the higher density stripes to the lower density ones increases as Δ increases. The ratio is approximately 1.5 for $\Delta = 0.2$ and 2 for $\Delta = 0.4$. This stripe structure occurs not only at the Fermi energy, but also near the Fermi energy.

The origin of these stripes is simple. They are formed due to the constructive interference of the low-energy electron (hole) waves with their doubly Andreev scattered counterparts. Since the probability of being Andreev scattered twice increases with Δ, the density difference between higher and lower density stripes increases accordingly. One can think of the stripe structure as a periodic Andreev state. For a wave vector at the end-points of the Fermi arcs, the doubly scattered wave vector is also located at the end-point of another Fermi arc. This means that the weights of both interfering waves are large and as a result they contribute considerably to the formation of the stripe structure. Moving toward the center of the Fermi arc, the coupling interaction decreases and the periodic Andreev structure is less likely to be formed. This is why, as mentioned in the paper by Baruch and Orgad (2008), the stripe

structure is mainly due to states near the end-points of the Fermi arcs.

Chapter 3

The Mixed State of a π-striped Superconductor

3.1 Introduction

In Chapter 1, we discussed the result of quantum oscillation experiments on the cuprates. We noted that the QO area is only about 2% of the BZ, much smaller than what one expected. In addition, the existence of FS pockets that presumably gives rise to quantum oscillations (QO) is not consistent with the Fermi arcs observed in ARPES. There have been different proposals to explain these key results of QO in the cuprates (Pereg-Barnea *et al.*, 2009; Elfimov *et al.*, 2008; Alexandrov, 2008). Among them, studies based on Fermi surface (FS) reconstruction approach are the most promising. In general, the FS of the undistorted lattice can be reconstructed into a number of smaller hole and electron pockets due to the breaking of translational symmetry. Interestingly, in a recent study, QO are reported to be the strongest at 1/8 doping which suggests that the breakdown of translational symmetry due to stripes

is responsible for the phenomenon (Laliberte *et al.*, 2011). Theoretically, both charge and spin density waves result in small electron pockets and could account for the quantum oscillations (Millis and Norman, 2007; Harrison, 2009; Yao *et al.*, 2011). However, the essential problem with both approaches is that they result in multiple pockets, whereas in most measurements only a single frequency has been observed. Moreover, the electron pockets found by these studies are located in antionodal parts of the BZ where ARPES sees large gaps. This means that the problem of reconciling the ARPES and QO experiments still exists.

In addition, thermodynamic measurement of YBCO shows that the $\sqrt{H}$ trend in the magnetic field dependence of the specific heat persists through the resistive transition (Riggs *et al.*, 2011). The $\sqrt{H}$ dependence, which is consistent with a nodal FS, suggests that a fully developed d-wave pairing is still present after the resistive transition (Volovik, 1993). In the same study, it has been argued that these FS reconstruction approaches produce a specific heat that is too large to be consistent with experimental values (Riggs *et al.*, 2011).

In this thesis, we use a variation of the previous FS reconstruction studies to explain QO in the cuprates. The idea is to investigate whether a π-striped superconductor, that is conjectured to be stable at strong enough fields, could give rise to QO. This approach is different from previous FS reconstruction studies in which the resistive state of the cuprate are treated like a metal with no pairing potential present. It is the aim of this chapter[1] to calculate the low-energy DOS of a π-striped superconductor in the presence

---

[1]The results presented in this chapter are published in Physical Review B (Zelli *et al.*, 2011)

of a magnetic field and see whether Landau levels are formed near the Fermi
energy for this model.
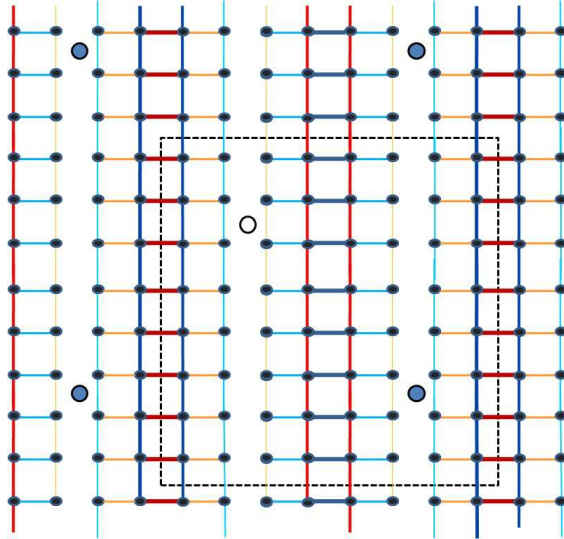
Figure 3.1 Position dependence of the pairing gap for the bond-centered con-
figuration using color coding on bonds. The circles in the middle of plaquettes
specify the positions of vortices for a $l = 8$ magnetic field unit cell whose
boundary is shown by the dashed line. In the singular gauge, the vortices at
white (dark) circles are only seen by particles (holes). The lower part of the
figure shows the varying gap amplitude as a function of x.

3.2   A π-striped Superconductor in a Magnetic field

In chapter 2, we discussed the DOS and spectral weight properties of the π-
striped superconductor at zero magnetic field. In this section, we will examine
the structure of the DOS in the presence of a magnetic field. The magnetic
field is incorporated into the model using the Franz-Tesanovic singular gauge
transformation (Franz and Tešanović, 2000; Vafek *et al.*, 2001). This gauge
transformation is discussed in appendix B. In this approach, one needs to

introduce magnetic unit cells that have two vortices each; one is seen only by particles and the other seen only by holes. In our case, we work with square magnetic unit cells with linear size l, where l is measured in units of the lattice constant. The magnetic field is inversely proportional to the area of the unit cell and is given by $B = \phi_0/l^2$ where ϕ_0 is the flux quantum. For example, taking the lattice constant $a = 3.8\text{Å}$, $l = 32$ corresponds to $B = 28$ T. We position the vortices at the nodes of the order parameter, as shown in Fig. 3.1 for the case of $l = 8$. Because of the 8-site periodicity of the pairing potential in our model, l is taken to be an integer multiple of 8. This implies that only discrete values of the magnetic field are accessible when using the method described above.
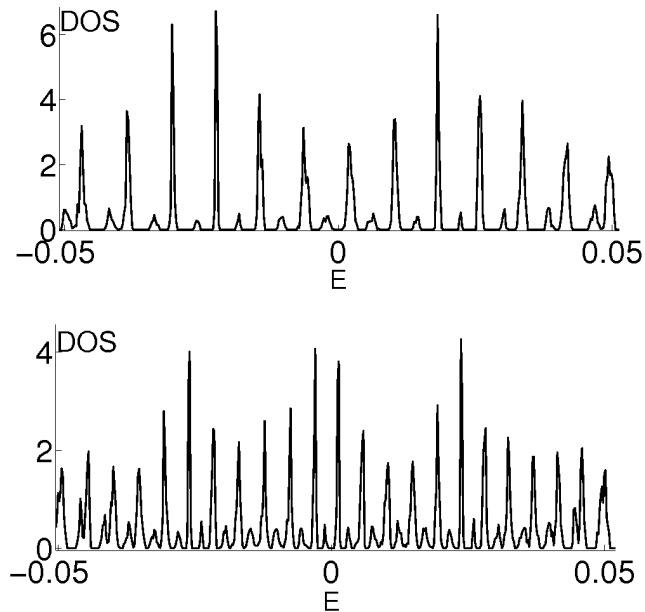
Figure 3.2 Low-energy DOS of a π-striped superconductor with $\Delta = 0.01t$ and $\mu = -0.226$ in the presence of magnetic fields of $l = 24$ (top) and $l = 32$ (bottom).

In this section, we investigate how the DOS structure of the model changes as a function of the pairing amplitude Δ in the presence of a magnetic

field. First, we consider small values of Δ where one can expect to understand the effect of the interaction based on a simple perturbative picture. For $\Delta = 0.01$, the spectral weight in the absence of a magnetic field exhibits only small gaps at four points of the unperturbed FS. It is similar to Fig. 2.4(a) except that the gaps are smaller.

The low-energy DOS structures for $\Delta = 0.01$ and two magnetic fields of $l = 32$ and $l = 24$ are shown in Fig. 3.2. The most striking feature of this figure is the appearance of Landau levels that are equally spaced in energy with the spacing proportional to B. Furthermore, the presence of a small perturbative interaction, Δ, causes the low-energy Landau levels to be slightly broadened and also partially reflected to the other side of the Fermi energy due to particle-hole scattering. In fact, each Landau level for $\Delta = 0$ is split into two peaks (at E and $-E$) with the second peak having much smaller weight for small Δ, as seen in Fig. 3.2. The sum of the number of states in these two peaks equals the degeneracy of a Landau level.

From a semiclassical point of view, particles can keep undergoing Larmor precession by tunnelling through the gaps since the gaps are small for $\Delta = 0.01$. This is the so-called magnetic breakdown phenomenon (Shoenberg, 1984). A particle can also be Andreev scattered as a hole into a state of $-\vec{k} \pm \vec{q}$. This process explains the reflected part of each Landau level with smaller weight in Fig. 3.2. This picture is motivated by the work of Pippard,(Pippard, 1962) who studied the cyclotron motion of nearly free electrons in the presence of a weak periodic potential that induces gaps in the Fermi surface. For this case, when the periodic potential is weak, electrons can tunnel through the gaps, following the unperturbed FS trajectory, or they may be Bragg scattered onto a different cyclotron orbit leading to broadening. The

main difference between Pippard's model and the π-striped superconducting model is that the superconducting periodic potential scatters electrons with wave vector $-\vec{k}$ into holes with wave vector $-\vec{k} \pm \vec{q}$ and vice versa. Thus electrons either tunnel through gaps induced by the periodic potential or scatter into hole states. Note that magnetic breakdown occurs even if the magnitude of the gap in the FS is larger than $\hbar\omega_c$ (Shoenberg, 1984). We will discuss this picture in more detail in chapter 4.

For small to intermediate values of Δ ($0.07 \lesssim \Delta \lesssim 0.13$), for which the FS has well-separated segments (see Fig. 2.4(b)), we do not observe clearly defined Landau levels. This may be the result of broadening and the close spacing of Landau levels due to the large density of states. Furthermore, multiple Fermi surfaces may each give rise to their own sets of Landau levels which are unresolved.
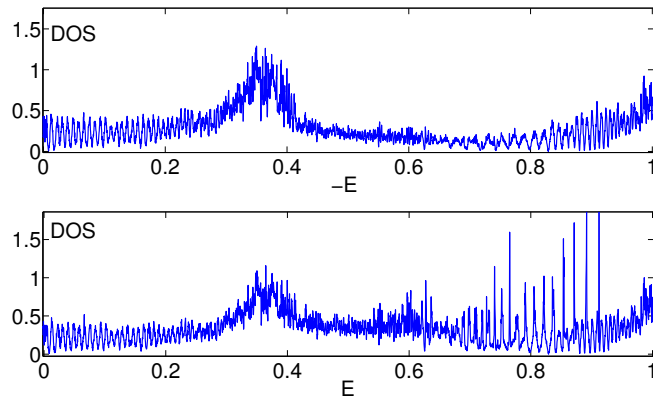
Figure 3.3 DOS for $\Delta = 0.25$ and magnetic field of $l = 32$ shown as a function of positive and negative energies separately. The band structure spans energies from $-4 - \mu$ to $4 - \mu$. However, the DOS is only shown in the $-1 < E < 1$ range.

For intermediate values of Δ ($0.14 \lesssim \Delta \lesssim 0.3$), the shape of the FS is simpler. In this range, the spectral function has significant weight on the parts of the FS that resemble the Fermi arcs observed in ARPES experiments.
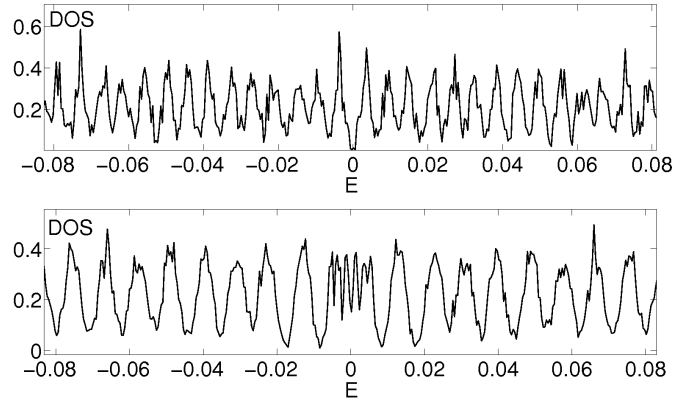
Figure 3.4 Low-energy DOS for $\Delta = 0.25$ and magnetic fields of $l = 40$ (top) and $l = 32$ (bottom).

The DOS for $\Delta = 0.25$ and $l = 32$ is shown in Fig. 3.3 for positive and negative energies up to E $= 1$ separately. Remarkably, we again observe periodic behavior of the low-energy DOS as a function of E with a spacing that varies linearly with B. This is illustrated in Fig. 3.4 for $\Delta = 0.25$ and two values of the magnetic field, $l = 40$ and $l = 32$. Note the splitting of each Landau level into a strong and weak peak seen for small Δ, Fig. 3.2, does not occur in this larger Δ range, where the original large FS is not accessible to the quasiparticles.

In Fig. 3.4, the DOS has a minimum, or possibly a very small gap, at $E = 0$ for $l = 40$. However, for $l = 32$ it appears that the two Landau levels closest to $E = 0$ are joined together and the DOS at $E = 0$ has a nonzero value. In general, we find that, for $l = 8m$ where m is an integer, if m is even, the DOS at $E = 0$ is nonzero and if m is odd, the DOS is zero at $E = 0$. This is a commensurability effect due to the ordered vortex lattice that results in oscillation of the DOS at $E = 0$ as a function of l or $1/\sqrt{B}$ and is discussed further in Sec. 3.4.

The number of states in each peak in Fig. 3.4 is nearly the same as
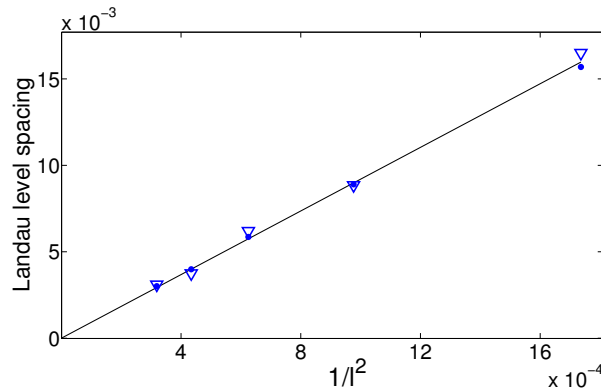
Figure 3.5 Low energy Landau level spacing as a function of $1/l^2$ for $\Delta = 0.25$ and $\mu = -0.3$. The spacing is defined as $E(N)/N$ where $E(N)$ is the minimum in the DOS between the N-th and $N + 1$-th Landau levels and is shown for $N = 2$ (triangle) and $N = 10$ (circle). The line is a linear fit to the data that goes through the origin.

that of a Landau level. In general, in the presence of a magnetic field, the n-th peak on the $E <$ side of $E = 0$ can have a degeneracy slightly different from a Landau level degeneracy. However, the n-th peak on the $E >$ side compensates so that the number of states of the two peaks together is always twice that of a Landau level. This shows that the Landau levels are a coherent mixture of particles and holes together and the particle-hole scattering is playing a role in the formation of the Landau levels. The reason for the small difference of the number of states in each peak from the exact degeneracy of a Landau level is that the low-energy DOS in the absence of a magnetic field is asymmetric around $E = 0$ except at half filling, as shown in Fig. 3.6.

We have calculated the spacing of the low energy Landau levels for a wide range of fields for $\Delta = 0.25$ and $\mu = -0.3$ as shown in Fig. 3.5. The LL spacing can be defined as $E(N)/N$ where $E(N)$ is the minimum in the DOS between the N-th and $N + 1$-th Landau levels (counting from $E = 0$) and is essentially independent of N provided $E(N) \lesssim 0.5\Delta$. Fig. 3.5 demonstrates

the spacing as a function of $1/l^2 \propto B$ for $N = 2$ and $N = 10$. The slope of the Landau level spacing versus B is inversely proportional to the DOS at $E = 0$. By comparison, we find that the slope is about half as large and the DOS at $E = 0$ about twice as large for $\Delta = 0$.
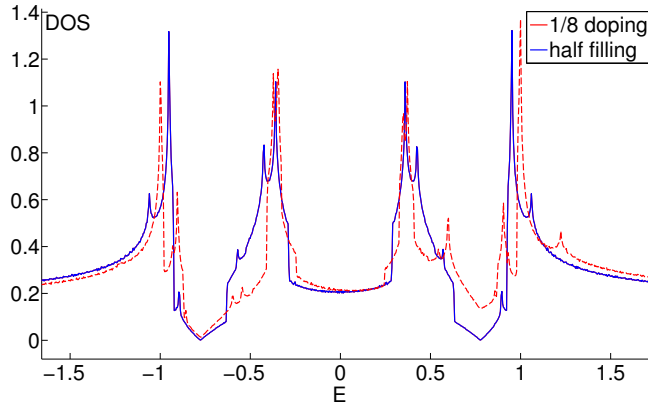
Figure 3.6 The DOS structure in the absence of a magnetic field for $\Delta = 0.25$ and two dopings. Note the asymmetry at low E for 1/8 doping.

It is worth contrasting the behavior of the π-striped superconductor, Fig. 3.4, to the DOS structure of a homogeneous d-wave superconductor. For the latter, at half-filling, peaks that are not equally spaced are formed in the low-energy DOS and the spacing scales as $\sqrt{B}$ around $E = 0$ (Vafek et al., 2001). This is a consequence of the nodal behavior at the Fermi energy. Therefore, quantum oscillations periodic in $1/B$ are not expected for a d-wave superconductor. For the remainder of this paper we refer to each peak of the type shown in Fig. 3.4 (that is, equally spaced with a spacing proportional to B) as a Landau level. The fact that there is only one set of Landau levels and the number of states in each peak is equal to that of a Landau level suggests that all parts of the FS participate in the formation of low-energy Landau levels.

It is unclear why the case of intermediate values of Δ, Fig. 3.4, is

different from the case of very small values of Δ, Fig. 3.2, in which the sum of the degeneracy of the two peaks equals the degeneracy of only one Landau level. One possibility is that this is due to the fact that there are two identical, separate segments of the FS in the reduced BZ assuming that each separate segment gives rise to the formation of peaks with the degeneracy of one LL. Because the two segments are identical, we see the two peaks on top of each other which have a total degeneracy of two LLs.
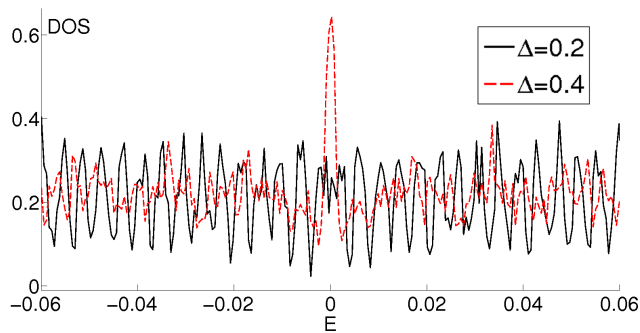
Figure 3.7 Low-energy DOS for $l = 48$ and $\Delta = 0.2$ and $\Delta = 0.4$. Landau levels are suppressed for $\Delta = 0.4$ but a sharp peak around $E = 0$ appears.

Next we increase Δ to even larger values. Although Landau levels are observed in the low-energy DOS in the intermediate Δ regime ($0.14 \lesssim \Delta \lesssim 0.3$), for larger Δ ($\Delta \gtrsim 0.35$), the Landau levels disappear. Fig. 3.7, shows a comparison of the low-energy DOS for $\Delta = 0.2$ and $\Delta = 0.4$ in the presence of a magnetic field $l = 48$. The DOS for $\Delta = 0.4$ shows structure but no clear Landau levels. The sharp peak at $E = 0$ can be attributed to the commensurability effect. This is further discussed in appendix 3.4.

As Δ is increased, large gaps appear within the Fermi arcs. This is seen in the spectral function, shown in Fig. 2.4(d) for $\Delta = 0.4$ and zero magnetic field. If one assumes that the semiclassical process of the formation of the Landau levels (Anderson, 1998) involves tunnelling of particles (holes)

across the gaps within the Fermi arcs, one expects the magnetic breakdown phenomenon not to occur if the gaps are too large. This may explain why the Landau levels are suppressed for very large Δ. Nevertheless, it is not clear whether the suppression of the LLs is due to the appearance of large gaps in the FS or to a strong commensurability effect. We will return to the case of very large Δ in chapter 4.
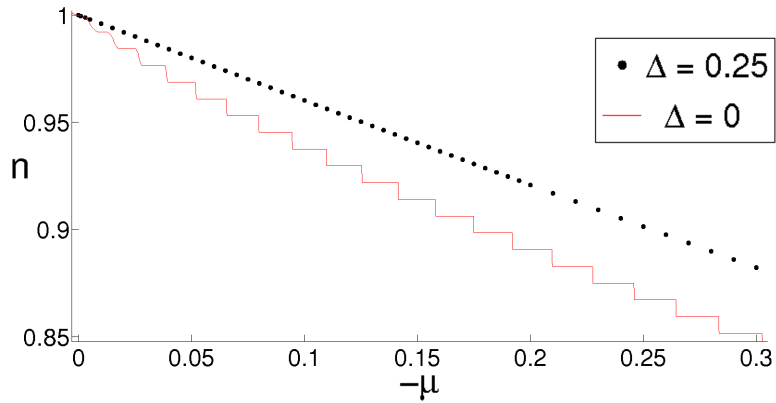
Figure 3.8 Density of electrons versus $-\mu$ for the magnetic field of $l = 16$ and two cases of $\Delta = 0.25$ and $\Delta = 0$. Unlike $\Delta = 0$, the density does not exhibit a stepped behavior for $\Delta = 0.25$.

Landau-type quantum oscillatory behavior has previously been discussed in the context of a particular model of a 'Fermi-arc metal' (Pereg-Barnea *et al.*, 2009). In that model, parts of the FS of a metal are artificially gapped out by restricting superconducting pairing to the antinodal regions of momentum space in order to get a FS that consists of Fermi arcs. The appearance of LLs in this model is not surprising as both a π-striped superconductor and a Fermi-arc metal have almost all the spectral weight on Fermi arcs. However, the π-striped model, which is based on a specific microscopic mechanism and has no such restriction on pairing, differs from the Fermi-arc metal of (Pereg-Barnea *et al.*, 2009) in that it breaks the translational sym-

metry of the underlying lattice. This means that, unlike the Fermi-arc metal, the one-electron spectral function for a π-striped superconductor has non-zero (but possibly very small) weight along continuous lines in k-space.

The behavior of a π-striped superconductor is strikingly different from that of a metal, in spite of the fact that both exhibit a Fermi surface. In a metal, the particle density n versus μ exhibits a stepped behavior in the presence of a constant magnetic field. In contrast, the particle density in a π-striped superconductor changes smoothly as a function of μ as shown in Fig. 3.8 for a large magnetic field of $l = 16$. Furthermore, we find that the low-energy DOS behavior of the π-striped superconductor is rather insensitive to the change in μ. In other words, no oscillatory behavior of the DOS at $E = 0$ is observed as μ is varied except for finite size effects. This is in contrast to the result for the simple Fermi-arc metal model (Pereg-Barnea *et al.*, 2009). However, experimentally, quantum oscillations are induced by changing the magnetic field, not the chemical potential, and consequently could still be observed for a π-striped superconductor.

3.3   Specific Heat

In this section, we present specific heat calculations in the absence and presence of a magnetic field in order to make connections to experiments on the cuprates. Our analysis in this section is based on the calculation of the Sommerfeld coefficient, γ, which is the slope of the electronic part of the specific heat and a measure of the DOS at low energies. This coefficient is discussed in detail in appendix D. In advance, we note that the $\sqrt{B}$ dependence of γ in the cuprates is not present in the π-striped superconducting model as there is

a finite DOS at $E = 0$. However, it will be shown that some features of the specific heat in the cuprates are consistent with this model. One can calculate the specific heat from the relationship $c = T\frac{\partial S}{\partial T}$. For a system of independent quasiparticles, the entropy is given by (de Gennes, 1989)

$$S = -2k_B \sum_p [f_p \ln f_p + (1 - f_p) \ln(1 - f_p)] \qquad (3.1)$$

where f_p is the Fermi-Dirac distribution function. The details of the specific heat calculation are discussed in appendix D. It should be noted that, in this study, the DOS is not calculated self-consistently as there is no microscopic Hamiltonian defined. Furthermore, for the following calculations, it is assumed that the magnitude of the pairing interaction is constant at low temperatures so that the quasiparticle spectrum is unchanged as temperature increases.

The specific heat at zero field for a π-striped superconductor as a function of temperature is shown in Fig. 3.9 for $\Delta = 0.25$ at 1/8 doping. The slope associated with the linear behavior is $\gamma = 0.70k_B^2 t^{-1}$ per site and is directly proportional to the DOS at $E = 0$, which is $0.21t^{-1}$ per site. The slope is about half of that of $\Delta = 0$ at 1/8 doping. The low-energy specific heat at various fields as a function of temperature is also shown in Fig. 3.9 for $\Delta = 0.25$ and $\mu = -0.3$. As expected, all the curves converge to that of zero field as the temperature increases. However, at very low temperatures, the specific heat behavior for different fields is significantly affected by the commensurability effect. This is seen in the nearly zero slope of the curves for odd m (recall $l = 8m$) as $T \to 0$.

Low temperature electronic specific heat measurements of the cuprates point to a finite DOS at $E = 0$ which is often attributed to the presence of
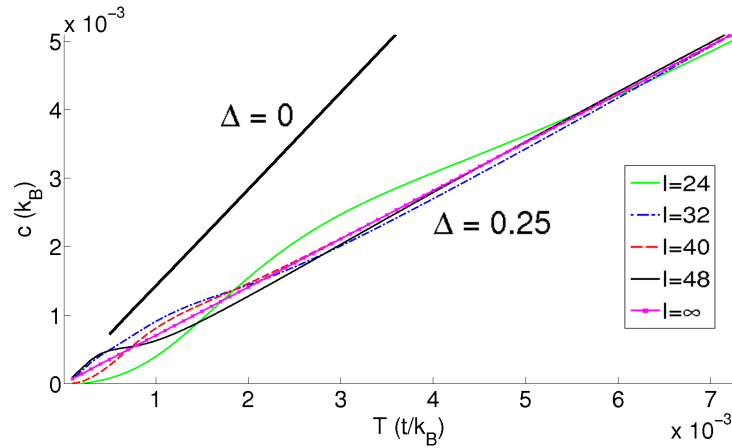
Figure 3.9 Specific heat in the presence of various fields as a function of temperature for $\Delta = 0.25$ and $\mu = -0.3$. The behavior of the curves at very low temperatures is significantly affected by the commensurability effect. The heavy line shows the specific heat in zero field for $\Delta = 0$ and $\mu = -0.225$ corresponding to 1/8 doping. The slope associated with the linear behavior is about twice as the slope for $\Delta = 0.25$ in zero field (noted by $l = \infty$).

disorder in a d-wave superconductor. However, the specific heat measurements of a cuprate (Riggs *et al.*, 2011) indicate a relatively large DOS at $E = 0$ which can not be explained by the presence of disorder. Taking the lattice constant of a typical cuprate to be $a = 3.85\mathring{A}$, the specific heat effective mass becomes $m^*/m = 0.34eV/t$. A rather wide range of values has been used for t (Baruch and Orgad, 2008; Yao *et al.*, 2011). Within a simplified nearest-neighbor hopping only model as used here, we obtain $m^*/m = 1.36$ for $t \approx 0.25eV$ (Goswami *et al.*, 2010). This value corresponds to $\gamma \approx 1.98$ mJ· K^{-2}·mol^{-1} which is consistent with the specific heat measurements for the cuprates in the absence of a magnetic field, $\gamma \approx 1.85$ mJ· K^{-2}·mol^{-1} (Riggs *et al.*, 2011). Instead, if we had taken $t \approx 0.125eV$, we would get $\gamma \approx 3.96$ mJ· K^{-2}·mol^{-1} which corresponds to the specific heat at around 25T where the quantum oscillation phenomenon appears in the cuprates.

Riggs et al. have studied the low temperature specific heat as a function

of magnetic field up to very high fields and observed quantum oscillations (Riggs *et al.*, 2011). This allowed them both to measure the magnitude of the specific heat in what is presumably the normal state, and also to determine the cyclotron effective mass associated with the quantum oscillations. Then, if one assumes the normal state has broken translation symmetry, modelling the arrangement of electron and hole pockets in the Brillouin zone and using the measured cyclotron effective mass, one can estimate what the specific heat should be. The result is much larger than the specific heat that they observe (Riggs *et al.*, 2011; Tesanovic, 2011). This problem was also noted in a theoretical study based on FS reconstruction where the calculated specific heat was larger than the measured value for any reasonable value of t (Yao *et al.*, 2011).

In our calculations for a π-striped superconductor, it was found that, even though there exist several FS pockets in the BZ, a single set of Landau levels is observed above and below the Fermi energy. The relation between the slope of Fig. 3.5, defining the cyclotron effective mass obtained from the spacing of Landau levels, and the DOS at $E = 0$ is the same as for the $\Delta = 0$ case. This implies that, as for the $\Delta = 0$ case, the cyclotron effective mass, m_c, is equal to the specific heat effective mass, m^*, for large values of Δ. Consequently, the quantum oscillations in the specific heat and the magnitude of the specific heat which is observed in Ref. (Riggs *et al.*, 2011) could be consistent with the behaviour of a π-striped superconductor state induced by large magnetic fields, rather than a striped metallic state with no pairing gap as is often assumed. However, as noted earlier, the ideal π-striped model (with no uniform d-wave component) is not expected to give a $\sqrt{B}$ background, which also appears to be a feature of the experiments (Riggs *et al.*, 2011). We will

discuss this feature in the next chapter.

3.4   Commensurability effects

In this section, we discuss the commensurability effect mentioned in Sec. 3.2. We found that the DOS at $E = 0$ exhibits a periodic behavior as a function of l or $1/\sqrt{B}$ for large values of Δ. If m is even, the two vortices in a magnetic unit cell are in perfectly equivalent positions with respect to the spatially modulated gap and the DOS at $E = 0$ is nonzero. In contrast, for odd m, the gap on the right of one vortex is positive but is negative on the right of the other vortex as shown in Fig. 3.1. The DOS at $E = 0$ is zero for odd m.

The same kind of commensurability effect is also seen in a uniform d-wave superconductor (Melikyan and Vafek, 2008). There, due to strong internodal scattering, the DOS at zero energy exhibits a periodic behavior as a function of $k_d l$, where k_d is the k-space half distance between the nearest nodes of the d-wave superconductor. Specifically, depending on whether n is odd or even in $k_d l = \pi n$, the DOS around $E = 0$ shows a linear or gapped behavior. For a π-striped superconductor, the relevant k-space half distance is $\pi/8$ which leads to a periodicity of $\delta l = 16$ for the DOS at zero energy as a function of l. This is consistent with the periodicity that we observe in our calculations. So the commensurability effect seen in a π-striped superconductor is most likely due to interference effects. This suggests that the nonzero DOS at $E = 0$ for even m is due to constructive interference of particle and hole waves, while the gapped behavior for odd m is due to destructive interference.

For very large Δ, a sharp peak develops near $E = 0$ for even m only, as shown in Fig. 3.7. It appears that the origin of the peak can be traced back to
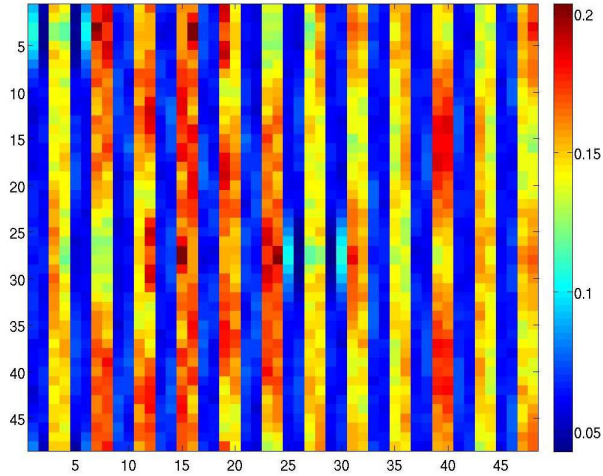
Figure 3.10 Local density of electrons due to the low-energy states within 0.001t of $E = 0$ for $l = 48$ and $\Delta = 0.4$. The vortices are at $(3.5, 3.5)$ and $(27.5, 27.5)$.

the non-zero DOS at $E = 0$ for smaller Δ, and consequently is related to the commensurability effect. The fact that the low-energy Landau levels disappear when the peak at $E = 0$ is sharp suggests that the commensurability effect is competing with the Landau level formation. Figure 3.10 shows the real space representation of the the states under the sharp peak at $E = 0$ where a pattern of stripes of low and high particle density is clearly visible. On average, the ratio of the density of the higher density stripes to the lower density is 2.35 for $\Delta = 0.4$, which is larger than the value 0.2 in the absence of a magnetic field (see Sec. 2.6). It is not clear whether these effects are due to the existence of a strong commensurability effect or due to the presence of large gaps within the Fermi arcs.

3.5   Summary

In this chapter, we have studied the model of a π-striped superconductor in a magnetic field. Our main finding is that Landau levels are seen in the low-energy DOS of the π-striped superconductor for a large range of magnetic fields and pairing amplitudes. This indicates the possibility of quantum oscillations as LLs are a prerequisite for this phenomenon. The low-energy Landau level formation persists even though particle and hole levels are mixed by the pairing interaction. In particular, for large values of the pairing potential, the π-striped superconductor exhibits a unique low-energy Landau level set that is only due to the Fermi arc part of the spectral weight function. In contrast to other studies based on FS reconstruction due to density waves, this is consistent with the ARPES measurements.

One other promising feature of this model is that it does not lead to a specific heat that is too large compared to the experimental values. We found that the cyclotron effective mass, m_c defined based on the LL spacing, is equal to the specific heat effective mass, m^*, for large values of Δ. Note that this feature of a π-striped superconductor is in contrast to other numerical studies based on FS reconstruction where the problem of a too large specific heat has been reported (Yao et $al.$, 2011).

Since our numerical studies are restricted to vortex lattices satisfying $l = 8m$, we cannot change the magnitude of the magnetic field continuously or in small steps. As a result it is not possible, by the method used in this chapter, to find the FS area associated with quantum oscillations that would be observed following the simple formula of Onsager (Onsager, 1952). One might suggest to use a rectangular vortex lattice in order to get more magnetic

field values. However, this does not add enough magnetic point values for the calculation of the quantum oscillation area. Furthermore, there is an ambiguity on how to arrange a rectangular lattice with respect to the modulated order parameter. For example, a rectangular unit cell with 128 sites can either have $l_x = 16$ and $l_x = 8$. These two cases have different commensurability effects and so different low energy DOS. This means that we get two different physical behavior for the same magnetic field.

We can make conjectures about FS areas that might be observed, based on our analysis. We expect that any semiclassical trajectory describing the formation of Landau Levels should have the following characteristics: 1) The trajectory should use all parts of the FS. 2) Andreev scattering needs to occur at least at two points during the Larmor precession because Landau levels are a coherent mixture of particles and holes. 3) Magnetic breakdown is likely involved in Landau level formation because once the gaps within the Fermi arcs become too large, the Landau levels disappear.

It is also useful to compare the behaviour of the π-striped superconductor to the Fermi-arc metal, in which a new mechanism for quantum oscillations is proposed that is not based on FS reconstruction (Pereg-Barnea *et al.*, 2009). For that model, it was shown, based on a semiclassical approach, that the frequency of quantum oscillations is proportional to the Fermi arc length. In the π-striped superconductor, the fact that a quasiparticle with wave vector $\vec{k}$ is coupled to ones with wave vectors $-\vec{k} - \vec{q}_x$ and $-\vec{k} + \vec{q}_x$ provides a different scattering mechanism which changes the semiclassical motion of quasiparticles. Consequently, the semiclassical trajectories of the two studies are expected to be different. Although Landau level formation in the Fermi-arc metal resembles what we have seen in the π-striped model, the DOS at $E = 0$ shows an

oscillatory behavior as a function of μ for the Fermi-arc metal which is absent in our study.

The observation of quantum oscillations corresponding to small Fermi surface pockets supports the scenario of translational symmetry breaking and Fermi surface reconstruction, whether due to charge or spin density waves or to modulation of the d-wave gap. Indeed recent experimental results support the connection between stripe formation and quantum oscillations (Laliberte *et al.*, 2011). Our calculations in this chapter show that a modulated d-wave superconductor can support Landau levels and quantum oscillations. However, we are unable to make detailed comparisons to quantum oscillation experiments because of the restriction to commensurate vortex lattices. One might expect there to be observable differences between quantum oscillations in the presence of charge or spin stripes and superconducting stripes, due to the Andreev reflection and particle-hole mixing involved in the formation of Landau levels in the latter case. Therefore, it would be of interest to study modulated superconductivity within a framework that allows the magnetic field to be varied continuously in order to more directly connect to the quantum oscillation experiments on the cuprates. Possible approaches would be to use random vortex lattices, as is done by Chen and Lee (Chen and Lee, 2009), or to develop a semiclassical approximation that allows magnetic unit cells of arbitrary aspect ratios. The latter method is the subject of the next chapter.

Quantum Oscillations in a π-striped Superconductor

4.1 Introduction

In chapter 3, we examined the mixed state of a π-striped superconductor where a spatially periodic d-wave pairing interaction led to a reconstructed FS. We found that Landau levels (LLs) are formed in the low-energy DOS for a broad range of values of the pairing interaction. In particular, we found LLs for intermediate values of the pairing potential where the spectral function exhibits Fermi arcs. Furthermore, we showed that the cyclotron effective mass for this model, defined based on the LL spacing, is equal to the specific heat effective mass. This indicates that a π-striped phase does not lead to too large a specific heat to explain the data. Riggs *et al.* (2011) argued that models based on FS reconstruction give a too large specific heat too, so it is interesting to note that does not seem to be the case for the π-striped model. Therefore, with the exception of the $\sqrt{H}$ of the background specific

heat, we demonstrated that the properties of the π-striped superconductor that we calculated are consistent with those of cuprates. However, our study in chapter 3 was limited to only a few discrete values of magnetic field which did not allow the calculation of quantum oscillations.

In this chapter[1], we overcome the limitations of the previous chapter by employing a semiclassical approximation that enables us to make more quantitative comparison with experiments. The remainder of this chapter is organized as follows. In Sec. 4.2, we introduce the approximate semiclassical numerical method used to calculate quantum oscillations. In Sec. 4.3, we discuss the differences of a uniform and modulated d-wave under this approximation. Section 4.4 shows the result of this semiclassical method for small values of the pairing interaction. In this section, we also discuss the semiclassical picture of Pippard for motion of electrons in a magnetic field in the presence of a one-dimensional periodic potential, based on linked orbits in position space, and generalize this picture to the case of a periodic pairing potential. In Sec. 4.5, results are shown for intermediate values of the pairing interaction where the shape of the spectral function resembles Fermi arcs. Section 4.6 shows how quantum oscillations in the specific heat behave for this model. Finally, the plausibility and implications of such a superconducting π-striped model are discussed in Sec. 4.7.

[1]The results presented in this chapter are published in Physical Review B (Zelli *et al.*, 2012)

4.2 Semiclassical theory in a field: BdG without vortices

In chapter 3, a magnetic field was introduced into the model using the Franz-Tesanovic singular gauge transformation,(Vafek *et al.*, 2001; Franz and Tešanović, 2000) and the resulting Boboliubov-deGennes (BdG) equations were solved numerically. As explained in appendix B, vortices, commensurate with the super-lattice, are incorporated into the magnetic unit cell. As a result, the magnetic unit cells have comparable width and length, which means that the area of a magnetic unit cell changes significantly when going from one unit cell size to next available one. Consequently, the magnetic field can only be changed in very large steps which makes it impossible to measure the area associated with quantum oscillations. In addition, we observed that commensuration effects, due to the assumed perfect order of the vortex lattice, resulted in periodic oscillations of the DOS at $E = 0$ as a function of $1/\sqrt{B}$. This behavior is not consistent with the QO observed in the cuprates where the oscillations are periodic as a function of $1/B$. The mixed state of the cuprates is most likely characterized by vortex liquid behavior where vortices do not adopt the assumed ordering in chapter 3. So the commensurability effect is irrelevant to the cuprates.

In this chapter, we use a different approach. For simplicity, consider the $\Delta = 0$ case which describes two-dimensional electrons on a square lattice, hopping from one site to its nearest neighbors. To apply a magnetic field to the system, one introduces magnetic unit cells in a given gauge with no vortices present. Independent of the choice of the gauge, the phase of the hopping term in the kinetic part of the Hamiltonian changes by 2π in going

around a magnetic unit cell. In this case, different choices of the magnetic unit cell aspect ratio result in the same DOS spectrum for a given magnetic field, provided the magnetic unit cells have the same number of sites. This means that a unit cell which is a single row of sites is equally acceptable as a square unit cell. Note that a row unit cell is only possible when using Landau gauge which has translational symmetry in one direction. The benefit of using a row unit cell is that one can add only one site to a unit cell to proceed to the next available unit cell size. Bearing in mind that magnetic field is inversely proportional to the area of magnetic unit cell, the fractional decrease in the field for adding one site is $-1/L$ for a row of length L. The magnetic field increments are much larger if one maintains a square aspect ratio. Thus a magnetic unit cell formed by a single line of sites allows the smallest field changes. For the rest of this thesis, we use L to refer to the number of sites in a unit cell so that $L = 256$ could correspond to a row unit cell of length 256 or a square unit cell with a linear size $l = 16$.

In a superconductor, one can not go to the row limit for a magnetic unit cell because of the supercurrent field associated with vortices introduces a two-dimensional space-dependent term in the Hamiltonian. However, if one assumes that the effect of the interactions of quaisparticles with vortices is negligible, then row unit cells can be used. This allows us to change the magnetic field in much smaller increments and eliminates commensuration effects. This approximation can potentially enable us to calculate the area associated with quantum oscillations. We will refer to this approximation as the semiclassical approximation or the no-vortices approach. The important question of the validity of this approximation will be addressed later in this chapter.

In order to formulate this approximation more explicitly, we start from the BdG Hamiltonian in a magnetic field.

$$H = \begin{pmatrix} -t\sum_{\delta} e^{-iA_{\delta}(r)}\hat{s}_{\delta} - \mu & \sum_{\delta}\Delta_{\delta}e^{i\phi(r)/2}\hat{s}_{\delta}e^{i\phi(r)/2} \\ \sum_{\delta}\Delta_{\delta}e^{-i\phi(r)/2}\hat{s}_{\delta}e^{-i\phi(r)/2} & t\sum_{\delta}e^{iA_{\delta}(r)}\hat{s}_{\delta} + \mu \end{pmatrix} \qquad (4.1)$$

where $\hat{s}_{\delta}$ is defined as the operator, $\hat{s}_{\delta}u(r) = u(r+\delta)$. For a model of a π-striped superconductor, the space dependent pairing interaction is $\Delta_{\delta} = \Delta\cos(q_x(x-1/2\pm1/2))$ if $\delta = \pm\hat{x}$ and $\Delta_{\delta} = -\Delta\cos(q_x(x-1/2))$ if $\delta = \pm\hat{y}$. Also $A_{\delta}(r) = \frac{e}{\hbar c}\int_r^{r+\delta}A(r)dr$ where $A(r)$ is the vector potential associated with the magnetic field. The phase of the order parameter associated with a bond between two sites is approximated by $\phi_{\delta}(r) = \frac{1}{2}(\phi(r)+\phi(r+\delta))$ where $\phi(r)$ is the phase of the order parameter on site r.

To eliminate the phase of the order parameter, we apply the following singular gauge transformation

$$U = \begin{pmatrix} e^{i\phi(r)} & 0 \\ 0 & 1 \end{pmatrix} \qquad (4.2)$$

which is a single-valued transformation (Anderson, 1998). This yields

$$H = \begin{pmatrix} -t\sum_{\delta}e^{-i(A_{\delta}(r)-\nabla\phi_{\delta}(r))}\hat{s}_{\delta} - \mu & \sum_{\delta}\Delta_{\delta}e^{i\nabla\phi_{\delta}(r)/2}\hat{s}_{\delta} \\ \sum_{\delta}\Delta_{\delta}e^{i\nabla\phi_{\delta}(r)/2}\hat{s}_{\delta} & t\sum_{\delta}e^{iA_{\delta}(r)}\hat{s}_{\delta} + \mu \end{pmatrix} \qquad (4.3)$$

where $\nabla\phi_{\delta}(r) = \phi(r+\delta)-\phi(r)$. Now using the definition of the superfluid

velocity, we can write the Hamiltonian as follows

$$
\begin{pmatrix}
-t \sum_\delta e^{i(A_\delta(r)+2v_s^\delta(r))} \hat{s}_\delta - \mu & \sum_\delta \Delta_\delta e^{i(A_\delta(r)+v_s^\delta(r))} \hat{s}_\delta \\
\sum_\delta \Delta_\delta e^{i(A_\delta(r)+v_s^\delta(r))} \hat{s}_\delta & t \sum_\delta e^{iA_\delta(r)} \hat{s}_\delta + \mu
\end{pmatrix}
\tag{4.4}
$$

where $mv_s^\delta(r) = \hbar\nabla\phi_\delta(r)/2 - (e/c)A_\delta(r)$. If the effect of vortices is negligible, one can approximate 4.4 by setting $v_s^\delta(r) = 0$.

Before proceeding further, we compare the results of this approximation to that of the full BdG equations with vortices to check whether the approximation works. It is found that the two cases (with and without vortices) are in qualitative agreement for both small and intermediate Δ. For small Δ, the qualitative agreement is illustrated in Fig. 4.1 for the low-energy DOS for $\Delta = 0.02$ and $\mu = -0.23$ in the presence of a magnetic field of $L = 256$. For intermediate Δ, the comparison is shown in Fig. 4.2 for $L = 1024$, $\Delta = 0.25$ and $\mu = -0.3$ corresponding to 1/8 doping. Note that, in this figure, the nonzero DOS at $E = 0$ for the case with vortices is a commensurability effect which is absent for the case without vortices.
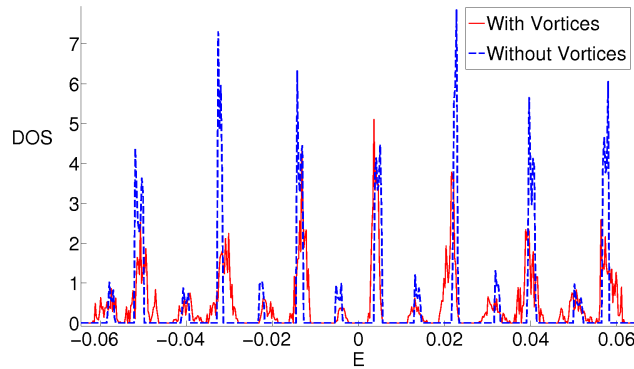
Figure 4.1 Comparison of the low-energy DOS of a π-striped superconductor with $\Delta = 0.02$ and $\mu = -0.23$ in the presence of a magnetic field of $L = 256$ with and without vortices, as described in the text.
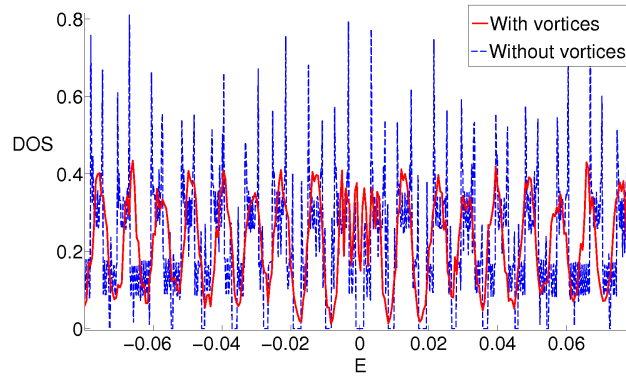
Figure 4.2 Comparison of the low-energy DOS of a π-striped superconductor in the presence of a magnetic field of $L = 1024$ with $\Delta = 0.25$ and $\mu = -0.3$ corresponding to 1/8 doping with and without vortices.

Here some details for the calculation of the DOS in figures 4.1 and 4.2 are provided (also see Appendix A). The length of a row unit cell, which is spanned in the x direction, is given by $L = 8m$ where m is an integer. The magnetic field associated with a unit cell L lattice constants long is $B = \phi_0/La^2$ where a is the lattice spacing. The number of unit cells in the x direction can be taken to be only one because adding more unit cells in the x direction results in the same DOS spectrum. This point is discussed in the next section. However, the number of unit cells in the y direction, N, must be large to give a well-defined DOS. Using Bloch's theorem, one needs to diagonalize N BdG matrices with linear size $2L$ so that the total number of positive-energy states is NL.

4.3 Comparison to Uniform d-wave

In late 90s and early on in this new century, the nature of the electronic states of a d-wave superconductor in the presence of a perpendicular magnetic field was a controversial subject in theoretical condensed matter physics. First, it

was suggested by Gor'kov and Schrieffer (Gor'kov and Schrieffer, 1998) and by Anderson (Anderson, 1998) that the spectrum in a magnetic field consisted of Landau levels with energies $\pm\hbar\omega_H\sqrt{n}$ where n is a positive integer and $\omega_H = \sqrt{2\omega_c\Delta/\hbar}$, ω_c is the cyclotron frequency, and Δ is the maximum gap (Marinelli *et al.*, 2000). This is essentially the result for an anisotropic Dirac cone. A key step in obtaining this result is to assume that the effect of the superfluid velocity due to vortices is negligible compared to the vector potential **A**. However, it was soon shown by Mel'nikov (Melnikov, 1999) that the superfluid velocity is a strong perturbation for this problem, and, not long afterward, Franz and Tesanovic (Franz and Tešanović, 2000) developed an approach which treated the superfluid velocity field and the vector potential on an equal footing. Note that the results of chapter 3 were obtained using this approach. After linearizing the Hamiltonian near the nodal points, Vafek et al (Vafek *et al.*, 2001) give an elegant expression for the continuum Hamiltonian near a single node in the FT gauge.

$$H_N = v_F(p_x + a_x)\tau_3 + v_\Delta(p_y + a_y)\tau_1 + mv_Fv_{sx}, \tag{4.5}$$

where τ_i are Pauli matrices, $2\mathbf{a} = m(\mathbf{v}_s^e - \mathbf{v}_s^h)$, and $2\mathbf{v}_s = \mathbf{v}_s^e + \mathbf{v}_s^h$. This expression shows that the difference of the superfluid velocities associated with the vortices on the two sublattices in the FT gauge, the so-called Berry gauge field, acts like a vector potential and appears coupled to the momenta of the Dirac quasiparticles, while the superfluid velocity enters as a scalar potential. This symmetry of the Hamiltonian results in the spectrum of d-wave quasiparticles in a magnetic field remaining gapless. Based on this result, the authors claimed that there are no LLs in the low-energy DOS of a d-wave superconductor in

the presence of a magnetic field.

Note that there are two ways that one can set the superfluid velocity to zero in the exact BdG equation. If one gets rid of v_{sx} in Eq. (4.5), one does not get the Dirac-like LLs described earlier in this section. In Eq. (4.4), the superfluid velocity only appears in one of the diagonal parts, whereas one can write the superfluid velocity in both diagonal parts of the BdG Hamiltonian as follows:

$$H = \begin{pmatrix} -t \sum_\delta e^{i(\nabla\phi(r)/2 + v_s(r))} \hat{s}_\delta - \mu & \sum_\delta \Delta_\delta e^{i\nabla\phi(r)/2} \hat{s}_\delta \\ \sum_\delta \Delta_\delta e^{i\nabla\phi(r)/2} \hat{s}_\delta & t \sum_\delta e^{i(\nabla\phi(r)/2 - v_s(r))} \hat{s}_\delta + \mu \end{pmatrix}. \quad (4.6)$$

Setting $v_s = 0$ in Eq. (4.6) would leave us a system in the absence of a magnetic field that experiences half-flux scatterings due to the $\nabla\phi(r)/2$ term. Such a system would never be a good approximation to the real system. However, setting $v_s = 0$ in Eq. (4.4) may be a good approximation provided some conditions are satisfied. To make our point clearer, let us start with the $\Delta = 0$ limit in which the DOS spectrum consists of sharp LLs in the presence of a magnetic field (everywhere except near the van-Hove singularity as seen in Fig. A.1). Setting $v_s = 0$ in Eq. (4.6) leads to a DOS spectrum that has no resemblance to the exact DOS solution. However, setting $v_s = 0$ for the $\Delta = 0$ limit in Eq. (4.4) is exact and results in sharp LLs. Henceforth in this thesis, when we use the term "ignoring vortices", we mean setting the superfluid velocity in Eq. (4.4) to zero. Once Δ becomes finite, then ignoring vortices is not exact but an approximation. It is the purpose of this section to justify this approximation in more detail.

Previous studies have already shown that ignoring vortices is not a good

63
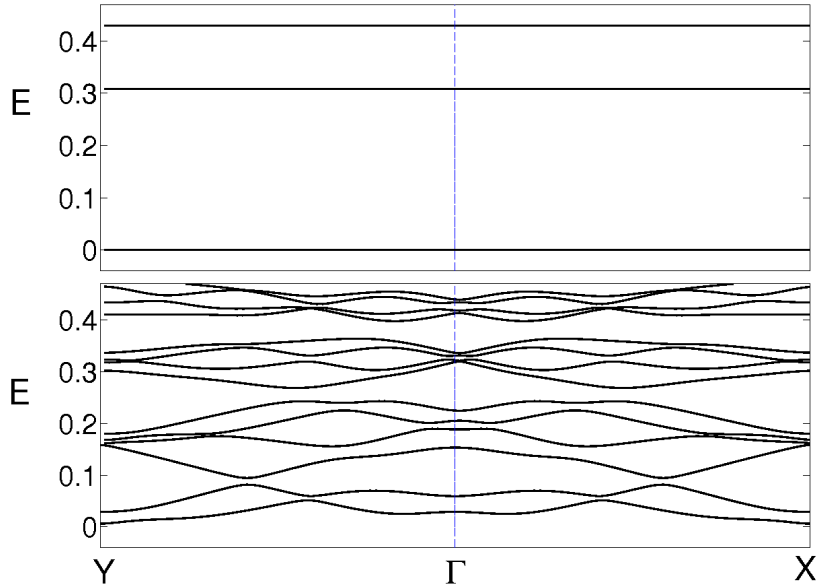
Figure 4.3 Low-lying energy levels (in units of t) of a uniform d-wave with $\Delta = 0.25$, $\mu = -0.3$, and $L = 256$ plotted versus wave vector along two directions in the BZ (see Fig. 4 in (Vafek *et al.*, 2001)). In the top panel, the effects of vortices are ignored. However, the bottom panel includes the effects of vortices. All calculations were obtained by diagonalizing the BdG Hamiltonian in the FT gauge.

approximation for a uniform d-wave superconductor. We have investigated the properties of a uniform d-wave superconductor in a magnetic field in such detail in order to emphasize the *differences* between that problem and a π-striped superconductor. The semiclassical result for uniform d-wave, when neglecting v_s, results in perfectly flat bands, at energies scaling approximately as $\pm E_1 \sqrt{n}$ for $n = 0, 1, 2, \ldots$. This is shown in Fig. 4.3a for a uniform d-wave gap of $\Delta = 0.25$, without vortices and with $\mu = -.3$ and $L = 256$, along the directions $Y \to \Gamma \to X$ in the magnetic BZ (see Fig. 4 in (Vafek *et al.*, 2001)). For these parameters, $E_1 \approx 0.31$. In contrast, Fig. 4.3b shows the band structure for the same parameters when including the effect of vortices. One might expect that the effect of vortices is only to broaden the flat bands which would result

in broadened Landau levels. However, there is no hint of broadened Landau levels in Fig. 4.3b. In fact, the two plots in Fig. 4.3 bear no resemblance to each other, confirming that v_s is indeed a strong perturbation for uniform d-wave.
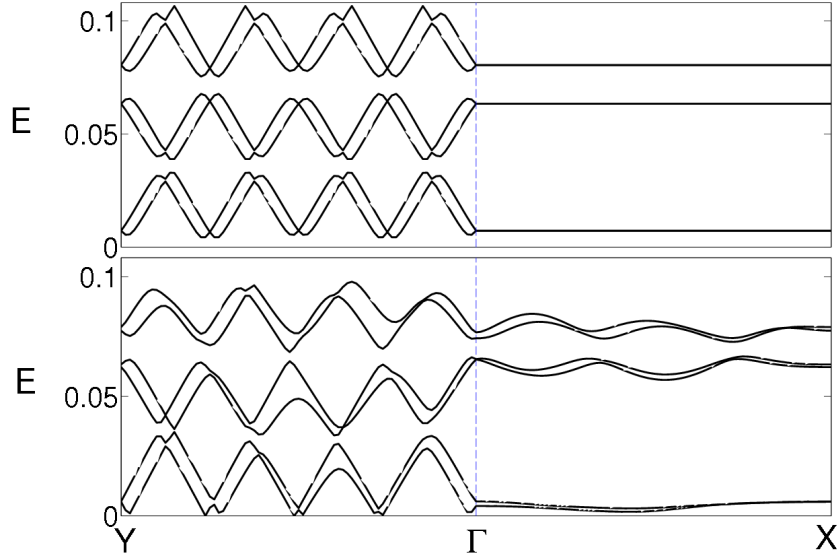
Figure 4.4 Low-lying energy levels (in units of t) for, from top to bottom, modulated d-wave ignoring the effects of vortices and modulated d-wave including the effects of vortices for $\Delta = 0.25$, $\mu = -0.3$, and $L = 256$.

In Fig. 4.4, we have calculated the band structure of the excitations for the system of π-striped superconductor with and without vortices for the case $\Delta = 0.25$ and $\mu = -0.3$, for a magnetic field corresponding to $L = 256$. For the semiclassical approximation, Fig. 4.4a, the bands are flat along $\Gamma \to X$ which corresponds to moving in the reduced BZ along constant $k_y = 0f$. Dispersion arises along the Y direction, resulting in one-dimensional DOS peaks. To understand the dispersion along k_y and the flat bands for constant k_y for $v_s = 0$, we refer to the continuum picture where, in Landau gauge, the wave functions are plane waves of wavevector k_y along y and localized in x around a

position $x_0 \sim k_y$ (see Eq. (A.5)). In the presence of a spatially varying poten-
tial and a perpendicular magnetic field, electrons move along equipotentials.
For a potential modulated along x, this motion is along y, at a position and
energy that depend on k_y. This provides an interpretation of the meaning of
"broadened Landau levels." The broadening is due to the different ways that a
Landau level wave function averages over the periodic (pairing) potential, de-
pending on its position with respect to the modulation. Comparing Figs. 4.4a
(without vortices) and 4.4b (with vortices), we see that band structure is rel-
atively insensitive to the effect of vortices for these parameters. Nevertheless
it is clear that the broadened Landau levels are further broadened and shifted
by the vortices.
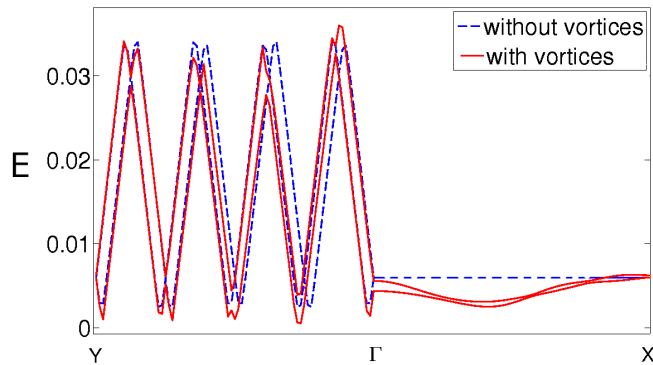
Figure 4.5 Comparison of the first two bands for the BdG Hamiltonian of
a π-striped superconductor with $\Delta = 0.2$ and $\mu = -0.3$ in the presence of a
magnetic field of $L = 256$ to those of obtained using no-vortices approximation.
The overall agreement is good and, in fact, it is excellent near the Y point.

To have a even better comparison of the exact and approximate method,
we have shown the first two band structures of the two cases for another pairing
potential, $\Delta = 0.2$, in Fig. 4.5 . One can see that the overall agreement of the
two cases is good. Furthermore, t is also useful to compare the band structures
of the two cases (with and without vortices) for small values of Δ. We have

already shown that numerical calculations, with and without vortices, result in similar low-energy DOS as seen in Fig. 4.1 for $\Delta = 0.02$ and $L = 256$ at 1/8 doping. The energy bands, shown for positive energy along $Y \to \Gamma \to X$ in Fig. 4.6, look similar for the cases with and without vortices and both are similar to the Landau level structure observed for $\Delta = 0$. Note that the bands for both cases, with and without vortices, shift in the same direction from the $\Delta = 0$ Landau level energies.
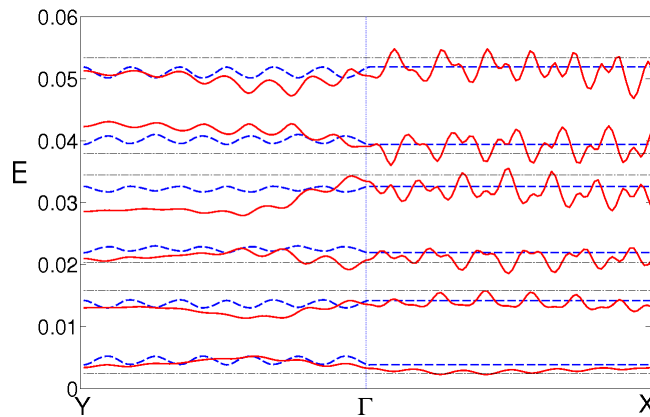
Figure 4.6 Comparison of the low-energy bands for the BdG Hamiltonian of a π-striped superconductor with $\Delta = 0.02$ and $\mu = -0.23$ in the presence of a magnetic field of $L = 256$. The solid curves are the bands for the full BdG Hamiltonian, including vortices. The dashed curves are the semiclassical results for no vortices, and the flat lines (dash-dot lines) are the Landau levels in the limit $\Delta = 0$.

So why does this approximation work for a modulated d-wave but not a uniform d-wave superconductor? The main difference is that the π-striped superconductor in zero field does not have nodal points at E_F with Dirac-like excitations. Instead it has extended regions of Fermi surface which persist in the presence of an off-diagonal potential that couples electron states at $\mathbf{k}$ and hole states at $-\mathbf{k} \pm \mathbf{q}$ and which gaps only parts of the Fermi surface. We find that, for not very large gap amplitudes, the u's and the v's, the Bogoliubov

quasiparticle amplitudes, jump sharply on crossing the FS (see figures 2.5, 2.6 and 2.7), as they do for a normal metal, rather than varying smoothly as they do away from Dirac point. These features of the π-striped superconductor lead to very different behavior in a magnetic field from that of a uniform d-wave superconductor. Since quantum oscillations arise from the presence of broadened Landau levels in the semiclassical approximation, we conjecture that this approximation is valid in parameter ranges where the exact calculation also exhibits Landau levels. Conversely, if broadened Landau levels are not present in the full BdG calculation, then the semiclassical approximation is not applicable. This is the case for large values of Δ where no LLs are observed in exact BdG calculations as discussed in Sec. 3.2. As shown in Fig. 2.8, the parts of the FS where the pairing interaction is vanishingly small shrink for large Δ. So we expect the semiclassical approximation to be unreliable in this range.

4.4   Results for Small Δ

For small values of Δ, the effect of the pairing interaction is to induce small gaps in the closed $\Delta = 0$ FS as shown in Fig. 2.4a. Looking at Fig. 4.1, it seems that the only effect of the small pairing potential is to partially reflect each unperturbed LL to the other side of the Fermi energy. This suggests that the area associated with quantum oscillations should remain the large closed FS area for $\Delta = 0$. However, as we will see, this is not the whole story. It also happens that interference between the original FS area and another orbit induced by the potential leads to LL broadening which oscillates as a function of magnetic field. The widths of the Landau levels near the Fermi energy

affect the low temperature properties of the system and, consequently, their dependence on magnetic field is expected to be observable in experiments. In the following discussion, we focus on the LL closest to the Fermi energy and measure its width and its position relative to the Fermi energy. We refer to this LL as the first LL. Here, we define the width to be the difference between the low and high energy ends of a LL feature in the DOS spectrum (see the inset of Fig. 4.7). By choosing a large system size N in the y direction and sufficiently small energy intervals for the DOS calculation, the width of a LL can be calculated with precision.
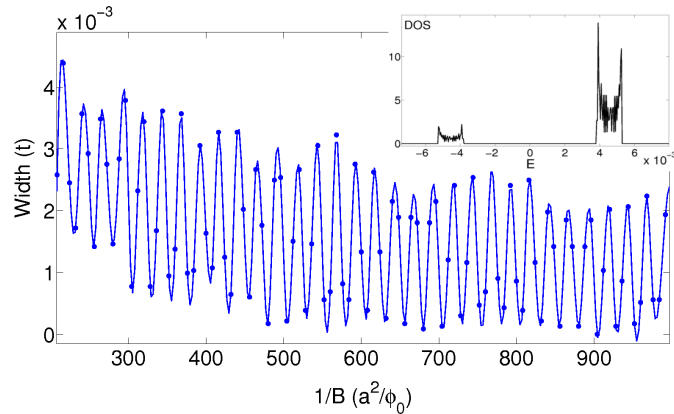
Figure 4.7 The width of the LL closest to $E = 0$ as a function of $1/B$ or L for $\Delta = 0.02$ and $\mu = -0.23$, corresponding to 1/8 doping within the semiclassical (no-vortices) approximation. $1/B$ is written in terms of the lattice constant, a, and flux quantum, ϕ_0. The solid line is a spline fit to the data that shows the oscillatory behavior more clearly. The inset shows the first LL for $L = 256$.

The width of the first LL as a function of $1/B$ is shown in Fig. 4.7 for $\Delta = 0.02$ and $\mu = -0.23$, corresponding to 1/8 doping. The width shows an oscillatory behavior. To calculate the area associated with the oscillations, we perform a Fourier transform analysis. Note that the Fourier transform analysis is performed to determine the dominant frequencies in oscillations in the width and uses the data but not the spline fit (see Fig. 4.7). To have a reasonably
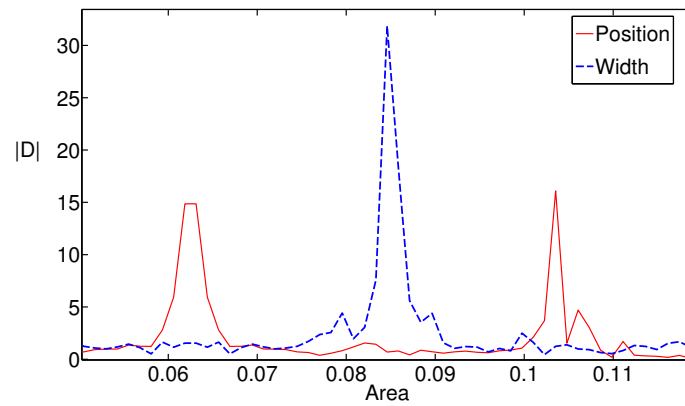
Figure 4.8 Power spectrum associated with the oscillations of the width (as shown in Fig. 4.7 and position of the first LL for $\Delta = 0.02$ at 1/8 doping. The x axis is rescaled so that it corresponds to area in units of the area of BZ.
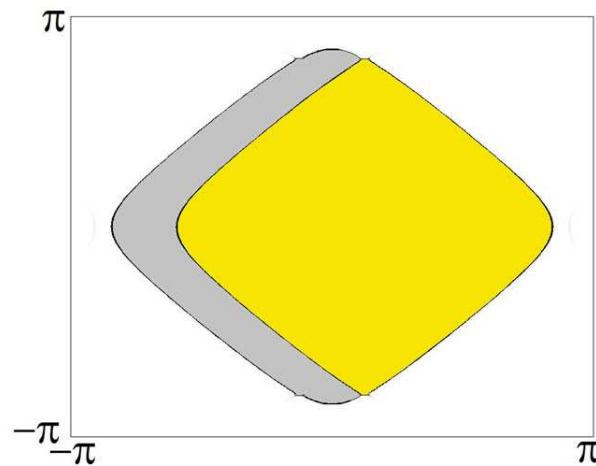
Figure 4.9 The spectral function of a π-striped superconductor for $\Delta = 0.02$ at 1/8 doping. The yellow area corresponds to the area associated with the oscillations in the width and is shown in Fig. 4.10(b) separately.

accurate analysis, we choose the minimum number of input data points for the Fourier transform function to be 99, here and for the remainder of this chapter. Figure 4.8 shows the power spectrum associate with oscillations in the width of the first LL for $\Delta = 0.02$ and $\mu = -0.23$. The x axis has been rescaled to correspond to area in units of the area of the BZ. The peak in the power spectrum associated with oscillations in the width occurs at an area of about 0.0845. It turns out that by adding 2/8 to 0.0845, we get the area of the yellow region in Fig. 4.9 which is 0.3345. We refer to this yellow region as A_b which is shown in Fig. 4.10b separately. Plotting the μ dependence of the calculated area coming from the power spectrum of width, we discover that it has the same slope as the yellow area in Fig. 4.9. This is illustrated in Fig. 4.11. The two lines are the same within error bars when 2/8 is added to QO area. The reason why we are allowed to do this is that the area measured by the power spectrum is only an area modulo 1/8. Since a minimum of 8 sites is added to a magnetic unit cell in changing B, one can not directly see periods of oscillations in L that are smaller than 8. This means that we can not see areas that are large than 1/8 of the BZ. Although, in principle, any multiple of 1/8 could be added to the area, only adding 2/8 results in an identified area or orbit for the FS at this doping and pairing strength. This analysis shows that the QO area is, in fact, the yellow area in Fig. 4.9. One other way to prove this is to start with a large chemical potential for which the FS areas are less than 1/8. By continuously decreasing the absolute value of μ, the FS area associated with the width oscillations becomes larger and reaches 1/8 for some chemical potential. By even more decreasing μ, we find that the corresponding Fourier transform peak for this bigger than 1/8 FS is only the area modulo 1/8.
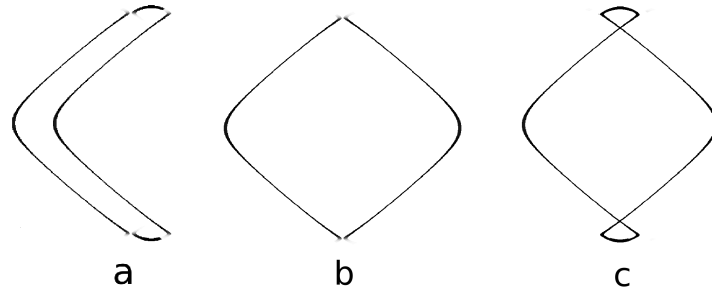
Figure 4.10 (a) Boomerang-shaped FS orbit involving two Andreev-Bragg scatterings and two tunnellings, as shown schematically in Fig. 4.13b, but for a period 8 modulation. The area of this orbit is denoted $A_T - A_b$ in the text, where A_T is the area of the unperturbed FS (b) The corresponding area A_b. (c) The area $2A_b - A_T$, corresponding to the difference of figures (a) and (b).
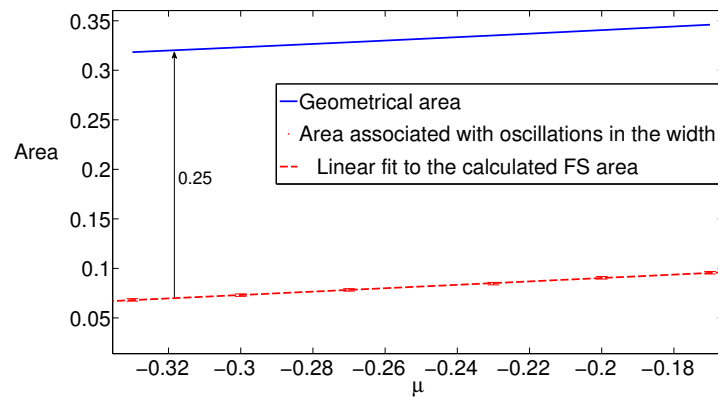
Figure 4.11 Comparison of the geometrical area, A_b, and the area associated with quantum oscillations in the width of the first LL for $\Delta = 0.02$ vs μ in the region around 1/8 doping. Adding 2/8 to the calculated FS area, as discussed in the text, gives the yellow area in Fig. 4.9.

Next we consider oscillations in the position of the first LL. Since, the shape of a LL is not symmetric around its position, we define the position of a LL to be the energy at which there are equal numbers of states on both sides. Interestingly, there are two peaks that appear in the power spectrum of the position as shown in Fig. 4.8. The peak on the left corresponds to the large $\Delta = 0$ FS area, A_T, as expected. As before, we can only measure the area modulo 1/8. For the large FS, one must add 3/8 to the measured value to obtain an area that corresponds to an allowed FS orbit. The relevant peak in Fig. 4.8 occurs at 0.0625 which gives $0.0625 + 3/8 = 0.4375$ for the area of the original FS. Note that, as expected for 1/8 doping, this corresponds to a density of $0.4375 * 2 = 7/8$ electrons per site where the factor of 2 accounts for the spin degree of freedom. The other peak of the power spectrum of position oscillations is associated with the shaded area in Fig. 4.9 that looks like a boomerang. One expects this peak to occur at $0.4375 - 0.3345 = 0.103$ in agreement with the position of the right hand peak in Fig. 4.8. The relationship is also confirmed in Fig. 4.12 where the position in the power spectrum and the boomerang-shaped geometrical value are compared as μ is varied.

4.4.1 Pippard's Semiclassical Picture

So far in this section, we have calculated the areas associated with the oscillations in the width and position of the first LL of a π-striped superconductor in a magnetic field for small Δ. The question arises whether a simple explanation for the observed areas exists. Here we develop a simple picture of the semiclassical motion of particles which provides an explanation for the quantum oscillation areas. This picture is based on Pippard's semiclassical motion
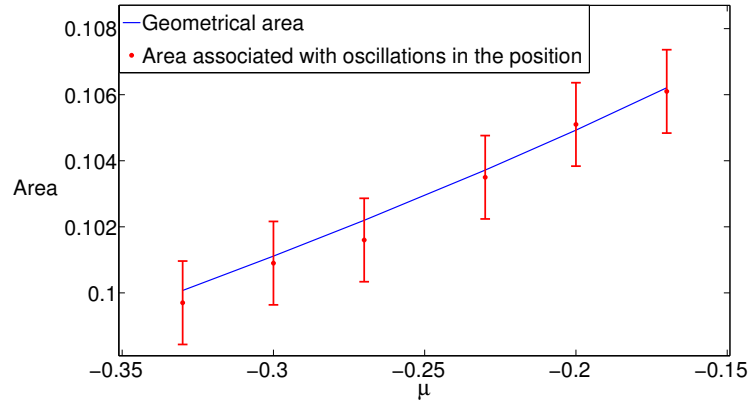
Figure 4.12 Comparison of the geometrical area, $A_T - A_b$, the boomerang-shaped area in Fig. 4.10a, and the area associated with oscillations in the position of the first LL, corresponding to the highest frequency peak in Fig. 4.8, shown as a function of μ.

of electrons in the presence of a magnetic field and weak periodic potential. When no periodic potential exists, free electrons precess in circular orbits in an applied magnetic field both in position and in k space. For free electrons, the trajectory in k space has the same form as the trajectory in real space, rotated by $\pi/2$. Discrete, sharp LLs are formed because the Aharonov-Bohm (AB) phase gained by going around the orbit in position space needs to be a multiple integral of 2π. If a weak periodic potential is turned on, small gaps open in the original orbits and the orbits become linked as shown in Fig. 4.13a. Due to the periodic potential, an electron can now Bragg scatter from one orbit to another. It can scatter twice and as a results follow an electron pocket as the shaded region A_b in Fig. 4.13a. The particle can also follow the original circular orbit by tunneling through the gaps. The LLs are broadened due to the periodic potential. However, interference of the particles moving on different trajectories determines the magnitude of the broadening. The shaded area in Fig. 4.13a is $(\frac{\hbar c}{eH})^2 A_b$ corresponding to an electron pocket where, in Pippard's

notation, A_b is the corresponding area in k space. We also refer to the k space area of the original orbit as A_T which means that the corresponding area in position space is $(\frac{\hbar c}{eH})^2 A_T$.
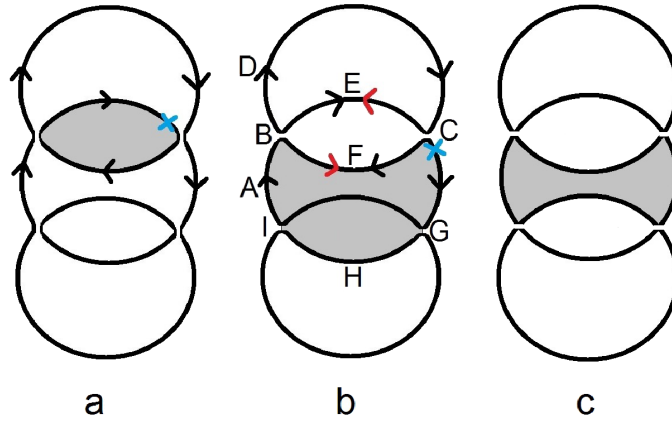
Figure 4.13 Semiclassical motion of a nearly free particle system in the presence of a weak periodic potential (a) and a weak periodic superconducting pairing potential, (b and c). The direction of the semiclassical motion for particles is shown by black arrows. Holes (shown by red arrows) precess in the opposite direction. The gray area in the center figure is $(\frac{\hbar c}{eH})^2 (A_T - A_b)$ where A_b is the area of the small electron pocket in panel a and A_T is the area of the original circular FS. Starting from the blue cross in panel b, the particle can either go over the whole unperturbed circular orbit by tunnelling at points B,C,G, and I, or tunnel only at points G and I and Andreev scatter twice at points B and C covering the gray area. Another possible path is to Andreev scatter at points H and I and tunnel at points B and C. However, this path covers the same gray area. The change in the phase of the wave function is $\frac{\hbar c A_T}{eH}$ when the particle goes over the whole circular circuit and $\frac{\hbar c (A_T - A_b)}{eH} + \beta$ when it travels around the shaded area, where β is the phase shift due to two consecutive Andreev scatterings and is assumed to be relatively field independent. This behavior should be contrasted to that of the linked orbit of Pippard, shown on the left, where the particles orbit around the areas A_T and A_b. Thus, as discussed in the text, the areas associated with quantum oscillations in the width of the first LL are different for the periodic potential and the periodic pairing models. Panel c shows the closed orbit corresponding to four successive Andreev-Bragg scatterings.

Now we consider what happens for a weak periodic superconducting pairing potential, for which Bragg scattering in Pippard's picture is replaced

by Andreev scattering. In this case, the possible orbits are shown in Fig. 4.13b. For the case of a weak pairing potential and a strong magnetic field, it is most likely for particles (here either electrons or holes) to tunnel through gaps at points B, C, G, and I, following the original cyclotron orbit. For the simplest process involving the periodic pairing potential, a particle could start at the blue X below point C, tunnel at points G and I through section H, and Andreev scatter into a hole at point B, pass point F and Andreev scatter back into a particle at point C. In the first case, the increment in the AB phase of the wave function is $\frac{\hbar c A_T}{eH}$, corresponding to the original FS area. In the second case it is $\frac{\hbar c (A_T - A_b)}{eH} + \beta$, where β is a phase shift due to two consecutive Andreev scatterings and is assumed to be relatively field independent. Note that this path, apart from the original orbit, is the most probable closed path because, for small Δ which only induces very small gaps in the FS, the probability of tunneling is larger than the that of Andreev scattering. Also it is equally likely for the particle to Andreev scatter at points G and I and tunnel at points B and C, and this path covers the same shaded area as in the second case. The probability of undergoing 4 consecutive Andreev reflections (at points B, C, G, and I), corresponding to an area $A_T - 2A_b$ and shown in panel c, is small for small Δ. It should be noted that, when an electron Andreev scatters, it keeps precessing as a hole in the opposite direction to electrons as shown in Fig. 4.13b.

So far the picture seems to be a plausible picture. Now the question is how this picture justifies the area associated with oscillations in the width of the first LL. For a fixed chemical potential, A_T and A_b are fixed. The phase of the wave function due to different trajectories changes as H is varied. The relative change of the phase due to the two trajectories described above is

$\delta\phi = \frac{\hbar A_b}{eH} - \beta$. The broadening of a LL will be minimal when $\delta\phi$ is an integral multiple of 2π. The frequency of this occurring and so the broadening of the LL should then be proportional to A_b as the magnetic field varies. In fact, this is equivalent to the yellow area in Fig. 4.9. Note that our semiclassical argument here is not dependent on the symmetry of the order parameter. In fact, we performed the same calculations as in the previous section for an oscillating s-wave order parameter. Interestingly, it was found that the frequency of the broadening of the first LL corresponds to the same area as for a π-striped d-wave superconductor.

The same argument can be applied to the case of the periodic potential in Fig. 4.13a. In this case, it is the interference between the phase shift around the shaded pocket and that of the original circular orbit that leads to broadening of Landau levels. As H is varied, the relative phase changes as $\delta\phi = \frac{\hbar c(A_T - A_b)}{eH} - \beta'$ where β' is the phase shift due to two consecutive Bragg scatterings. Performing the numerical calculations for a model in the normal state with a period 8 site potential, we confirm that $A_T - A_b$ is the area associated with the oscillations in the width of the first LL.

Once again, this is not the whole story. Based on the simple semiclassical picture provided we can also look for oscillations in the position spectrum due to the orbit shown in Fig. 4.13c, involving four Andreev-Bragg scatterings, which is shown for the period 8 system in Fig. 4.10c. This feature is expected to be weak for $\Delta = 0.02$ and to occur at $2A_b - A_T = 0.2315$. Subtracting $1/8$, we expect a small peak in the position spectrum at 0.1065, which is barely visible in Fig. 4.8. In order to check whether this feature is real or just an artifact, we vary the value of Δ. The results are shown in Fig. 4.14 for $\Delta = 0.01$, 0.02, and 0.03. As expected, the magnetic breakdown peak at 0.0625 drops
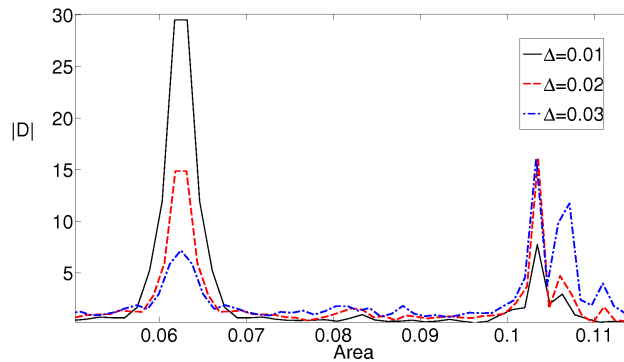
Figure 4.14 Power spectrum for oscillations of the position of the lowest LL for small values of the pairing potential amplitude, Δ. As discussed in the text, the peak at 0.0625 corresponds to the area A_T, the original FS. The peak at 0.103 corresponds to $A_T - A_b$, the boomerang-shaped area shown in Fig. 4.10a, while the feature at 0.1065 corresponds to the orbit with area $2A_b - A_T$, shown in Fig. 4.10c.

rapidly with increasing Δ while the "boomerang" peak at 0.103 grows and the peak at 0.1065, due to the closed orbit of Fig. 4.10c, grows more rapidly. The consistency of the numerical calculations with the semiclassical pictures we provided for both cases, periodic potential and periodic pairing potential, indicates that our simple picture for semiclassical motion of particles is valid. Strictly speaking, it is valid for the no-vortex approximation. However, the agreement between the vortex and no vortex results presented earlier leads us to conjecture that this simple picture captures the main features, even in the presence of supercurrents.

4.4.2 μ Dependence

In this subsection, we examine the approximation of neglecting vortices in more detail. In particular, we would like to see whether the same kind of quantum oscillations observed so far in this section occur when vortices are included in the calculation. Obviously, we can not change the magnetic field in small
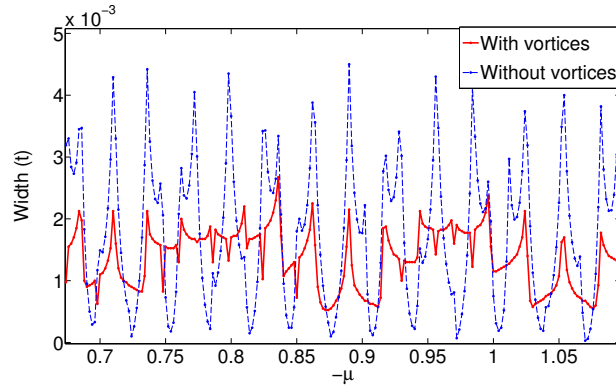
Figure 4.15 The width of the LL closest to $E = 0$ versus μ for a constant magnetic field of $L = 256$. The period of the oscillations for the case without vortices (the dotted lines) corresponds to a change in the area of Fig. 4.10b by one LL area. The same function for the case with vortices (solid line) shows rather similar behavior.

steps if vortices are present, but μ can be varied continuously. If the same behavior as a function of μ is seen for the two cases, then the same behavior as a function of $1/B$ is also expected. Fig. 4.15 shows the width of the first LL versus μ at a constant magnetic field of $L = 256$ in the absence and presence of vortices. Note that $L = 256$ corresponds to a linear size of $l = 16$ for a square unit cell when the FT transformation is used. The apparent oscillatory behavior of the width as a function of μ, when the vortices are absent, is due to changes in the area A_b by one LL area. Here a LL area is $1/L$ of the area of the BZ. The same plot for the case with vortices shows some similarity, but the similarity is more apparent when the Fourier transform of the plot is taken. Note that, in order to have a meaningful Fourier transform, the period of oscillations as a function of μ needs to be fairly constant as μ varies. Since the FS area changes rapidly as a function of μ around 1/8 doping, we have chosen to study larger negative values of μ where the FS area changes more smoothly.
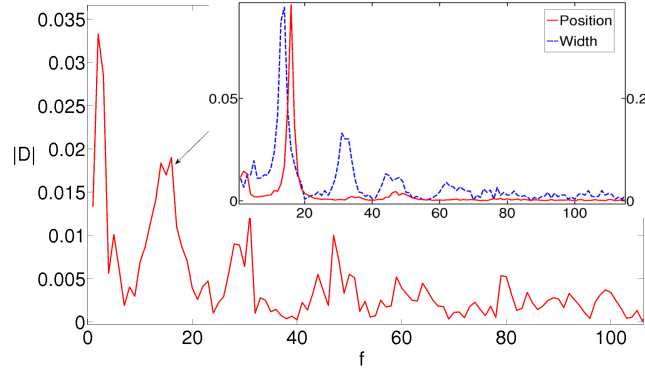
Figure 4.16 Power spectrum associated with the behavior of the width as a function of μ for the case with vortices. The broad peak denoted by the arrow corresponds to a change in A_T and A_b by one LL area. Power spectra associated with the width and the position of the first level for the case without vortices are shown in the inset. The sharp peak at very low frequencies corresponds to a change by one LL area in A_b. Note that, as shown in the inset, there is a maximum at the same low frequency in the position power spectrum for the case without vortices.

The power spectrum associated with the width of the first LL as a function of μ for the case with vortices is shown in Fig. 4.16. Looking at the figure, we see that the peaks in the power spectrum coincide with those of the width and the position of the first LL in the absence of vortices which are shown in the inset. The peak denoted by the arrow is a broad peak corresponding to an oscillatory behavior associated with a change of one LL area both in A_b and A_T. Another peak that appears at very low frequencies for the case with vortices in Fig. 4.16 does not show up when vortices are absent. It appears that this peak corresponds to $A_T - A_b$. This latter area has already been seen in the power spectrum of the position of the first LL in the case without vortices. This analysis implies that, even though there are differences, the assumption of neglecting the effect of vortices appears to be a good approximation for understanding the behavior of a π-striped superconductor in a magnetic field. The fact that both cases show an oscillatory behavior in the width of the LL

closest to $E = 0$ when the area A_b of Fig.4.10b is changed by one LL area suggests that the main features of quantum oscillations that are observed for the case without vortices should persist for the case with vortices.

4.5   Intermediate to Large Δ

In this section, we consider larger values of Δ, specifically the range in which the spectral function resembles Fermi arcs (FA). It should be noted that there are gaps within the FA-shaped spectral function that play a significant role in low-energy properties of this model. We examine whether quantum oscillations exist for this range of intermediate to large Δ. As in the small Δ case, one can measure the width and the position of the peak closest to the Fermi energy. Performing the calculations for a model of only nearest neighbor hopping, the results are discussed in two subsections, at half-filling and around $\frac{1}{8}$ doping. Later on in this chapter, we include the second nearest neighbor hopping term in order to have a more realistic band structure.

Note that, even though there is qualitative agreement for intermediate Δ in the range $0.15 \leq \Delta \leq 0.35$, our approximation results in a rather different behavior from the full BdG technique with vortices for large Δ in the range $\Delta \geq 0.4$. In this range, the LLs are sharp when vortices are absent in contrast to the result of the previous chapter. This is expected because, as Δ increases, the role of vortices becomes more significant and our semiclassical approximation breaks down for some threshold value of Δ in the range $0.35 \leq \Delta \leq 0.4$. Nevertheless, we are reporting the data for large Δ to gain some insight for understanding the physical picture in the $0.15 \leq \Delta \leq 0.35$ range where qualitative agreement exists.

4.5.1 Half-filling
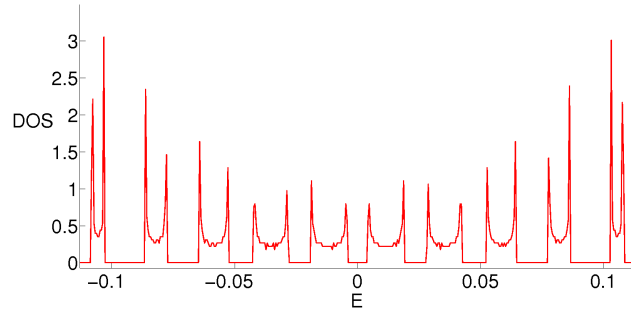
Figure 4.17 The low-energy DOS for $\Delta = 0.4$ and $L = 800$ at half-filling. Each (double) peak has twice the degeneracy of a LL.

For $\mu = 0$, the points at the centers of the Fermi arcs, which occur at $k_y = \pm\pi/2$, are gapless. In addition, for this special case of $\mu = 0$, the FS arcs for $k_y > 0$ ($k_y < 0$) are symmetric under reflection across the line $k_y = \pi/2$ or $k_y = -\pi/2$ which means that the lobes of the figure-eight FS segments have equal areas.

Fig. 4.17 shows the low-energy DOS for $\Delta = 0.4$ at half-filling in the presence of a magnetic field of $L = 800$. Each peak has twice the degeneracy of a LL and is, in fact, composed of two Landau levels that touch. Turning on the chemical potential creates a small gap at the center of the peak. This merging of pairs of Landau levels does not occur in the case with vortices, where the Landau levels are resolved even at half-filling.

Fig. 4.18 shows the width of the first peak as a function of $1/B$ for several values of Δ at half-filling. The most obvious feature of this figure is the oscillations that become more prominent for larger Δ. There is also a smooth background width which decreases for decreasing B and increasing Δ.

The behavior of Fig. 4.18 can be explained by the left and right panels of Fig. 4.19. The right hand panel, for $\Delta = 0.4$, shows a line of figure-eight-
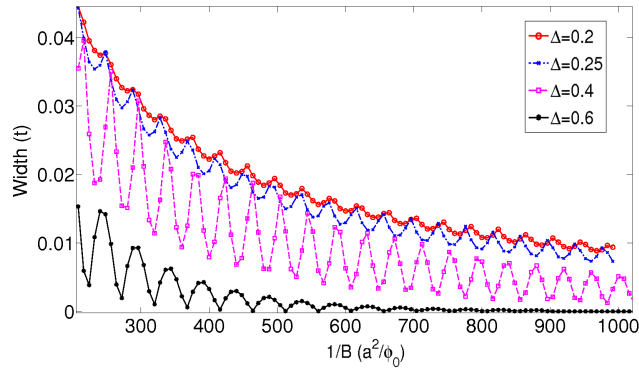
Figure 4.18 Half width of the peak closest to $E = 0$ for different values of Δ at half-filling. The Fermi surfaces for two of the Δ values in this figure are shown in Fig. 4.19.
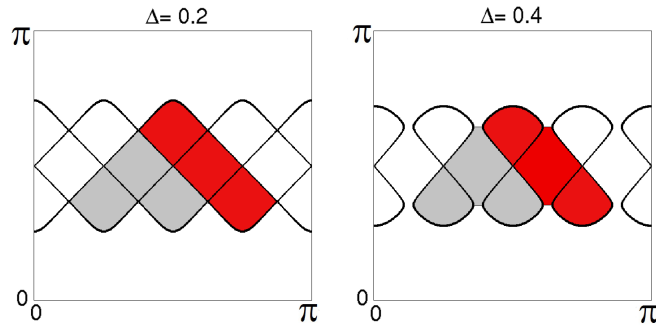
Figure 4.19 Areas consistent with the quantum oscillations seen in the width of the first peak in the low-energy DOS are shown in red (dark-shaded) for two values of Δ at half-filling. Note that, for $\mu = 0$ the gray (light-shaded) areas have the same area as the red areas.

shaped Fermi surfaces which are separated by gaps in k-space. In contrast, as shown in the left hand panel, the gaps are very small for $\Delta = 0.2$. At high fields, magnetic breakdown causes tunnelling across these gaps along the open orbits. The fact that, for $\Delta = 0.6$, the width of the first LL goes to zero for smaller magnetic fields suggests that there is no magnetic breakdown phenomenon in this large Δ limit where the figure-8-shape Fermi surfaces are well separated.

Fig. 4.20 shows the power spectrum associated with the oscillations in
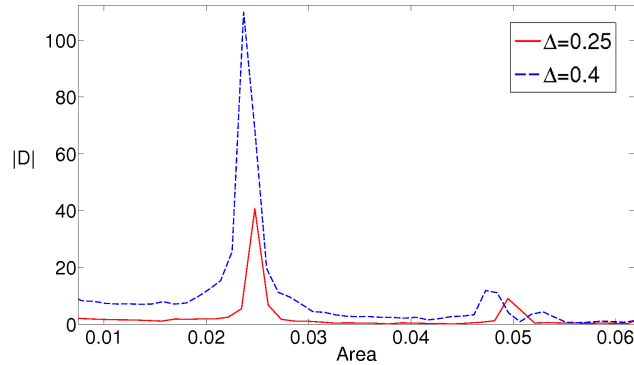
Figure 4.20 Power spectrum associated with the oscillations in the width for $\Delta = 0.25$ and $\Delta = 0.4$ at half-filling. The x axis is rescaled so that it corresponds to area in units of the area of BZ.

the width of the lowest energy peak for $\Delta = 0.25$ at half-filling. A sharp peak appears in this spectrum around 0.025, along with a second one that seems to correspond to a second harmonic. The area associated with quantum oscillations for other Δ values in Fig. 4.18 are also calculated and found to be consistent with the red colored (dark-shaded) areas shown in Fig. 4.19. Note that the areas of the gray (light-shaded) and the red (dark-shaded) regions are the same area. This is because, at half-filling, the two loops in the figure-eight-shaped segments have exactly the same area. The consistency is confirmed in Fig. 4.21 where the geometrical area corresponding to the red (or gray) regions in Fig. 4.19 and the area associated with quantum oscillations follow the same trend as a function of Δ. Note that, for large values of Δ, the FS areas are smaller than 1/8 of the BZ area, so we do not need to be concerned with the fact the measured QO areas are only modulo of 1/8.

It is worth noting that the average position of the lowest energy peak for $\mu = 0$ (which consists of two LLs) does not exhibit quantum oscillations for intermediate Δ, but rather scales linearly with B as expected for Landau levels. This is because the two Landau levels in this peak oscillate in opposite

directions. As a result, the oscillations in the width of this feature also reflect position oscillations of its two components.
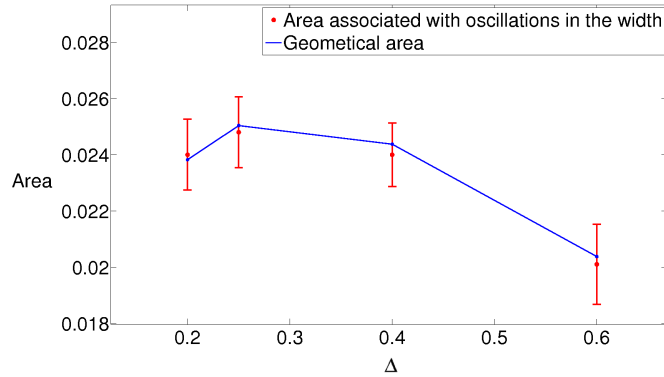
Figure 4.21 Comparison of the geometrical area (red or gray area in Fig. 4.19) and the area associated with quantum oscillations in the width of the lowest energy peak for different values of Δ at half-filling.
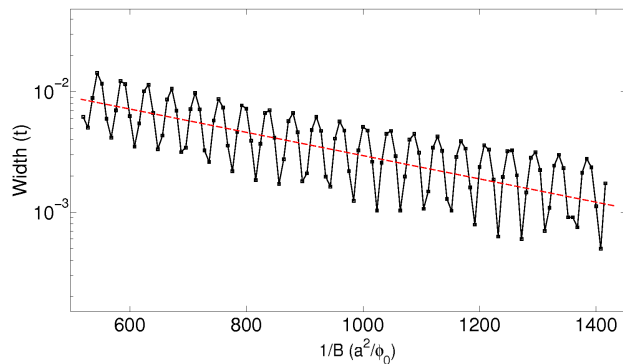
Figure 4.22 Semi-log plot of the width of the first LL for $\Delta = 0.4$ at half-filling as a function of $1/B$ showing a fairly linear average behavior for not very large fields. This is expected if the broadening is caused by magnetic breakdown. The dashed line is a linear fit to the data.

To summarize so far, we have seen that, at half-filling, sharp peaks with the degeneracy of two Landau levels are formed for large Δ where the figure-eight-shaped FS segments are well-separated. As Δ decreases, the gaps between figure-eight segments decrease and magnetic breakdown occurs which leads to broadening of the peaks. This is reflected in the smooth non-oscillatory

part of the curves in Fig. 4.18. According to the theory of magnetic break-
down,(Shoenberg, 1984) its probability is proportional to $\exp(-B_0/B)$ where
B_0 is a constant. Taking the broadening of the first peak as an estimate of
the probability of magnetic breakdown, we show the width as a function of
$1/B$ in a semi-logarithmic plot for $\Delta = 0.4$ in Fig. 4.22. The non-oscillatory
part exhibits a linear behavior in this semi-log plot which further supports
our argument that magnetic breakdown is responsible for broadening of the
Landau levels.

4.5.2 Nonzero μ

In subsection 4.5.1, we dealt with the half-filled case of π-striped superconduc-
tor where the two lobes of the figure-8-shaped Fermi surfaces have the same
area. There, we established the existence of magnetic breakdown in this sys-
tem. Here, we report on the observation of QO for non-zero μ. Away from
half filling, for example at $\frac{1}{8}$ doping, the Landau levels are well resolved. Each
peak has a number of states close to that of a LL, and the total number of
states in the two peaks related by $E \rightarrow -E$ symmetry is exactly twice the
degeneracy of a LL. This behavior is consistent with BdG calculations with
vortices, as shown in Fig. 4.2.

To better understand the quantum oscillations that exist in a π-striped
superconductor with intermediate pairing potential, we start from the large Δ
limit where, in our semiclassical approximation, the Landau levels are sharp
and magnetic breakdown is strongly suppressed.

The position of the first LL for $\Delta = 0.6$ and $\mu = -0.5$ corresponding
to 1/8 doping is plotted in the inset of Fig. 4.23 as a function of magnetic
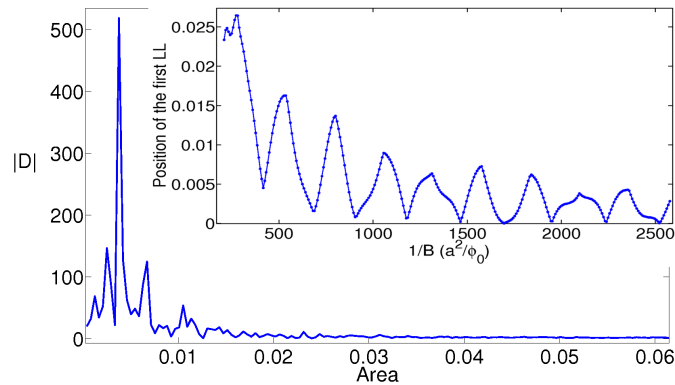
Figure 4.23 Power spectrum associated with the position of the first LL for $\Delta = 0.6$ and $\mu = -0.5$. The inset shows the position of the first LL for the same parameters.
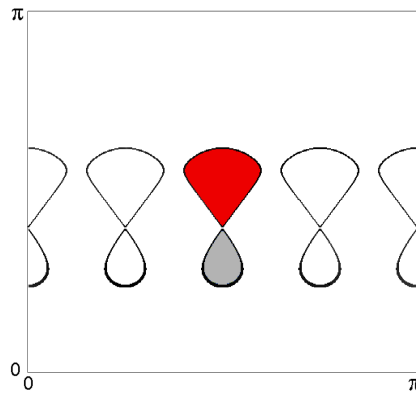
Figure 4.24 FS for $\Delta = 0.6$ and $\mu = -0.5$. The difference in the area of the the gray (light-shaded) and red (dark-shaded) areas gives rise to the strongest peak in the power spectrum of the position of the first LL.

field. The position shows an oscillatory behavior with a long period, which implies that the QO area is very small. The power spectrum associated with the position of the first LL for $\Delta = 0.6$ and $\mu = -0.5$ is shown in Fig. 4.23. Within error bars, the largest peak corresponds to the *difference* in the areas of the gray (light-shaded) and red (dark-shaded) areas shown in Fig. 4.24. Note that, semiclassically, the two area are traversed in opposite directions. The other two peaks on either side of the main peak correspond to the separate

gray (light-shaded) and red (dark-shaded) areas. Most likely, these two peaks arise due to a small gap where the two lobes meet, leading to small amplitude reflections into closed orbits around each lobe. Nevertheless, the oscillatory behavior that we measure corresponds predominantly to orbits around the figure-eight-shaped areas. For this value of Δ, there is no sign of magnetic breakdown across gaps separating neighboring figure-eights.
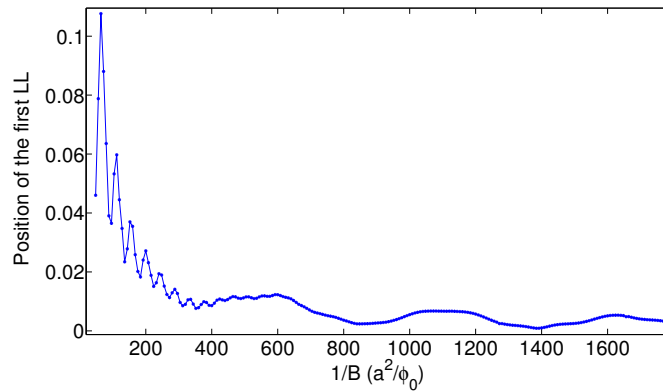
Figure 4.25 Position of the first LL for $\Delta = 0.5$ and $\mu = -0.4$.

Now we decrease Δ by a small amount in order to see what happens when magnetic breakdown is possible. Fig. 4.25 shows the position of the first LL for $\Delta = 0.5$ and $\mu = -0.4$. For larger magnetic fields, the short-period oscillations are due to magnetic breakdown and correspond to the red (dark-shaded) area shown in Fig. 4.26. Magnetic breakdown does not occur for smaller magnetic fields, and so only long-period oscillations occur at small B, corresponding to the difference in the areas of the two lobes in the figure-eight-shaped areas of Fig. 4.26.

This provides the key to understanding the semiclassical motion. One possible semiclassical motion is shown by the black arrows in Fig. 4.26. The phase that a quasiparticle gains by going around this path is proportional to the difference in the areas of the two lobes of figure-eight. The semiclassical
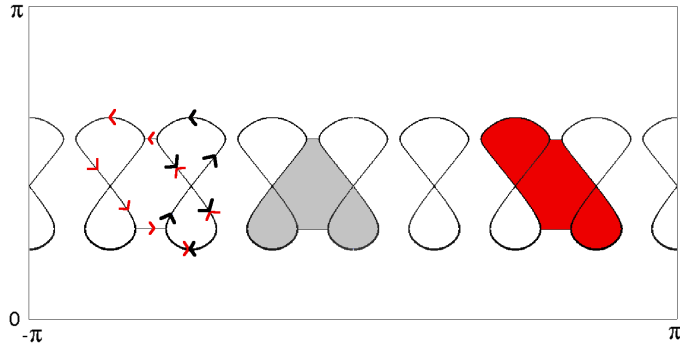
Figure 4.26 FS for $\Delta = 0.5$ and $\mu = -0.4$. The red area is associated with short-period oscillations in Fig. 4.25 for larger magnetic fields and the gray (light-shaded) area is associated with the oscillations in the width of the first LL when magnetic breakdown occurs. The difference in the area of the two lobes of the figure-eight results to long-period oscillations in Fig. 4.25 at smaller fields. Black (thin) and red (thin) arrows show the two possible semi-classical paths.

motion associated with magnetic breakdown is shown by the red (thin) arrows. In this case, the phase gained by precessing around the path is proportional to the red (dark-shaded) area. Like the small Δ case, we expect that the difference of the two paths to determine oscillations in the width of the position peak. Indeed this is what happens. The area associated with the oscillations in the width is equal to the gray (light-shaded) area in Fig. 4.26.

Having gained some physical insight from the case of very large Δ, we move on to the case of smaller Δ. In Fig. 4.27, we show the width and position of the first LL for $\Delta = 0.25$ and $\mu = -0.3$ corresponding to 1/8 doping. Both quantities show an oscillatory behavior as a function of $1/B$. The amplitude of oscillations is larger for the width and the frequency is slightly higher.

The power spectra associated with the position and width of the first LL for $\Delta = 0.25$ and $\mu = -0.3$, corresponding to 1/8 doping, are shown in Fig. 4.28. For simplicity, we limit our discussion to the largest position and width peaks which lie between 0.02 and 0.03 of the BZ. The position spectrum
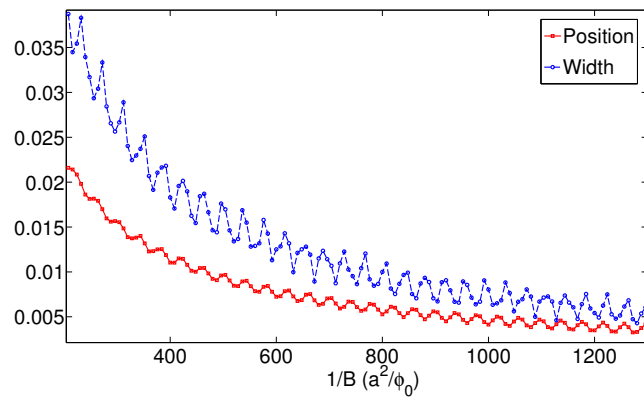
Figure 4.27 Position and width of the first peak for $\Delta = 0.25$ and $\mu = -0.3$, corresponding to $1/8$ doping, plotted versus $1/B$.
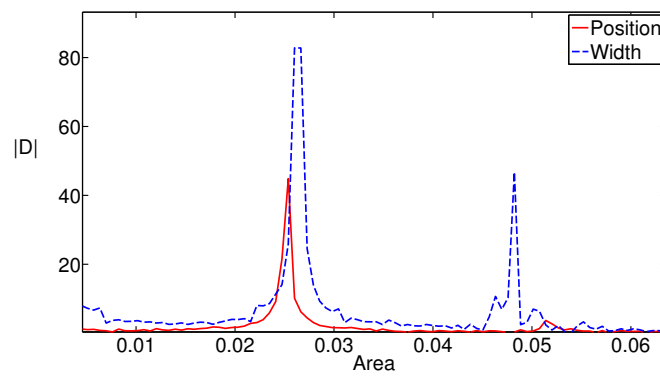
Figure 4.28 Power spectrum for $\Delta = 0.25$ and $\mu = -0.3$
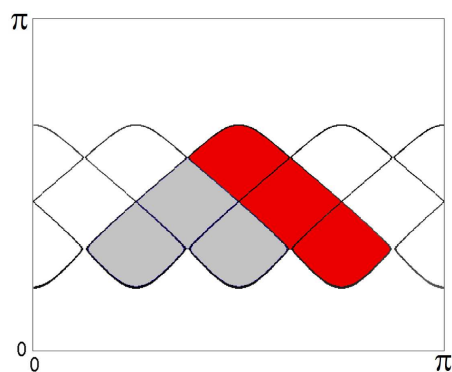
Figure 4.29 FS for $\Delta = 0.25$ and $\mu = -0.3$ in the quadrant of the first BZ.

exhibits a peak at around 0.025 which is due to magnetic breakdown and is associated with the red (dark-shaded) area in Fig. 4.29. In the width spectrum, there are two peaks. The first one, which is larger, is associated with the gray (light-shaded) area shown in Fig. 4.29. Note that the gray area can be thought as the red area minus the difference in the areas of the two loops of the figure-eight.

In Fig. 4.30, we have shown the consistency between the position and width spectra of the first peak and the geometrical area for $\Delta = 0.2$ as a function of the chemical potential. As μ becomes more negative, the area associated with the width oscillations becomes larger than the area associated with the position oscillations. This is consistent with the fact that the area of the lower loop of the figure-eight segments is larger than the upper loop for this smaller value of Δ. We will see in the next section that, near $\frac{1}{8}$ doping, the period of the oscillations in the specific heat, as calculated for this model, corresponds to that seen for the position of the first LL.
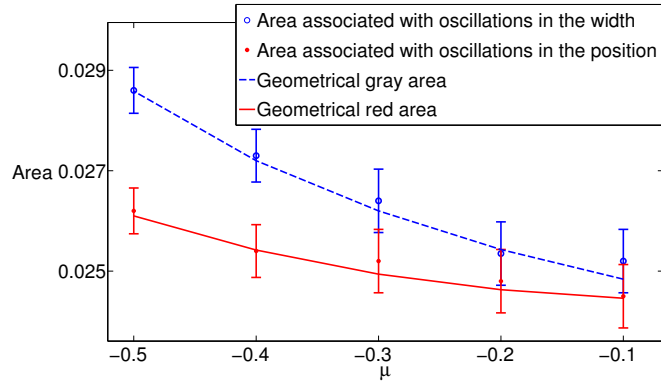
Figure 4.30 Comparison of the geometrical area and the area associated with quantum oscillations in the width and position of the first LL as a function of μ for $\Delta = 0.2$. The geometrical area is the area corresponding to the red (dark-shaded) region in Fig. 4.29 in the case of $\Delta = 0.2$.

4.5.3 Second nearest neighbor hopping

So far all the calculations were for the case where the second nearest neighbor hopping term was set to zero. To allow for the possibility of a more realistic band structure, calculations were also performed for $\Delta = 0.25$ and $t_2 = -0.15$ at 1/8 doping. The results are as expected from the $t_2 = 0$ calculations. The power spectrum for oscillations in the width and position of the lowest LL are shown in Fig. 4.31. The first peak associated with oscillations in the position of the first LL corresponds to the red (dark-shaded) area in Fig. 4.32. The first peak associated with the width of the first LL corresponds to the gray (light-shaded) area which is smaller than the red (dark-shaded) area. The calculation for non-zero t_2 demonstrates that the position and width frequencies are rather sensitive to the details of the band structure. However, we use the simplest model, with nearest neighbor hopping only, to make comparison to experiment in the next section. Since a number of factors could affect the frequencies, such as induced charge or spin order, our calculations can be taken as semi-quantitative when comparing to experiment.
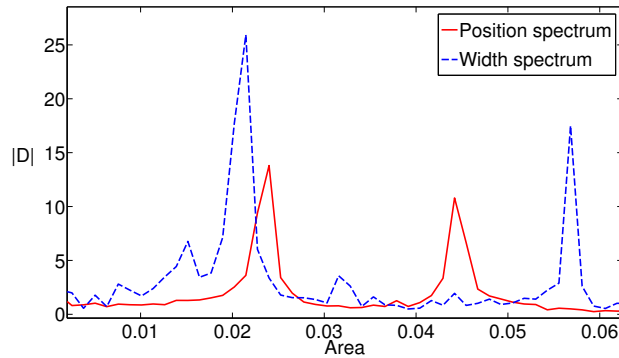
Figure 4.31 The spectra associated with oscillations in the width and position for $\Delta = 0.25$ and $t_2 = -0.15$ at 1/8 doping. The peaks correspond to the gray (light-shaded) and red areas shown in Fig. 4.32. The results are consistent with those for $t_2 = 0$.
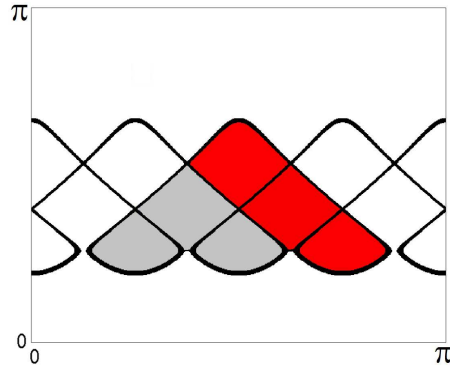
Figure 4.32 The areas associated with the first peaks of the position and width spectra in Fig. 4.31 for $\Delta = 0.25$ and $t_2 = -0.15$ at 1/8 doping.

4.6   Specific Heat
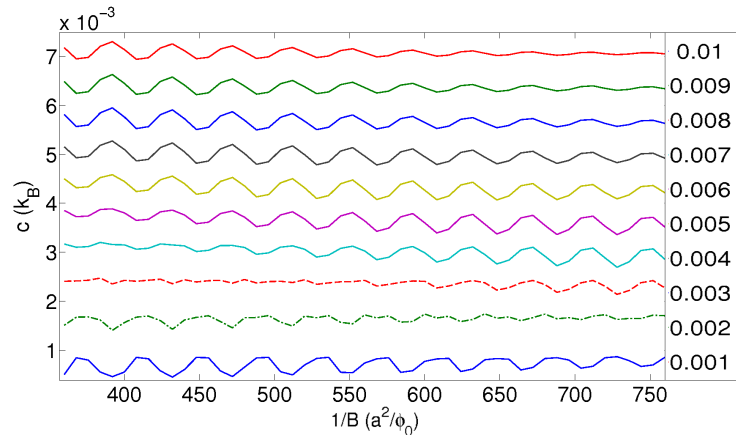
Figure 4.33 Specific heat versus $1/B$ for $\Delta = 0.25$ and $\mu = -0.3$ and $t_2 = 0$ for different temperatures. Temperatures in units of the hopping term, t, are shown on the right. Note the π phase shift in the oscillatory behavior of specific heat as T increases through $T^* \approx 0.003t$. The background specific heat at a given magnetic field changes linearly with T.

The question remains whether oscillations, related to those seen in the width and the position of the first LL, can be observed in a physically measurable quantity. In this section, we calculate the specific heat in order to make a connection to experiment. In chapter 3, it was shown that the specific heat of the model could be consistent with the observed specific heat of a cuprate

superconductor at $\frac{1}{8}$ doping in zero field or in the presence of a magnetic field by adjusting the value of the only parameter in the model, t. (Note that in chapter 3 and in this section we take $t_2 = 0$.) In chapter 3, using exact BdG result, the field dependence of the specific heat could not be studied in detail for the same reasons that quantum oscillations could not be measured, and, in addition, commensurability effects were exaggerated because of the restriction to commensurate vortex arrangements. Using the semiclassical approximation of this study, the magnetic field can be changed in relatively small steps, and, in addition, commensurability effects are not present. As a result, we are able to observe quantum oscillations in the specific heat.

For the following results, the same method and assumptions are made as in chapter 3. Fig. 4.33 shows the specific heat versus $1/B$ for $\Delta = 0.25$ and $\mu = -0.3$ at different temperatures. The oscillatory behavior corresponds to the same area as seen in the position oscillations of the first peak in Fig. 4.28 and corresponds to the red area shown in Fig. 4.29. Interestingly, there is a π shift in the oscillatory behavior of the specific heat at a temperature T^*. This is consistent with the Lifshitz-Kosevich (LK) formula for the specific heat (Riggs et $al.$, 2011).

To make a direct connection to the experimental data by Riggs et al., we have shown the oscillatory part of our specific heat calculations for $t = 0.16\text{eV}$ in Fig. 4.34. The figure can be compared to Fig. 2a of Ref. (Riggs et $al.$, 2011). The qualitative agreement is good, bearing in mind that we have used only one parameter t to fit the data. In addition, we have compared the oscillatory behavior part of the data in our model to the experimental data at $T = 1\text{K}$ in Fig. 4.35. The period of oscillations is shorter for our data because the quantum oscillation area is larger by about 20%. The fact that
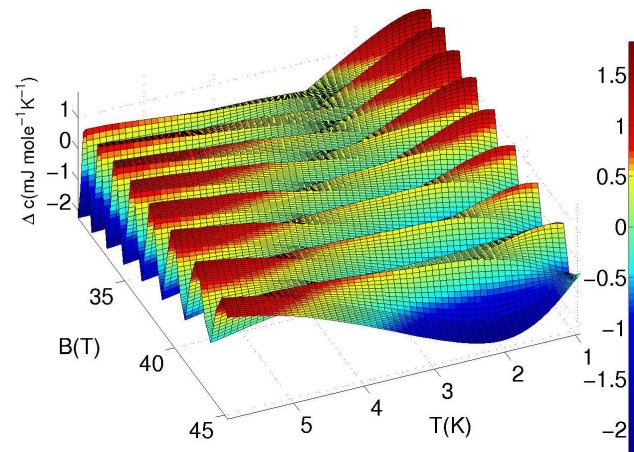
Figure 4.34 The oscillatory part of the calculated specific heat for $\Delta = 0.25$ and $\mu = -0.34$ with a zero second nearest neighbor hopping shown as a function of the magnetic field and temperature. To plot the data, $t = 0.16\text{eV}$ is chosen.
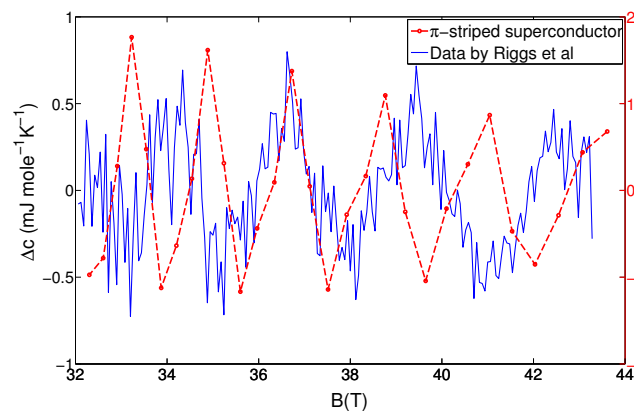
Figure 4.35 The oscillatory parts of the specific heat data by Riggs et al. and calculations for a π-striped superconductor at $T = 1\text{K}$ with $t = 0.16\text{eV}$, $\Delta = 0.25$ and $\mu = -0.3$. The left y-axis scale is for the experimental data and the right one is for the model.

the approximate magnitudes of the oscillations in the specific heat for the two data sets are similar supports the conjecture that the π-striped superconductor is a promising candidate model for explaining quantum oscillations in high T_c cuprates.

4.7   Summary and Conclusions

In this chapter, we have considered a model of sinusoidally modulated d-wave superconductivity, the π-stripe phase, in the presence of magnetic fields, and we have developed an approximate semiclassical method to calculate physical properties of this model as a function of field. In this model, the reconstructed FS arises from Andreev scattering by the periodic pairing potential which is different from the reconstructed Fermi surfaces due to spin waves.

Early in this chapter, we provided some evidence as to why the approximate method of ignoring vortices works for a π-striped superconductor. We have argued that a direct comparison of the low energy bands and the densities of states with and without vortices, for small and intermediate values of the gap amplitude, shows that, for both cases, these states resemble broadened Landau levels. We concluded that the effect of vortices is to modestly broaden and distort the bands. Furthermore, we examined the differences between this model and a d-wave superconductor. It was verified that neglecting vortices is not a good approximation for a uniform d-wave. For a d-wave superconductor, there are only 4 nodal points in the BZ where the pairing interaction vanishes. However, for a π-striped superconductor, there are extended FS regions where the effective pairing interaction vanishes and, hence, the FS acts like that of a metal. We concluded that this feature is the reason why the semiclassical

approximation works for a π-striped superconductor.

For the case of intermediate Δ in a π-striped superconductor, the DOS at $E = 0$ shows a discrepancy between the semiclassical approximation and the exact BdG calculations. However, as was discussed in chapter 3, this vortex lattice effect is for the rather artificial case of a commensurate, square vortex lattice. In reality the vortex lattice will adjust to conform to the modulated pairing potential, which we expect will reduce the perturbing effect of the superfluid velocity field. Furthermore, quantum oscillations are observed in the cuprates under conditions where the state is resistive, i.e., a vortex liquid state rather than an ordered vortex lattice. Studying the properties of a π-modulated vortex liquid state is a challenging problem. Nevertheless, one would expect the effects of the superfluid velocity to be reduced in such a state.

We find quantum oscillations in the specific heat in a model of π-striped superconductor with only nearest neighbor hopping present. The calculated QO is in qualitative agreement with the experimentally observed phenomenon in the cuprates. For example, the phase of the specific heat oscillations reverses at a temperature $T^*(B)$ which can be well fit by setting the hopping parameter $t = 0.16$eV. The frequency of oscillations is only about 20% larger than the experimental value. This is reasonable, bearing in mind that the second neighbor hopping term is set to zero. Beyond this, it is difficult to make detailed comparison because our model is strictly two-dimensional and does not include disorder.

Nevertheless, it is challenging to reconcile one feature of the cuprates with this model and that is the background $\sqrt{B}$ dependence of the specific heat. It should be noted that it is not clear from the data whether this $\sqrt{B}$

dependence persists to high magnetic field, or whether it is simply a low-field phenomenon. The data of Riggs et al. could, in principle, correspond to a system which switches from a low-field d-wave superconductor to a high-field π-stripe phase. Whether such a transition would be sharp or broad depends on how sensitive it is to disorder and vortex liquid effects.

In conclusion, we have studied a system in which spatially modulated pairing induces a non-zero density of particle-hole states near E_F which, in the presence of a magnetic field, forms broadened Landau levels and exhibits quantum oscillations. In light of the oscillations found in the specific heat, our model would be expected to give similar oscillations in all other quantities that are sensitive to the density of states near the Fermi energy. The model is distinctly different from conventional models of quantum oscillations in metals because of the paired nature of the quasiparticle states near the Fermi energy.

Chapter 5

Summary and Outlook

5.1 Summary

The work of this thesis is concerned with a model of a π-striped superconductor which has been proposed to describe the type of two-dimensional superconductivity seen within Cu-O planes in 1/8 doped $La_{2-x}Ba_xCuO_4$. This model has peculiar properties and is seen as a possible state of cuprates which might be stable under certain conditions. In this thesis, we focused on the properties of this model in a magnetic field. In particular, we spent a considerable amount of work investigating the existence of quantum oscillations in this model.

Chapter 2 of this thesis introduced this model of π-striped superconductor and examines how the DOS and spectral properties of this model vary as a function of the pairing potential, Δ. Unlike a uniform d-wave superconductor, this model exhibits an extended Fermi surface and has finite DOS at $E = 0$. Furthermore, for a certain range of values of Δ, the spectral function resembles the Fermi arcs seen in the ARPES measurements of the cuprates. We also find that, for not very large values of Δ, the majority parts of the FS

acts like a metal rather a superconductor (see Sec. 2.5).

In chapter 3, we calculate the DOS of a π-striped superconductor in the presence of a magnetic field using the Franz-Tesanovic gauge transformation. The main result of this chapter is that a periodic structure of the DOS is observed at low energies with a period that is proportional to B. This corresponds to the formation of Landau levels that are a coherent mixture of particles and holes. Furthermore, we showed that, this model is consistent with the specific heat measurements of cuprates in that it does not lead to the very large Sommerfeld coefficient that is predicted for the models based on FS reconstruction. As LLs are prerequisite for the existence of quantum oscillations, it is natural to ask whether the π-striped superconductor also supports the phenomenon. However, due to the particular method used in this chapter, we were not able to make connections to quantum oscillation experiments, by calculating the area associated with QO, as we were limited to only a few discrete values of the magnetic field.

In chapter 4, we employed a semiclassical approximation which allows much smaller increments in the magnetic field and provided justification for this approximation. Within this approximation, quantum oscillations were observed in a π-striped superconductor and the oscillation frequencies were related to the FS areas. In fact, for intermediate values of Δ, the QO area was found to be close to the experimentally measured value for the cuprates. In addition, the oscillatory part of the low-temperature specific heat calculated for this model was shown to be in qualitative agreement with experiments. The QO in this chapter are found within the employed semiclassical approximation and still require proof by exact BdG calculations. In conclusion, the work of this thesis suggests that a π-striped superconducting model is a promising

candidate to explain the QO phenomenon in the cuprates.

5.2   Outlook

At this point in time, the π-striped superconductor is a fairly new model and, so, many questions about this model remain to be answered. In this section, we suggest possible new studies on this model which would help to examine the possible connection of this model to the cuprates. One question which immediately comes to mind is whether such a state is likely to occur in the high T_c cuprates. Arguments for the occurrence of a π-striped superconducting state have been given earlier by Berg, Fradkin and Kivelson.(Berg *et al.*, 2007, 2009) Note that another possible superconducting state associated with stripes could be one in which the superconducting order parameter oscillates in magnitude but does not change sign. This is a uniform d-wave but modulated due to interactions favoring stripe formation. There have been several numerical studies (Corboz *et al.*, 2011; Raczkowski *et al.*, 2007; Loder *et al.*, 2010) investigating whether striped states arise from the t-J model. They find that the two states, one in which the gap oscillates in magnitude but does not change sign and the other in which the sign of the gap oscillates, are extremely close in energy. To go beyond this investigations, one needs a microscopic Hamiltonian that stabilizes stripes at the mean field level. The discovery of such a microscopic Hamiltonian is the key to understanding the stripe order.

One feature of the cuprates which is absent in this model of a π-striped superconductor is the background $\sqrt{B}$ dependence of the specific heat. However, it is not clear whether the dependence persists exactly at higher fields

where the QO occurs. To address this problem in detail, one needs to examine the relative stability of the π-stripe and a uniform d-wave. It has already been shown in experimental studies that stripe order can be induced by a magnetic field. In fact, based on the "nodal-antinodal dichotomy" which characterizes the sharp distinction between the nature of electronic excitations in the nodal and antinodal regions, it has been speculated before that there are distinct superconducting types of order parameter, one is spatially uniform and the other is spatially modulated (PWD) (Berg *et al.*, 2009). The PDW state gradually becomes stable as temperature decreases and the uniform order parameter becomes more stable with the possibility that the two orders coexist at some temperature range. It is possible that the same behavior occurs as a function of magnetic field. It is interesting to speculate that there could be a smooth transition from a uniform d-wave to a modulated d-wave state as magnetic field increases. Again, understanding the details of such a transition would require a microscopic Hamiltonian which stabilizes stripe order.

Nevertheless, one can study some properties of the π-striped superconductor without a microscopic Hamiltonian. Our method in this thesis, allows for the calculation of quantum oscillations in physical properties, such as the specific heat presented in chapter 4. It is left as future work to calculate oscillations in the magnetic susceptibility, resistivity and Hall resistivity. In addition, the mixed state of cuprates is believed to be in a state of quantum vortex liquid state. Although complicated, it would be beneficial to study the implications of such a state in more detail. One expects that one feature of a quantum vortex liquid is that the commensurability effect, seen in chapter 3 for a perfect vortex array, will be absent in the vortex liquid state. This suggests that the semiclassical approximation in chapter 4 may give a good description

under conditions where quantum oscillations are seen experimentally in the cuprates.

Finally, one expects a π-striped superconductor to coexist with spin and charge density wave order. Consequently, one expects the reconstructed FS due to all intertwined order parameters to be rather different from that due to only the superconducting order parameter. Again, further study in this direction requires a microscopic Hamiltonian to determine the relative magnitude of all the order parameters by self-consistent calculations. This would provide a more realistic model of the cuprates.

Electrons in a Magnetic Field

In this appendix, we first show how the energy spectrum of a free electron system develops Landau levels (LLs) in the presence of a magnetic field. Next, we show that tight-binding electrons also show discrete band structure that, in the small magnetic field limit, resembles LLs.

To find the energy spectrum of a free electron in a magnetic field, one needs to solve the following Schrodinger equation

$$\frac{1}{2m}(\frac{\hbar}{i}\nabla + \frac{e}{c}A(r))^2\psi(r) = \epsilon\psi(r) \qquad \text{(A.1)}$$

where $A(r)$ is the vector potential. There are two extensively used gauges: Landau gauge $A(r) = (0, Bx, 0)$ and the symmetric gauge $A(r) = \frac{1}{2}(-By, Bx, 0)$. Here we use Landau gauge which is als o used in chapter 4. The Hamiltonian (A.1) becomes

$$H = -\frac{\hbar^2}{2m}(\frac{\partial^2}{\partial x^2} + (\frac{\partial}{\partial y} + i\frac{eB}{\hbar c}x)^2 + \frac{\partial^2}{\partial y^2}). \qquad \text{(A.2)}$$

Because of translational symmetry in the y and z directions, we try the fol-

lowing function as the solution

$$\psi(r) = u(x)e^{ik_y y}e^{ik_z z}. \tag{A.3}$$

Then Eq. (A.2) becomes

$$\frac{\hbar^2}{2m}\frac{\partial^2 u(x)}{\partial x^2} + \frac{e^2 B^2}{2mc^2}(x + \frac{\hbar k_y}{eB})u(x) = (\epsilon - \frac{\hbar^2 k_z^2}{2m})u(x), \tag{A.4}$$

which is the Schrodinger equation of a one dimensional particle in a harmonic potential centered at

$$x_0 = -\hbar k_y/eB \tag{A.5}$$

with cyclotron frequency $\omega_c = eB/mc$. Consequently the solution gives the energy levels given by

$$(\epsilon_n - \frac{\hbar^2 k_z^2}{2m}) = (n + 1/2)\hbar\omega_c \tag{A.6}$$

where n is an integer.

The solution of (A.4) is highly degenerate. This is due to the fact that the eigenvalues do not depend on the quantum number k_y and, as a result, the energy spectra is the same for different values of k_y. One can qualitatively calculate the degree of degeneracy. k_y, which is the y component of the wavevector, is a multiple integer p of $2\pi/L_y$ where L_y is the length of the system in y direction. On the other hand $x_0 = -\hbar k_y/eB$ should lie within the system size, so that $0 < x_0 < L_y$. This gives

$$-\frac{eB}{\hbar}L_x < \frac{2\pi}{L_y}p < 0 \tag{A.7}$$

which means that the number of allowed values for integer p is $\frac{eB}{h}L_x L_y =$

$\frac{eB}{h}A$ where A is the area of the sample. Hence, the degeneracy of the LLs is proportional to the area of the sample (Yoshioka, 2002).

The energy spectra of electrons moving in a periodic potential is also of interest. Here we find the solution to the problem of electrons on a lattice where we assume that the electron are tightly bound to the underlying lattice. The resulting model is called the tight-binding model. The basis states consist of Wannier functions which are orthogonal functions centered at lattice sites. In the absence of the electron-electron interaction, the tight-binding Hamiltonian in the second quantization notation is given by

$$H = -\sum_{ij} t c_i^\dagger c_j e^{iA_{ij}} \tag{A.8}$$

where t is the hopping energy term which is tied to the fact an electron reduce its energy by hopping from one site to another. A_{ij} is the integral of vector potential from the i-th site to its nearest neighbor j-th site. Using Landau gauge, the Schrodinger equation becomes (Hofstadter, 1976)

$$-t[\psi(x+1,y) + \psi(x-1,y) + e^{ieaBx/\hbar}\psi(x,y+1) \quad +e^{-ieaBx/\hbar}\psi(x,y-1)] = \epsilon\psi(x,y)$$

where x and y are in units of the lattice constant, a. $\psi(x,y)$ is the coefficient associated with the Wannier function centered at site (x,y) and can be viewed as the wave function which gives the probability of finding an electron at site (x,y). Like the continuum case, we write the wave function as $\psi(x,y) = g(x)e^{iky}$ which means that the magnetic unit cell is a long row magnetic unit cell in the x direction. Next we find the equation for the function $g(m)$ as follows

$$-t[g(m+1) + g(m-1) + 2\cos(2\pi x\alpha + k)g(m)] = \epsilon g(m) \tag{A.9}$$

where $\alpha = \frac{a^2 B}{\phi_0}$ is the ratio of the flux through one primitive unit cell to the flux quantum. Equation (A.9) is called the Harper equation. When α is a rational number, the Harper equation solution leads to the Hofstadter energy spectrum and its dependence on α resembles a butterfly, the so-called Hofstadter butterfly (Hofstadter, 1976). The bands become narrower as the magnitude of the magnetic field decreases and eventually become very sharp levels that resemble Landau levels. In this thesis, we also call these narrow bands Landau levels.
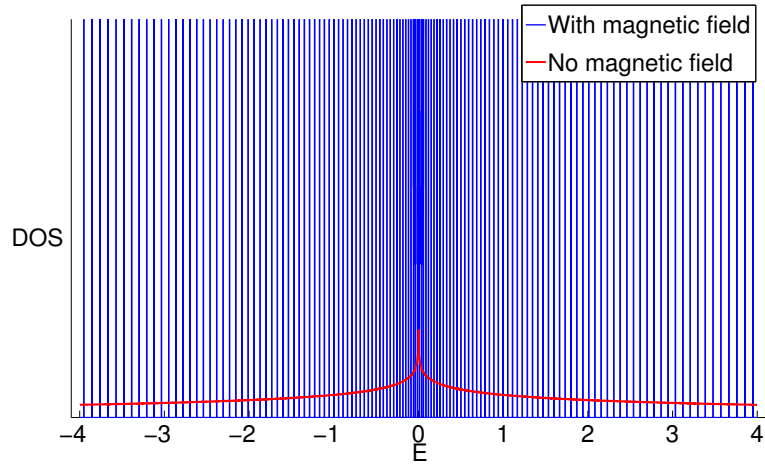
Figure A.1 The DOS as a function of energy E for $\alpha = 1/128$ and $\mu = 0$. LLs are seen everywhere except around $E = 0$ where the van-Hove singularity occurs at $E = 0$. The red curve shows the DOS in zero magnetic field.

Figure A.1 shows the DOS as a function of energy for zero field and $\alpha = 1/128$. Note that $\alpha = 1/128$ is equivalent to $L = 128$ where L is the number of sites in a magnetic unit cell in chapter 4. LLs are seen everywhere except around $E = 0$ where the van Hove singularity occurs. Unlike the continuum case where the LL spacing is constant, the LL spacing is energy dependent and is inversely proportional to the DOS in the absence of a magnetic field. To deal with this, it is convenient to define an effective mass. This topic is discussed in appendix D in detail.

When there is a pairing potential, one can get equations similar to (A.9)

only if the effect of vortices is neglected. Using the semiclassical approximation in chapter 4 (see Eq. (4.4)), one can follow the same procedure as described above and obtain two Harper-type equations as follows

$$
\begin{aligned}
&- t[u(m+1) + u(m-1) + 2\cos(2\pi x\alpha + k)u(m)] - \mu u(m) \qquad \text{(A.10)}\\
&+ \Delta_{m-}v(m-1) + \Delta_{m+}v(m+1) + \Delta_m \cos(2\pi x\alpha + k)v(m) = \epsilon u(m)
\end{aligned}
$$

and

$$
\begin{aligned}
&t[v(m+1) + v(m-1) + 2\cos(2\pi x\alpha + k)v(m)] + \mu v(m) \qquad \text{(A.11)}\\
&+ \Delta_{m-}u(m-1) + \Delta_{m+}u(m+1) + \Delta_m \cos(2\pi x\alpha + k)u(m) = \epsilon v(m).
\end{aligned}
$$

Here $\Delta_{m\pm} = \Delta\cos(q_x(x - 1/2 \pm 1/2))$ and $\Delta_m = -\Delta\cos(q_x(x - 1/2))$ for a π-striped superconductor. The two equations are two BdG-type equations similar to (2.11) and (2.12). They can be solved the same way as a BdG Hamiltonian. Note that these are the two equations one obtains in Landau gauge which is the gauge that enables us to work with row unit cells. The majority of results in chapter 4 are based on the solutions to (A.10) and (A.11).

Singular Gauge Transformations

The BdG Hamiltonian both in the continuum limit and on a lattice has the following form

$$H = \begin{pmatrix} \hat{h} & \hat{\Delta} \\ \hat{\Delta}^* & -\hat{h}^* \end{pmatrix}$$

where there is a phase $\phi(r)$ associated with the order parameter operator, $\hat{\Delta}$. It is convenient to remove the phase by a proper gauge transformation U so that

$$H \to U^{-1}HU \tag{B.1}$$

is not phase dependent. In the absence of vortices, this can be achieved by the symmetric gauge transformation given by

$$U = \begin{pmatrix} e^{i\phi(r)/2} & 0 \\ 0 & e^{-i\phi(r)/2} \end{pmatrix} \tag{B.2}$$

However, in the presence of vortices, the phase of the order parameter acquires a global curvature which satisfies

$$\nabla \times \nabla \phi = 2\pi \sum_i \delta(r - r_i). \tag{B.3}$$

In other words, the phase should wind by 2π when going around a vortex. Consequently, the transformation (B.2) is not single valued in the presence of vortices In principle, one can use branch cuts to assure single valueless. To avoid this, one needs to use singular gauge transformations. They are three singular gauges available: the first two proposed by Anderson are

$$U = \begin{pmatrix} e^{i\phi(r)} & 0 \\ 0 & 1 \end{pmatrix} \tag{B.4}$$

$$U = \begin{pmatrix} 1 & 0 \\ 0 & e^{-i\phi(r)} \end{pmatrix}. \tag{B.5}$$

Gauge transformation (B.4) is used in chapter 4. The third gauge transformation, proposed by M. Franz and Z. Tesanovic, is used in chapter 3 and is given by

$$U = \begin{pmatrix} e^{i\phi_e(r)} & 0 \\ 0 & e^{-i\phi_h(r)} \end{pmatrix} \tag{B.6}$$

where $\phi_e(r)$ and $\phi_h(r)$ satisfy $\phi_e(r) + \phi_h(r) = \phi(r)$. In all of the above gauge transformations, $\phi(r)$ satisfies Eq. (B.3). Intuitively, the Franz-Tesanovic (FT) gauge transformation divides the vortices into two groups, e and h. Each group is only seen by either electrons or holes. The differential equation for the phase $\phi_\mu(r)$, where μ is either e or h, is given by

$$\nabla \times \nabla \phi_\mu = 2\pi \sum_i \delta(r - r_i^\mu). \tag{B.7}$$

Likewise, we need to define two superfluid velocities associated with either e or h type vortices according to

$$v_s^\mu(r) = \frac{1}{m}(\hbar\nabla\phi_\mu(r) - \frac{e}{c}A(r)) \tag{B.8}$$

where $A(r)$ is the vector potential associated with the magnetic field. Taking the curl of the above equation and using Eq. (B.7), we get

$$\nabla \times v_s^\mu = \frac{2\pi\hbar}{m}[\hat{z}\sum_i \delta(r - r_i) - B/\phi_0]$$
(B.9)

which is used in appendix C to find the superfluid velocity associated with either holes or electrons.

For a superconducting system on a lattice, the tight-binding BdG given by Eq. (4.1) transforms to

$$H = \begin{pmatrix} -t\sum_\delta e^{iv_\delta^e(r)}\hat{s}_\delta - \mu & \sum_\delta \Delta_\delta e^{i\Lambda_\delta(r)}\hat{s}_\delta \\ \sum_\delta \Delta_\delta e^{i\Lambda_\delta(r)}\hat{s}_\delta & t\sum_\delta e^{-iv_\delta^h(r)}\hat{s}_\delta + \mu \end{pmatrix}$$
(B.10)

under the FT gauge transformation where $v_\delta^\mu(r) = \int_r^{r+\delta} dr v_s^\mu(r)$ and $\Lambda_\delta(r) = \int_r^{r+\delta} dr[v_\delta^e(r) - v_\delta^h(r)]$. The Hamiltonian is periodic with periodicity of either type vortices. The periodic vortex array defines a magnetic unit cell so that each magnetic unit cell has two vortices inside, one type e and one type h. The magnetic field is inversely proportional to the area of the magnetic unit cell. Due to periodic structure of the superfluid velocities, one can use the Bloch theorem outlined in chapter 2 to find the solution to Eq. (B.10).

Appendix C

Superfluid Velocity

The line integral of the superfluid velocity associated with μ type (electron or hole type) vortices from one site to its nearest neighbor enters in Eq. (B.10). Hence, to build the Hamiltonian, one first needs to find the superfluid velocities. In this appendix, we show how to derive the superfluid velocity v_s^μ associated with the group type $\mu = e(h)$ on a lattice. We find the local superfluid velocities on each lattice site and also on the links connecting the sites. The latter is needed to have a good approximation of the integral. We start with the following two equations for the superfluid velocity

$$\nabla \times v_s^\mu = \frac{2\pi\hbar}{m}[\hat{z}\sum_i \delta(r - r_i^\mu) - B/\phi_0] \tag{C.1}$$

$$\nabla \cdot v_s^\mu = 0 \tag{C.2}$$

where the summation in (C.1) is over all the vortices of type μ. To use an easier notation here, we denote the $x(y)$ component of v_s^μ on site i with $v_i^{x(y)}$. We drop the μ index and only find $v_i^{x(y)}$ for type e vortices. $v_s^{x(y)}$ for h type vortices can be found by shifting $v_i^{x(y)}$ by half of the diagonal of the magnetic unit cell as seen in figure 3.1.

We derive $v_s^{x(y)}$ in a few steps as follows: we first calculate B_k, the

Fourier transform of the magnetic field as it is needed later in our calculations. Next Stokes' and Gauss's theorems are applied to equations (C.1) and (C.2) on a grid with spacing, b, equal to half of the lattice constant. This is because we also need $v_i^{x(y)}$ on the links connecting the lattice sites. Then we take the Fourier transform of the resulting equations and solve the equations in k space. Finally, the superfluid velocity is converted back to the position space.

First, to find the magnetic field in k-space, we start with the London equation

$$B - \lambda^2 \nabla^2 B = \frac{\phi_0}{2} \sum_i \delta(r - r_i) \qquad (C.3)$$

where λ is the London penetration depth. Magnetic field and the δ function in k-space are given by

$$B = \frac{1}{N} \sum_k e^{ik \cdot r} B_k \qquad (C.4)$$

$$\sum_i \delta(r - r_i) = \frac{1}{N} \sum_i \sum_k e^{ik \cdot (r - r_i)} \qquad (C.5)$$

where N is the number of grid points and the summation over k runs over the reciprocal grid vectors. Substituting these definitions in Eq. (C.3) and using the definition of the Laplacian on a lattice,

$$\nabla^2 e^{ik \cdot r} = -\frac{e^{ik \cdot r}}{b^2} [(1 - e^{ik_x})(1 - e^{-ik_x}) + (1 - e^{ik_y})(1 - e^{-ik_y}))], \qquad (C.6)$$

we can solve the London equation in k space and get

$$\Rightarrow B_k = \frac{\phi_0}{2} \frac{\sum_i e^{ik \cdot r_i}}{1 + \frac{\lambda^2}{b^2}[(1 - e^{ik_x})(1 - e^{-ik_x}) + (1 - e^{ik_y})(1 - e^{-ik_y}))]} \qquad (C.7)$$

which we will use later in our calculation. Note that e^{ik_x} is $e^{ik_x b}$ where b is set to 1 for convenience. Next we apply Gauss' theorem to the divergence Eq.

(C.2). On a grid, it becomes

$$v_r^x - v_{r+\hat{x}}^x - v_{r+\hat{x}+\hat{y}}^x + v_{r+\hat{y}}^x + v_r^y + v_{r+\hat{x}}^y - v_{r+\hat{y}}^y - v_{r+\hat{x}+\hat{y}}^y = 0 \qquad (C.8)$$

Its Fourier transform is

$$v_k^x(1 + e^{ik_y} - e^{ik_x} - e^{ik_x+ik_y}) + v_k^y(1 + e^{ik_x} - e^{ik_y} - e^{ik_x+ik_y}) = 0 \qquad (C.9)$$

$$\Rightarrow v_k^y = -\frac{(1 + e^{ik_y})(1 - e^{ik_x})}{(1 + e^{ik_x})(1 - e^{ik_y})} v_k^x \qquad (C.10)$$

which is the same as

$$v_k^y = -\frac{\sin(k_x/2)}{\sin(k_y/2)} v_k^x. \qquad (C.11)$$

Now we apply Stokes' theorem to (C.1). Going around the shaded square in

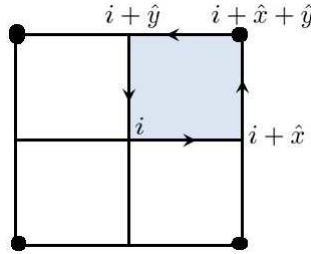Figure C.1 The application of Stokes' theorem to a grid used in this appendix to calculate the superfluid velocity. The black dots denote the position of the sites.

Fig. C.1, we have

$$b/2(v_r^x + v_{r+\hat{x}}^x - v_{r+\hat{x}+\hat{y}}^x - v_{r+\hat{y}}^x - v_r^y + v_{r+\hat{x}}^y - v_{r+\hat{y}}^y - v_{r+\hat{x}+\hat{y}}^y) = \phi \qquad (C.12)$$

where ϕ is the flux of the right hand side of (C.1) through the square. Per-

forming Fourier transform, we get

$$b/2[v_k^x(1+e^{ik_x})(1-e^{ik_y}) - v_i^y(1+e^{ik_y})(1-e^{ik_x})] = \phi_k \qquad \text{(C.13)}$$

$$v_k^x = \frac{(1+e^{ik_x})(1-e^{ik_y})}{[(1-e^{ik_y})(1+e^{ik_x})]^2 + [(1+e^{ik_y})(1-e^{ik_x})]^2} \frac{2\phi_k}{b} \qquad \text{(C.14)}$$

$$\Rightarrow v_k^x = \frac{(1+e^{ik_y})(1-e^{ik_x})}{(1-e^{ik_x+ik_y})^2 + (e^{ik_x} - e^{ik_y})^2} \frac{\phi_k}{b}. \qquad \text{(C.15)}$$

In the next step, we calculate ϕ_k. The flux, approximated by the value of right hand side of Eq. (C.1) on four corners of the shaded square in Fig. C.1, is given by

$$\phi = \frac{2\pi\hbar}{m} \frac{b^2}{4} \left[\sum_i \delta(r - r_i^\mu) - B(r)/\phi_0 + \sum_i \delta(r + \hat{x} - r_i^\mu) - B(r+\hat{x})/\phi_0 + ... \right)$$

$$\text{(C.16)}$$

which in k space is given by

$$\phi_k = \frac{2\pi\hbar}{m} \frac{b^2}{4} \left(\sum_i e^{-ik \cdot r_i^\mu} \right) f(k)(1 + e^{ik_x} + e^{ik_y} + e^{ik_x+ik_y}) \qquad \text{(C.17)}$$

where

$$f(k) = 1 - \frac{1}{1 + \lambda^2/b^2[(1-e^{ik_x})(1-e^{-ik_x}) + (1-e^{ik_y})(1-e^{-ik_y}))]} \qquad \text{(C.18)}$$

$$= \frac{\lambda^2/b^2[(1-e^{ik_x})(1-e^{-ik_x}) + (1-e^{ik_y})(1-e^{-ik_y}))]}{1 + \lambda^2/b^2[(1-e^{ik_x})(1-e^{-ik_x}) + (1-e^{ik_y})(1-e^{-ik_y}))]}. \qquad \text{(C.19)}$$

Note that, $f(k)$ can be well approximated to be equal to one for a type II superconductor except for $k = 0$ which gives $f(k) = 0$. We substitute ϕ_k into

(C.15) and simplify to get

$$v_k^x = \frac{A(\sum_j e^{ik\cdot(i-r_j)})(1+e^{ik_y})(1+e^{ik_x})^2(1-e^{ik_y})}{(1-e^{ik_x+ik_y})^2 + (e^{ik_x}-e^{ik_y})^2} \tag{C.20}$$

where $A = \frac{\pi\hbar}{m}\frac{b}{2}$ and which is valid for $k \neq 0$. Note that v_i^y can be easily calculated using Eq. (C.11). Taking the inverse Fourier transform of (C.20) gives the superfluid velocity in position space.

SPECIFIC HEAT

One can calculate specific heat by using the relationship $c = T\frac{\partial S}{\partial T}$. For a system of independent fermionic quasiparticles, the entropy, S, is given by (de Gennes, 1989)

$$S = -k_B \sum_{k\alpha}[f_k \ln f_k + (1 - f_k)\ln(1 - f_k)] \tag{D.1}$$

where α is the spin degree of freedom and f_k is the Fermi-Dirac distribution function given by

$$f_k = \frac{1}{1 + \exp(\epsilon_k/k_B T)} \tag{D.2}$$

where ϵ_k is the energy of the quasiparticle associated with the state k and its dependence on α is implicit. Then the specific heat is calculated as follows

$$c = -k_B T \sum_{k\alpha}[(\partial f_k)\ln f_k - (\partial f_k)\ln(1 - f_k)] \tag{D.3}$$

$$= -k_B T \sum_{k\alpha}[\partial f_k(\ln\frac{f_k}{1 - f_k})] \tag{D.4}$$

where the notation $\partial f_k = \partial f_k / \partial T$ is used. So

$$c = \sum_{k\alpha} \epsilon_k \partial f_k \tag{D.5}$$

$$= \frac{1}{k_B} \sum_{k\alpha} \epsilon_k^2 / T^2 \frac{\exp(\epsilon_k/k_B T)}{(1 + \exp(\epsilon_k/k_B T))^2}. \tag{D.6}$$

Now, by using the definition of the density of states, the sum can be transformed into an integral over energy as follows

$$c_v = k_B \int_{-\infty}^{\infty} d\epsilon D(\epsilon) \left(\frac{\epsilon}{k_B T}\right)^2 \frac{\exp(\epsilon/k_B T)}{(1 + \exp(\epsilon/k_B T))^2}. \tag{D.7}$$

where c_v is the specific heat per volume and $D(\epsilon)$ is the density of states per unit volume per unit energy. For a metallic system at low temperatures, the low-energy density of states is fairly constant and can be approximated by its value at Fermi energy, $D(\epsilon_f)$. Consequently, we have

$$c_v = 2k_B^2 T D(\epsilon_f) \int_0^{\infty} dx\, x^2 \frac{\exp(x)}{(1 + \exp(x))^2} \tag{D.8}$$

where the integral variable is changed from ϵ to $x = \epsilon/k_B T$. The answer to the integral is $\pi^2/6$ and the specific heat becomes

$$c_v = \pi^2 k_B^2 T D(\epsilon_f)/3 \tag{D.9}$$

which shows the linear dependence of c_v on T as expected. One can see that the Sommerfeld coefficient, $\gamma = c/T$, is proportional to the density of states at Fermi energy.

Eq. (D.7) can be used for a superconductor. The only difference is that, by convention, we only work with positive-energy quasiparticles. So, now, $D(\epsilon)$ in Eq. (D) is the sum of the positive and negative density of states and the integral starts from zero.

To compare the specific heat of a metal to that of a free electron system, it is conventional to define a quantity called the effective mass, m^*. For a 3-dimensional system, we have

$$\gamma = \frac{k_B^2}{\hbar^2} (\frac{\pi^2}{3})^{2/3} m^* n^{1/3} \tag{D.10}$$

where n is the carrier density (Harshman *et al.*, 1989).

For a two-dimensional system, the specific heat per unit area is defined as $c_A = \gamma_A T$ where γ_A is given by

$$\gamma_A = \frac{\pi^2 k_B^2}{3} D_A(\epsilon_f). \tag{D.11}$$

In Eq. (D.11), $D_A(\epsilon_f)$ is the density of states per unit energy per unit area. However, in reality, we have a stack of two dimensional systems with spacing p and what is measured is still the specific heat per volume. To relate c_v to c_A for these systems, we write

$$c_v = \frac{1}{V} \frac{dU}{dT} = \frac{1}{p} (\frac{1}{nA} \frac{dU}{dT}) = \frac{1}{p} c_A \tag{D.12}$$

where n is the number of layers in the sample. This means that the Sommerfeld coefficient of quasi two-dimensional systems measured in experiments is

$$\gamma = \frac{\pi^2 k_B^2}{3} D_A(\epsilon_f) \frac{1}{p} \tag{D.13}$$

$$= \frac{\pi^2 k_B^2}{3} D_e \frac{m^*}{m} \frac{1}{p} \tag{D.14}$$

where $D_e = \frac{m}{\pi \hbar^2}$ is the density of states of a free electron gas in two dimensions and is independent of energy. One advantage of writing the coefficient as in Eq. (D.14) is that, under certain conditions as will be shown, the effective mass, m^*, is the same as the cyclotron mass that is measured in quantum

oscillations experiments for two-dimensional systems.

The specific heat calculated here is per volume and needs to be converted to per mole for easier comparison with experiments. To do so, one needs to multiply the Sommerfeld coefficient by $\frac{N_A}{n}$ where N_A is the Avogadro number and n is the number of carriers in unit volume. We have

$$\gamma = \frac{\pi^2 k_B^2}{3} D_e \frac{m^*}{m} N_A \left(\frac{V}{pN}\right) \tag{D.15}$$

where N is the number of carriers in the sample. The quantity inside the bracket is the area of each unit cell. For a cuprate, it can be approximated by $a^2 = (3.85\text{Å})^2$ and, consequently, we get $\gamma = 1.46$ mJ mole^{-1}K^{-2} $\left(\frac{m^*}{m}\right)$. This explains the factor 1.46 in Riggs *et al.* (2011).

The cyclotron frequency, ω_c is equal to $\frac{eB}{m\hbar}$ for a two-dimensional free electron gas. For a general physical system, this is not the case. However, it is convenient to define a cyclotron effective mass, m_c, such that the LL spacing $\hbar\omega_c = \frac{\hbar eB}{m_c c}$. Now we show that, the effective mass defined for specific heat, m^*, is the same as m_c for a closed FS in two dimensions. From semiclassical physics, the cyclotron effective mass is given by

$$m_c = \frac{\hbar^2}{2\pi} (\partial A/\partial \epsilon) \tag{D.16}$$

where A is the area of the FS. On the other hand, the density of states of a closed FS in two dimensions is given by $D(\epsilon) = \frac{2}{4\pi^2} \partial A/\partial \epsilon$. This means that

$$m_c = \frac{\hbar^2}{2\pi} 2\pi^2 D(\epsilon) = m \left(\frac{D(\epsilon)}{D_e}\right) \tag{D.17}$$

which is the exact same definition of m^* as in (D.14). m_c is a quantity that determines the spacing of LLs through $\omega_c = \frac{eB}{m_c c}$. For a constant magnetic field, a small spacing means large m_c and vice versa. As shown in Eq. (D.17),

m_c is proportional to the density of states at Fermi energy. This means that, for a large $D(\epsilon_f)$, the LL spacing is small.

Bibliography

Abbamonte, P., Rusydi, A., Smadici, S., Gu, G. D., Sawatzky, G. A., and Feng, D. L. (2005). *Nat. Phys.*, **1**, 155.

Alexandrov, A. S. (2008). *Journal of Physics: Condensed Matter*, **20**, 192202.

Andersen, O., Liechtenstein, A., Jepsen, O., and Paulsen, F. (1995). *Journal of Physics and Chemistry of Solids*, **56**, 1573.

Anderson, P. W. (1987). *Science*, **235**, 1196.

Anderson, P. W. (1998). cond-mat/9812063.

Audouard, A., Jaudet, C., Vignolles, D., Liang, R., Bonn, D. A., Hardy, W. N., Taillefer, L., and Proust, C. (2009). *Phys. Rev. Lett.*, **103**, 157003.

Bangura, A. F., Fletcher, J. D., Carrington, A., Levallois, J., Nardone, M., Vignolle, B., Heard, P. J., Doiron-Leyraud, N., LeBoeuf, D., Taillefer, L., Adachi, S., Proust, C., and Hussey, N. E. (2008). *Phys. Rev. Lett.*, **100**, 047004.

Bardeen, J., Cooper, L. N., and Schrieffer, J. R. (1957). *Phys. Rev.*, **108**, 1175–1204.

Baruch, S. and Orgad, D. (2008). *Phys. Rev. B*, **77**, 174502.

Bednorz, J. G. and Muller, K. A. (1986). *Zeitschrift fur Physik B Condensed Matter*, **64**, 189.

Berg, E., Fradkin, E., Kim, E. A., Kivelson, S. A., Oganesyan, V., Tranquada, J. M., and Zhang, S. C. (2003). *Rev. Mod. Phys.*, **75**, 1201.

Berg, E., Fradkin, E., Kim, E. A., Kivelson, S. A., Oganesyan, V., Tranquada, J. M., and Zhang, S. C. (2007). *Phys. Rev. Lett.*, **99**, 127003.

Berg, E., Fradkin, E., and Kivelson, S. A. (2009). *Phys. Rev. B*, **79**, 064515.

Borisenko, S. V., Kordyuk, A. A., Yaresko, A. N., Zabolotnyy, V. B., Inosov, D. S., Schuster, R., Buchner, B., Weber, R., Follath, R., Patthey, L., and Berger, H. (2008). *Phys. Rev. Lett.*, **100**, 196402.

Brown, S. and Gruner, G. (1994). *Scientific American*, **270**, 50.

Chakravarty, S., Laughlin, R. B., Morr, D. K., and Nayak, C. (2001). *Phys. Rev. B*, **63**, 094503.

Chen, K.-T. and Lee, P. A. (2009). *Phys. Rev. B*, **79**, 180510.

Corboz, P., White, S. R., Vidal, G., and Troyer, M. (2011). *Phys. Rev. B*, **84**, 041108.

de Gennes, P. G. (1989). *Superconductivity of metals and alloys.* Westview press.

Ding, H., Norman, M. R., Yokoya, T., Takeuchi, T., Randeria, M., Campuzano, J. C., Takahashi, T., Mochiku, T., and Kadowaki, K. (1997). *Phys. Rev. Lett.*, **78**, 2628.

Doiron-Leyraud, N., Proust, C., LeBoeuf, D., Bonnemaison, J. L. J.-B., Liang, R., Bonn, D. A., Hardy, W. N., and Taillefer, L. (2007). *Nature*, **447**, 565.

Elfimov, I. S., Sawatzky, G. A., and Damascelli, A. (2008). *Phys. Rev. B*, **77**, 060504.

Emery, V. J., Kivelson, S. A., and Zachar, O. (1997). *Phys. Rev. B*, **56**.

Franz, M. and Tešanović, Z. (2000). *Phys. Rev. Lett.*, **84**, 554.

Fujita, M., Goka, H., Yamada, K., Tranquada, J. M., and Regnault, L. P. (2004). *Phys. Rev. B*, **70**, 104517.

Garg, A. (2006). *Strongly Correlated Systems: Metal-Insulator Transitions and Superconductors.* Ph.D. thesis, Tata Institute of Fundamental Research, Mumbai, India.

Gor'kov, L. P. and Schrieffer, J. R. (1998). *Phys. Rev. Lett.*, **80**, 3360.

Goswami, P., Rani, M., and Kapoor, A. (2010). arXiv:1007:5041v1.

Hardy, W. N., Bonn, D. A., Morgan, D. C., Liang, R., and Zhang, K. (1993). *Phys. Rev. Lett.*, **70**, 3999–4002.

Harrison, N. (2009). *Phys. Rev. Lett*, **102**, 206405.

Harshman, D. R., Schneemeyer, L. F., Waszczak, J. V., Aeppli, G., Cava, R. J., Batlogg, B., Rupp, L. W., Ansaldo, E. J., and Williams, D. (1989). *Phys. Rev. B*, **39**, 851.

Haug, D., Hinkov, V., Suchaneck, A., Inosov, D. S., Christensen, N. B., Niedermayer, C., Bourges, P., Sidis, Y., Park, J. T., Ivanov, A., Lin, C. T., Mesot, J., and Keimer, B. (2009). *Phys. Rev. Lett.*, **103**, 017001.

Hofstadter, D. R. (1976). *Phys. Rev. B*, **14**, 2239.

Howald, C., Eisaki, H., Kaneko, N., and Kapitulnik, A. (2003). *Proceedings of the National Academy of Sciences*, **100**(17).

Hücker, M., v. Zimmermann, M., Gu, G. D., Xu, Z. J., Wen, J. S., Xu, G., Kang, H. J., Zheludev, A., and Tranquada, J. M. (2011). *Phys. Rev. B*, **83**, 104506.

Imai, T., Shimizu, T., Yasuoka, H., Ueda, Y., and Kosuge, K. (1988). *Journal of the Physical Society of Japan*, **57**, 2280–2283.

Jaudet, C., Vignolles, D., Audouard, A., Levallois, J., LeBoeuf, D., N. Doiron-Leyraud, B. Vignolle, M. N., Zitouni, A., Liang, R., Bonn, D. A., Hardy, W. N., Taillefer, L., and Proust, C. (2008). *Phys. Rev. Lett.*, **100**, 187005.

Laliberte *et al.*, F. (2011). *Nature Communications*, **2**, 432.

Leboeuf *et al.*, D. (2007). *Nature*, **450**, 533.

Li, Q., Hücker, M., Gu, G. D., Tsvelik, A. M., and Tranquada, J. M. (2007). *Phys. Rev. Lett.*, **99**, 067001.

Lifshitz, L. M. and Kosevich, A. M. (1955). *Zh. Eksp. Teor. Fiz.*, **29**, 730.

Loder, F., Kampf, A. P., and Kopp, T. (2010). *Phys. Rev. B*, **81**, 020511.

Marinelli, L., Halperin, B. I., and Simon, S. H. (2000). *Phys. Rev. B*, **62**, 3488.

Matsuda, M., Fujita, M., Yamada, K., Birgeneau, R. J., Endoh, Y., and Shirane, G. (2002). *Phys. Rev. B*, **65**, 134515.

Melikyan, A. and Vafek, O. (2008). *Phys. Rev. B*, **78**, 020502.

Melnikov, A. S. (1999). *J. Phys. Cond. Matt.*, **82**, 4703.

Millis, A. J. and Norman, M. R. (2007). *Phys. Rev. B*, **76**, 220503.

Norman, M. R. and Pepin, C. (2003). *Reports on Progress in Physics*, **66**, 1547.

Norman, M. R., Takeuchi, T., Takahashi, T., Mochiku, T., Kadowaki, K., Guptasarma, P., and Hinks, D. G. (1998). *Nature*, **392**, 157.

Ogata, M. and Fukuyama, H. (2008). *Reports on Progress in Physics*, **71**, 036501.

Onsager, L. (1952). *Phil. Mag.*, **43**, 1006.

Pereg-Barnea, T., Weber, H., Refael, G., and Franz, M. (2009). *Nature Physics*, **6**, 44.

Pippard, A. B. (1962). *Proc. Roy. Soc. A*, **270**, 1.

Raczkowski, M., Capello, M., Poilblanc, D., Frésard, R., and Oleś, A. M. (2007). *Phys. Rev. B*, **76**, 140505.

Randeria, M., Duan, J.-M., and Shieh, L.-Y. (1989). *Phys. Rev. Lett.*, **62**, 981–984.

Riggs, S. C., Vafek, O., Kemper, J. B., Betts, J. B., Migliori, A., Balakirev, F. F., Hardy, W. N., Liang, R., Bonn, D. A., and Boebinger, G. S. (2011). *Nature Physics*, **7**, 332.

Rourke, P. M. C., Bangura, A. F., Proust, C., Levallois, J., Doiron-Leyraud, N., LeBoeuf, D., Taillefer, L., Adachi, S., Sutherland, M. L., and Hussey, N. E. (2010). *Phys. Rev. B*, **82**, 020514.

Schafgans, A. A., LaForge, A. D., Dordevic, S. V., Qazilbash, M. M., Padilla, W. J., Burch, K. S., Li, Z. Q., Komiya, S., Ando, Y., and Basov, D. N. (2010). *Phys. Rev. Lett.*, **104**, 157002.

Sebastian, S. E., Harrison, N., Palm, E., Murphy, T. P., Mielke, C. H., Liang, R., Bonn, D. A., Hardy, W. N., and Lonzarich, G. G. (2008). *Nature*, **454**, 200.

Shoenberg, D. (1984). *Magnetic Oscillations in Metals*. Cambridge University Press.

Singleton, J., de la Cruz, C., McDonald, R. D., Li, S., Altarawneh, M., Goddard, P., Franke, I., Rickel, D., Mielke, C. H., Yao, X., and Dai, P. (2010). *Phys. Rev. Lett.*, **104**, 086403.

Takigawa, M., Ichioka, M., and Machida, K. (2002). *The European Physical Journal B - Condensed Matter and Complex Systems*, **27**, 303–311.

Tesanovic, Z. (2011). *Nature Physics*, **7**, 283.

Tinkham, M. (1996). *Introduction to Superconductivity.* Dover publications.

Tranquada, J. M., Sternlieb, B. J., Axe, J. D., Nakamura, Y., and Uchida, S. (1995). *Nature*, **375**, 561.

Tranquada, J. M., Gu, G. D., Hücker, M., Jie, Q., Kang, H.-J., Klingeler, R., Li, Q., Tristan, N., Wen, J. S., Xu, G. Y., Xu, Z. J., Zhou, J., and v. Zimmermann, M. (2008). *Phys. Rev. B*, **78**, 174529.

Tsuei, C. C. and Kirtley, J. R. (2000). Pairing symmetry in cuprate superconductors. *Rev. Mod. Phys.*, **72**, 969–1016.

Vafek, O., Melikyan, A., Franz, M., and Tešanović, Z. (2001). *Phys. Rev. B*, **63**, 134509.

Van Harlingen, D. J. (1995). *Rev. Mod. Phys.*, **67**, 515–535.

Vignolle, B., Carrington, A., Cooper, R. A., French, M. M. J., Mackenzie, A. P., Jaudet, C., Vignolles, D., Proust, C., and Hussey, N. E. (2008). *Nature*, **455**, 952.

Volovik, G. E. (1993). *JETP Lett.*, **58**, 469.

Williams, G. V. M., Tallon, J. L., Haines, E. M., Michalak, R., and Dupree, R. (1997). *Phys. Rev. Lett.*, **78**, 721–724.

Wu, T., Mayaffre, H., Kramer, S., Horvatic, M., Berthier, C., amd Ruixing Liang, W. N. H., Bonn, D. A., and Julien, M.-H. (2011). *Nature*, **477**, 191.

Xu, G., Tranquada, J. M., Perring, T. G., Gu, G. D., Fujita, M., and Yamada, K. (2007). *Phys. Rev. B*, **76**, 014508.

Yao, H., Lee, D.-H., and Kivelson, S. (2011). *Phys. Rev. B*, **84**, 012507.

Yelland, E. A., Singleton, J., Mielke, C. H., Harrison, N., Balakirev, F. F., Dabrowski, B., and Cooper, J. R. (2008). *Phys. Rev. Lett.*, **100**, 047003.

Yoshioka, D. (2002). *The quantum Hall effect.* Springer.

Zelli, M., Kallin, C., and Berlisnky, A. J. (2011). *Phys. Rev. B.*, **84**, 174525.

Zelli, M., Kallin, C., and Berlinsky, A. J. (2012). arXiv:1201.1920v2.